UNIVERSITÉ DE STRASBOURG

ÉCOLE DOCTORALE de PHYSIQUE ET CHIME PHYSIQUE (ED 182)
ICS UPR-22 CNRS

THÈSE présentée par :

Jean WOLFF

soutenue le : **14 juin 2013**

pour obtenir le grade de : **Docteur de l'université de Strasbourg**
Discipline/ Spécialité **: Physique**

Un modèle théorique des mélanges ternaires de lipides et de cholestérol

THÈSE dirigée par :	
M. Marques Carlos	Directeur de recherches, Université de Strasbourg
M.Thalmann Fabrice	Maitre de conférences, Université de Strasbourg
RAPPORTEURS :	
Mme. Viallat Annie	Directeur de recherches, Université de Marseille
M. Fournier Jean-Baptiste	Professeur, Université de Paris
AUTRES MEMBRES DU JURY :	
M. Johner Albert	Directeur de recherches, Université de Strasbourg
M. Andelman David	Professeur, Tel-Aviv University

UNIVERSITÉ DE STRASBOURG

Discipline: Physique

Un modèle théorique des mélanges ternaires de lipides et de choléstérol

Thèse de Doctorat présentée par

Jean Wolff

Le 14 juin 2013

Membres du Jury:

Président: M. Albert Johner
Rapporteur: M. Jean-Baptiste Fournier
Rapporteur: Mme. Annie Viallat
Membre invité: M. David Andelman
Directeur de thèse: M. Carlos Marques
Directeur de thèse: M. Fabrice Thalmann

Subject: Physics

Ternary mixtures of lipids and cholesterol: a theoretical model

Dissertation by

Jean Wolff

June 14, 2013

PhD committee:

President: M. Albert Johner
Rapporteur: M. Jean-Baptiste Fournier
Rapporteur: Mme. Annie Viallat
Invited Member: M. David Andelman
Supervisor: M. Carlos Marques
Supervisor: M. Fabrice Thalmann

Remerciements

A la fin de cette aventure, je me rappelle les moments de grande solitude perdu dans les paysages des transitions de phase et les moments de joie pour un calcul qui aboutit ou un concept qui devient plus clair. Mais ce qui me revient surtout ceux sont les rencontres que j'ai faites et les discussions que j'ai pu avoir et qui m'ont fait progresser.

Je tiens tout d'abord à remercier Jean-Pierre Munch, alors directeur de l'UFR de physique pour ces conseils et son écoute, ainsi que pour sa précieuse aide afin de me permettre de démarrer mon stage de M2, puis ma thèse en me faisant rencontrer Carlos Marques et Fabrice Thalmann. J'ai commencé ma thèse en septembre 2009 à l'Institut Charles Sadron alors dirigé par M.Legrand et je le remercie pour m'avoir accueilli avec chaleur et enthousiasme, ainsi que M.guenet, actuel directeur de l'ICS.

Je remercie Carlos et Fabrice pour le temps qu'ils m'ont accordé et l'infinie patience qu'ils ont eu à mon égard pendant ces trois années et demie de thèse. Ils m'ont guidé avec beaucoup de gentillesse et d'encouragements en prenant mon projet au sérieux. Ils m'ont appris que *le diable se cache dans les details et qu'il est vaillant.* Je garderai en souvenir les premières discussions que nous avons eu à trois pendant lesquelles il me semblait que je n'avais jamais fait de physique dans ma vie tellement je n'y comprenais pas grand chose; merci à vous deux pour les progrès que j'ai pu faire.

Je remercie Jean-Baptiste Fournier et Annie Viallat, les deux rapporteurs du jury d'avoir bien voulu juger mon travail. Merci à Albert Johner d'avoir accepté de faire parti de mon jury. Un grand merci à David Andelman d'avoir fait ce long voyage pour faire partie de mon jury de thèse.

Je tiens à remercier tous les membres de MCUBE et en particulier Thierry Charitat pour sa disponibilité (Phys.Stat., latex...) et sa bonne humeur, André Schröder pour ses conseils en programmation (numerical recipes, ...) et sa patience, Pierre Muller et Tatiana Schmatko pour leur gentillesse. Merci à Jean Farago pour ses

conseils de lecture et ses intéressantes remarques.

Je tiens à remercier tous mes camarades de bureau avec lesquels j'ai beaucoup discuté ou bu de thé, pour leur gentillesse à l'egard d'un vieil étudiant comme moi. Merci à Balbine Amoussou pour ses encouragements, à Yuting Sun pour ses logiciels, à Wellington Gomez-Dantas pour ses conseils, à Andréas Weinberger, Pierre Ayoub et Laurence Jennings pour m'avoir fait progresser en anglais à l'oral et pour les encouragements de fin de thèse, ainsi qu'à Nava Schulmann pour son écoute. Un grand merci à Georges Weber avec qui j'ai debuté ma thèse et qui m'a supporté lors de nos nombreux voyages autour du globe, de l'est de l'Europe à l'ouest de l'Orient.

Un merci tout special à Paule Vannson pour sa disponibilité dans la préparation des voyages, à Marc Basler pour ses interventions lors des bugs informatiques, à Olivier Benzerara pour ses conseils en informatique et à Jean-Marc Chauvelot pour le courrier qui arrive à temps.

Je tiens à remercier tous mes collègues de l'ORT qui n'ont jamais hesité à me remplacer pendant mes déplacements. Un merci spécial à Serge Royer, Alain Lypsic, Eva Riveline, Jean-Michel Toledano et Gaetanne Armbrust pour leur soutien. Un grand merci à Gaetanne pour ses cours d'anglais qui m'ont fait progresser autant à l'oral qu'à l'écrit.

Merci à Gerard Mamou pour son expertise en informatique qu'il est toujours prêt à partager et à Philippe Auscher pour ses conseils avisés.

Je tiens à remercier la direction de l'ORT pour son soutien dans mon projet et en particulier M.Sabbah pour m'avoir faciliter la tâche et m'avoir soutenu tout au long de ces trois années. Je suis conscient que sans ce soutien exceptionnel le projet n'aurait pas pu aboutir.

Enfin un grand merci à toute ma famille pour son soutien.

Contents

Preface

I prepared my PhD at the Charles Sadron Institute, Strasbourg, from September 2009 to June 2013 under the supervision of Carlos Marques and Fabrice Thalmann, on phase transitions in ternary mixtures of lipids and cholesterol.

Lipid membranes have captivated physicists, chemists and biologists alike owing to their central role in living cells, their biochemical diversity and the fascinating polymorphism of their structural organization. Lipid mixtures are remarkable for their complex phase behavior, in which cholesterol molecules play a very special role. Gel and fluid states are the most striking manifestation of the thermotropic behavior of phospholipds, separated by a melting transition. This main transition corresponds to a sharp change in the statistical conformations of the hydrophobic chains, coupled with a lateral extension and a reduction of the thickness of the membrane. It is a weakly first order transition for membranes of pure composition.

In the recent years, ternary lipid systems comprising phospholipids and cholesterol were established as important model systems in relation with lateral lipid segregation phenomena in membranes. Ternary systems comprising a phospholipid in the liquid state, a second phospholipid in the gel state and cholesterol display several unique characteristics, including a surprising fluid-fluid coexistence, beside the more usual fluid-gel coexistence.

Membranes are dynamic and fluctuating. They constantly rearrange, reorganize and react to external perturbations. There is currently no technique capable of imaging membranes at the resolution (100 nm or less) and speed (1μs or less) where phenomena such as membrane severing and fusion, domain formation, protein diffusion and interactions happen. Experiments provide ensemble averaged or time averaged information, and theoretical models are the necessary link between the microscopic reality and the experimental measurements.

The aim of this work is to build a simple and predictive theoretical model for determining the phase stability of ternary lipid-cholesterol mixtures, and to examine the implications of this model regarding interactions between heterogeneous components in such model membranes.

The first chapter is an introduction to the biophysics of phospholipid membranes. I first present the nature of lipids and cholesterol, the structure and the mechanical properties of self-assembled bilayers, their thermal phase transitions and the various phase coexistences in multicomponent systems (Gibbs diagrams). In a second part, I mention different experimental methods which have revealed this phase behavior, and determine the thermodynamic stability of each phase. This includes X-ray scattering, NMR and fluorescence spectroscopy, microscopy and calorimetry. Finally I give an account of the state of the art with theoretical models of binary and ternary lipid mixtures, from the early 1970s to now. In a last part, I briefly remind the wetting theory about binary system and the Cahn's approach using graphical arguments.

In the second chapter, I introduce a thermodynamic model which allows determining the phase stability of the ternary DOPC/DPPC/Cholesterol mixture. I discuss the structure of the model and describe an original method based on a discrete geometry algorithm for computing numerically the convex hull of the Gibbs free-energy surface in three dimensions.

The third chapter explains how I refined the diagrams by solving numerically the Gibbs equations for binary and ternary coexistence, and for the critical point. The difficulty comes from the explicit presence of the scalar order parameter associated with the fluid-gel state of the membrane. This analytical determination allows us to find the tie-lines, the critical plait point position and the boundaries of the binary and ternary domains. I determined the Gibbs diagrams of several other ternary mixtures such as DOPC/PSM/Chol., POPC/PSM/Chol., and DiphytanoylPC/DPPC/Chol. and their temperature dependence. I finally attempt to improve the binary coexistence diagrams by taking into account the variation of area per molecule during the melting transition.

In the last chapter, I introduce a Landau-Ginzburg extension of this thermodynamic model. I compute the line tension between a liquid ordered and liquid disordered domain. Then, I consider the wetting of large and intermediate size circular inclusions, when the binary mixture is slightly off-coexistence. I determine the "pre-wetting" horn of the system, discuss the effect of the curvature on wetting, and the thermodynamic stability of the profiles which are obtained.

Chapter 1

Introduction

1.1 Biomembranes

1.1.1 Presentation

The cells are the structural units of all unicellular or multicellular organisms. Bacteria are prokariotic cells, while plants, animals and fungi are composed of eukariotic cells (1.1).

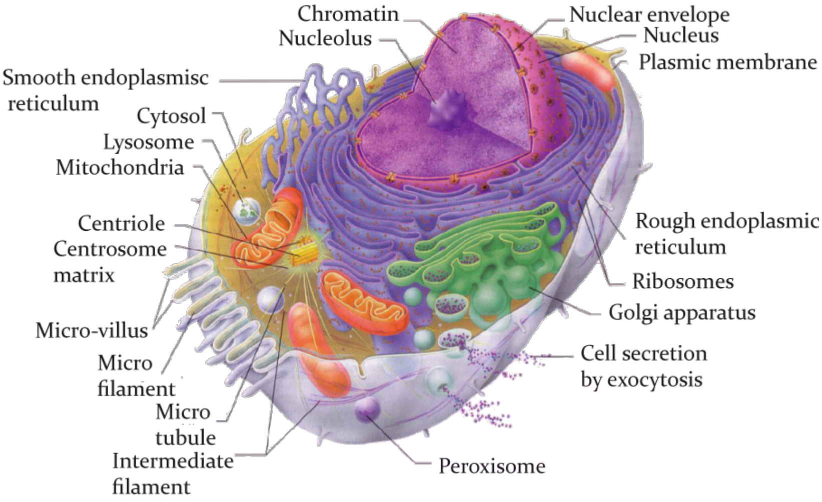

Figure 1.1 – *Internal view of the cell (adapted from [1]).*

A prokariotic cell is not compartmentalized and possesses a strong plasmic membrane, simple or double, depending on the so-called positive Gram or negative Gram character. The plasmic membrane isolates the interior of the cell from the exterior, regulates the inner medium, and provides metabolic energy. An eukariotic cell has a plasmic membrane, and in addition many internal membranes or biomembranes delimiting organelles inside the cell, such as the endoplasmic reticulum, the mitochondria, the Golgi apparatus, or the peroxisomes, all in charge of performing various vital functions (figure 1.1). Eukariotic cells are significantly larger than prokaryotic cells and their architecture is much more sophisticated. They compose the tissues of higher organisms where they perform a large number of different functions, both individually and collectively.

The internal compartments allow cells to perform simultaneously several antagonist bio-chemical reactions, such as proteins synthesis and degradation, and setting up electrochemical gradients. Biomembranes regulate the intake of essential molecules for its structure, operation and the excretion of toxics resulting from its metabolism. They assure protection against the environment. The biomembrane is semipermeable or provided with a selective permeability so that water molecules go through easily, while ions or larger molecules are stuck on each side. Many substances (peptides, proteins, ions, nucleic acids...) are not able to proceed passively through the membrane but rely on using trans-membrane carriers (ionic channels, permeases, and active transport proteins). Finally membranes can internalize macromolecules by endocytosis, and excrete substances by exocytosis mechanism. The endocytosis consists in plasmic membrane invaginations localized on specific domains called coated pits, in which membrane receptors activate the endocytic processes. The exocytosis phenomenon corresponds to fusion between intracellular vesicles and plasmic membrane in order to release their content outside the cell. The collective behavior of cells in organ and tissues requires a constant communication between cells and a synchronization of their functions, for which the external membrane is the central gateway. The studies of the cell properties and functions is the focus of cellular biology.

Biomembranes are composed of a wide variety of chemical compounds, namely lipids, proteins and oses. To simplify to the extreme, lipids play a structural role while proteins play many different functional roles (for many of them still unknown), such as signalling channels, anchoring to the internal cell cytoskeletton or the extracellular matrix, and performing enzymatic reactions. Lipids represent a very diverse class of chemical compounds, characterized by their poor solubility in water. Some lipids, commonly referred as “fat” or “grease” are almost insoluble. These are believed to represent a form of metabolic energy storage. Other lipids are only partially soluble, a property known as amphiphilic character (see section 1.1.3 below). Amphiphilic compounds are the one that chiefly contributes the biomembranes structure.

Lipid membrane composition varies enormously from one cell to the other, and within a cell. This lipid diversity constitutes a puzzle, biologists and biochemists are far from understanding the reasons for these compositional variations, nor do they apprehend the subtle regulations operating among them. Unlike proteins and nucleic acids, which seem to work in a highly specific and specialized manner, the lipid functions are somewhat “fuzzy”. Understanding the lipid functions requires some knowledge and techniques pertaining to the field of physics and physical chemistry: rheology, mechanics, phase transitions, critical phenomena to name a few. This is why the study of membranes and membrane properties has become a popular topic in modern biophysics.

1.1.2 The concept of bilayer

In 1925, Gorter et Grendel [2] demonstrated that the monolayer area of lipids extracted from red blood cells is twice as large as the contour area of these cells. They were the first to suggest that lipid compounds (originally referred as “lipoids”) self-assemble into a bilayer structure.

Much later, in 1972, Singer and Nicolson [3] came up with a new model of cell membrane known as the fluid mosaic model (1.2). They suggested that membrane proteins are actually dispersed in a fluid “sea” of lipids, free to move around with either one or two sides exposed the free water solution surrounding the membrane. The mosaic term then refers to the inhomogeneous and spontaneously fluctuating arrangement of the membrane components.

Lipids are subject to intramolecular rotations and isomerizations, as well as intermolecular lateral diffusion. The bilayer is divided in two opposing leaflets. A lipid move consisting in leaving one leaflet for the other is known as flip-flop exchange. The solubility of most lipids is so small that they remain trapped within membranes for very long times. Beside these individual motions, membranes are subject to collective out-of-plane undulations. Altogether, the fluid membrane state looks very disordered and fluctuating.

1.1.3 Size and structure of lipids

Two major families of membrane forming lipids are the *glycerophospholipids* and the *sphingolipids*. They are amphiphilic compounds, with an hydrophilic, bulky

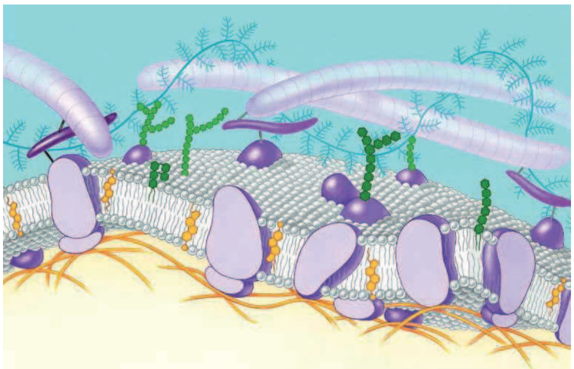

Figure 1.2 – *Artist view of a cell membrane.*

moiety commonly designated as the head or *headgroup* and two distinct hydrophobic, aliphatic oligomers known as *tails* (1.3.a)

The length of these molecules lies between 2 and 3 nm, the molecular cross-section area ranges from 0.60 to 0.75 nm^2 [4]. A single lipid has a typical volume of 1 nm^3, for a molecular mass of about 800 g/mol.

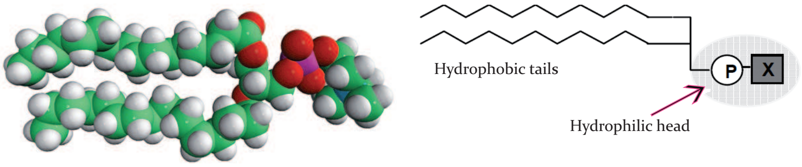

(a) Representation of a lipid (b) Skeletton of a lipid

Figure 1.3 – *Glycerophospholipid molecule.*

Glycerophospholipids are composed of a glycerol backbone linked to phosphate group (abbrev. P) and a polar or charged headgroup on the 3rd carbon (1.3.b). Common headgroup names (ethanolamine, choline, glycerol...) are shortened to their first letter (E,C,G...)(1.4). Two saturated or unsaturated fatty acids are linked by an ester bond, respectively to the 1st (*sn1*) and 2nd (*sn2*) carbon of the glycerol backbone. Common fatty acids possess an even number of carbons starting from 12 to more than 20, with possibly *cis* insaturations. Common fatty acid names are abbreviated as depicted in Table 1.1. Following this rule, the acronym DOPC naturally stands for *1,2-dioleoyl-sn-glycero-3-phosphocholine*, while *1-palmitoyl-2-oleoyl-sn-glycero-3-phosphoethanolamine* is referred as POPE.

Sphingolipids are today recognized as essential components of the plasmic membrane. Their architecture is somewhat similar to glycerophospholipid, except but a single labile fatty acid (amide bond) attached to a long chain called sphingosine.

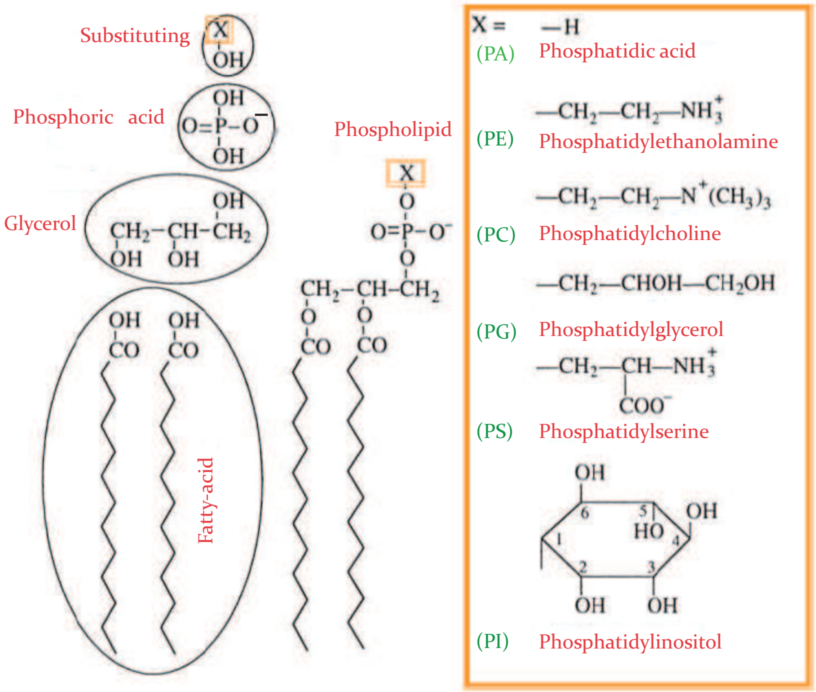

Figure 1.4 – *Molecule of glycerophospholipid with different headgroups (adapted from [1]).*

Usual name	Formula	Symbol
Saturated fatty-acid		
(L) Lauric	$CH_3 - (CH_2)_{10} - COOH$	12:0
(M) Myristic	$CH_3 - (CH_2)_{12} - COOH$	14:0
(P) Palmitic	$CH_3 - (CH_2)_{14} - COOH$	16:0
(S) Stearic	$CH_3 - (CH_2)_{16} - COOH$	18:0

Usual name	Formula	Symbol
Insaturated fatty-acid		
(O) Oleic	$CH_3 - (CH_2)_7 - CH = CH$ $-(CH_2)_7 - COOH$	18: 1(9)
(Li) Linoleic	$CH_3 - (CH_2)_4 - CH = CH$ $-CH_2 - CH = CH - (CH_2)_7 - COOH$	18: 2(9,12)
(Lic) Linolenic	$CH_3 - CH_2 - CH = CH$ $-CH_2 - CH = CH - CH_2 - CH = CH - (CH_2)_7 - COOH$	18: 3(9,12,15)
(A) Arachidonic	$CH_3 - (CH_2)_4 - [CH = CH - CH_2]_3$ $-CH = CH - (CH_2)_3 - COOH$	20: 4(5,8,11,14)

Table 1.1 – *Examples of saturated and insaturated fatty acids (adapted from [5]).*

They are commonly abbreviated as SM (1.5).

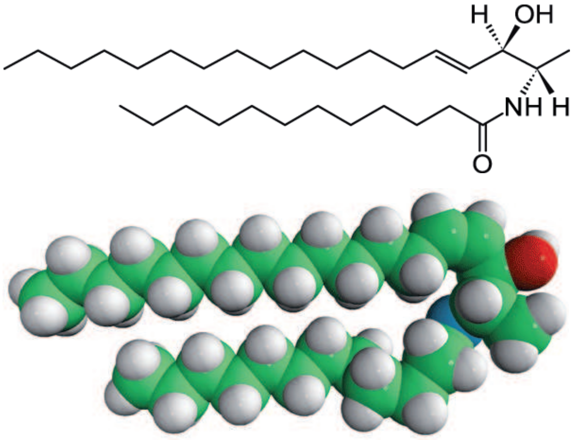

Figure 1.5 – *A sphingosine.(N-lauroyl-1-deoxysphingosine (m18:1/12:0)).*

The insaturated fatty acids present a *cis- trans* isomerism, the *cis* isomer showing a kinked orientation of its tail of about 120°. This kink causes an increase of the mean volume occupied by the molecule, and destroys the regular packing of the tails, as it occurs for instance in the low temperature crystalline phases of paraffins. These effects are all the more pronounced that the insaturation is located near the middle of the chain. As we will see in the next sections, the existence of these kinks has important consequences as far as membrane thermodynamics is concerned.

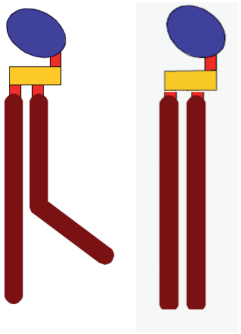

Figure 1.6 – *Lipid species. with a cis insaturated fatty-acid kinked tail (left) and lipid with two saturated tails (right).*

1.1.4 Cholesterol

Cholesterol is considered as a lipid, due to its amphiphile character and its significant presence in some membranes. However, the cholesterol structure differs greatly from the two previous lipid families. Cholesterol possesses a non-aromatic polycyclic structure terminated by a short hydrophobic tail at one side and an hydrophilic alcool residu at the opposite side (1.7). It is a member of an important class of molecules known as steroids.

Cholesterol is found in various proportions in eukaryotic cells, and reaches significant fractions in the outer plasma membrane. Its biological role is manifold and still matter of debate and question. For instance, the stiffness, the elasticity, the thickness and the permeability of membranes are all affected by the amount of cholesterol. The molecule has a condensing effect, which means that the area of a cholesterol-saturated lipid mixture is less than the specific area of its components, consistent with a strong mutual affinity between the two components. The cholesterol molecule is flat on one side, and rough on the opposite side, medling with the usual arrangement of phospholipid tails, bringing order to the disordered lipid phases and disorder to the ordered lipid phases [6]. Cholesterol is specific to higher eukaryotic organisms, where its presence is necessary for membrane fluidization, but analogue molecules are found in vegetals, yeasts or fungi. Cholesterol is not found in prokaryotes (bacteria).

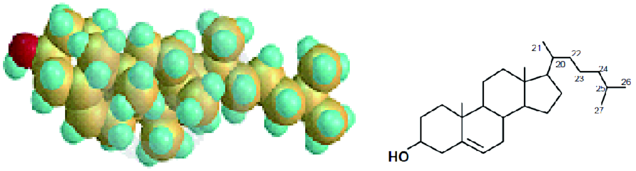

Figure 1.7 – *Cholesterol molecule and formula.*

1.1.5 Self-assembly and lyotropic meso-phases

The poor solubility of glycerophospholipids is documented in ref. [7]. As a result of their amphiphilic character and their molecular shapes, these lipid molecules self-assemble in water to form extended structures, called mesophases. Lamellar phases are common, but other structures are also seen, depending on pH, temperature and composition (figure 1.8). Lamellar phases are favored, as this is optimal in terms of molecular packing, shielding the hydrophobic part from, and exposing the polar head to the water solution.

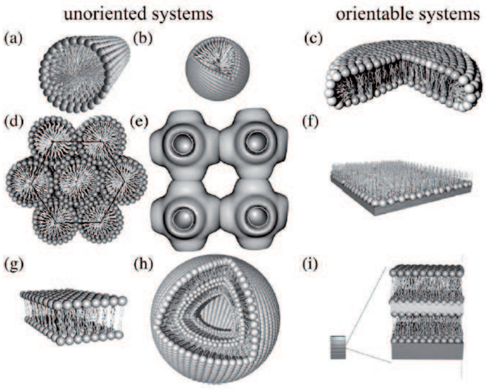

Figure 1.8 – *Example of surfactant morphologies. (a) Micellar tubes, (b) spherical micelles, (c) disc-shaped bicelles, (d) hexagonal phase, (e) cubic phase, (f) langmuir monolayer at the air–water interface, (g) lamellar phase, (h) multilamellar liposomes, and (i) stacked bilayers on a solid support[8].*

The sophisticated balance between hydrophilic and hydrophobic, electrostatic and dispersive forces leads to a number of possible structures, function of the amount of water in the mixture, referred as the lyotropic behavior of the amphiphile.

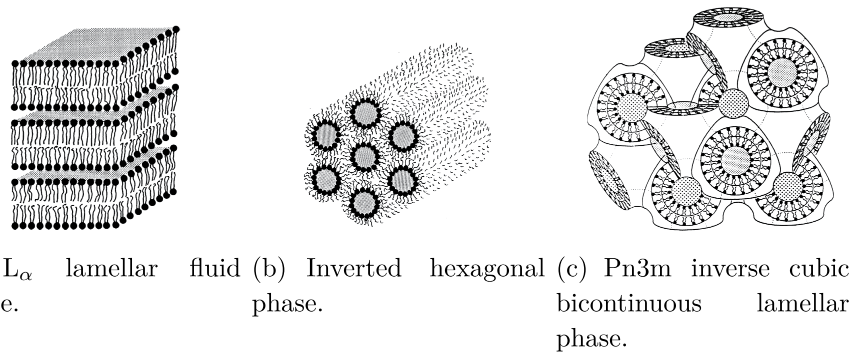

(a) L_α lamellar fluid phase.

(b) Inverted hexagonal phase.

(c) Pn3m inverse cubic bicontinuous lamellar phase.

Figure 1.9 – *Several lipid mesophases[9].*

We can observe on figure (1.8) closed and opened meso-phases composed of surfactant monolayers (a,b,c,d,e,f) and surfactant bilayers (g,h,i). The name meso-phase is given because the scale of the regular spatial variations is mesoscopic, larger than the microscopic size of the lipids. Lipids in water give also various meso-phases, though with a lesser diversity, shown on figure (1.9).

We show on figure (1.10) the ideal diagram of a lyotropic species, with different domains of stability for each meso-phase, as water dilution increases. Real amphiphilic compounds display many of the phases featured in this diagram.

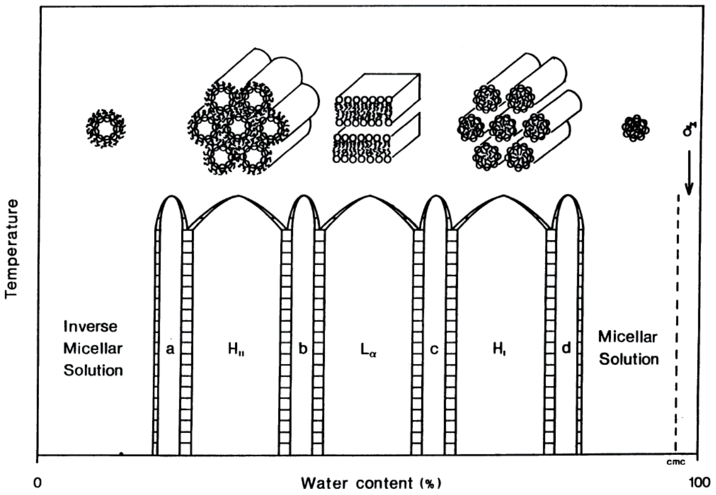

Figure 1.10 — *Schematic phase diagram of a lyotropic species. The a,b,c,d phases are cubic phases. [9].*

1.1.6 Vesicles

At low concentration, lipid water dispersions lead to closed compact structures known as vesicles (1.11). Single, isolated bilayers with free edges are not stable and close spontaneously to form spherical vesicles. These structures are filled with, and surrounded by water.

Vesicle diameters range from 50 nm for the small ones, up to 50 μm for the large ones, while their thickness corresponds roughly to the double of a lipid length, say 5 nm. Small vesicles are known as SUV (small unilamellar vesicles) or liposomes with a diameter less than a micrometer. Large vesicles are referred as LUV or GUV (large or giant unilamellar vesicles). The vesicle size is not under thermodynamic control, and depends mainly on the lipid suspension preparation procedure. In term of mesophases, lipid vesicles can be assimilated to highly hydrated lamellar phases.

The range of applications of lipid vesicles is immense, whether one is interested in fundamental issues or biotechnological applications. Lipid vesicles form an important class of model membrane systems, for carrying out structural, mechanical and biochemical studies [10]. On the other hand, encapsulation of chemicals and drugs into vesicles offer important prospects in biotechnology.

GUV are particularly suitable for optical and fluorescence microscopy studies, and can be individually manipulated by means of micropipette aspiration techniques. Two techniques are widely used to produce GUV: the gentle hydration technique and electroswelling technique (growth assisted by electric fields). Depending on the procedure, the yield, the sizes and the shapes of the resulting vesicles may differ. Moreover, significant fluctuations of composition from one vesicle to another have been reported, due to the complex formation process.

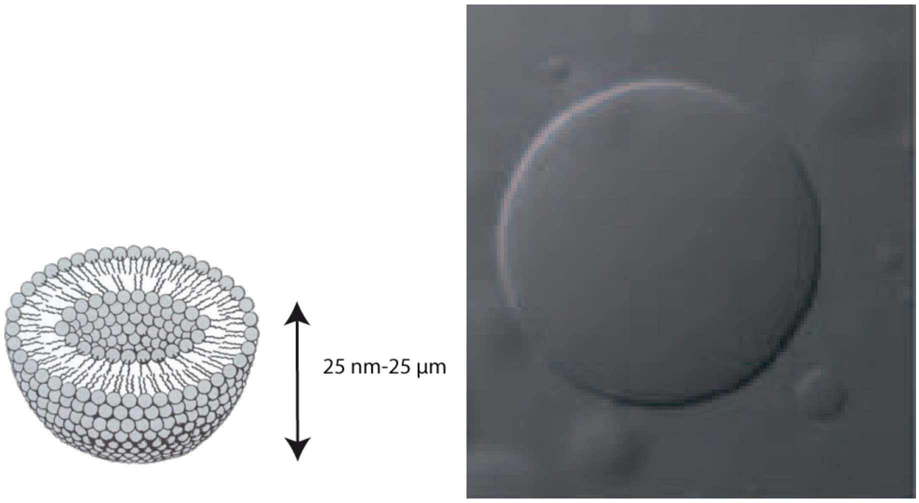

(a) Schematic vesicle.

(b) Microscopy observation by differential interference contrast of a lipid vesicle. [10]

Figure 1.11 – *Lipids vesicles.*

1.2 Lipid bilayer: a biomembrane model

1.2.1 Bilayer lipids phases

Lipid bilayers display a number of different thermodynamic phases and phase coexistences. The complexity of the phase diagram increases with the number of different components: single component bilayers, binary or ternary mixtures all display rich phase diagrams as a function of composition and temperature.

For instance, the lipid composition of the red blood cell membrane, once all non lipid factors have been removed, features about 250 different lipid species [11]. Membrane with artificial composition are *de facto* over-simplified. An alternative to circumvent this limitation consists in making vesicles with biological membranes extracts.

The lipid organization at molecular scale depends on multiple factors, size and charge of the headgroup, length and packing properties of the chains, mutual chemical affinities, etc...As a rule, chain length mismatches and poor packing of unlike chains tend to segregate different lipids, while entropic contributions favor homogeneous mixing.

Temperature, which enters in the entropy contribution $-TS$ of the free-energy, plays a prominent role as far as lipid chain ordering is concerned. Usual phospholipids present a marked thermotropic behavior, *i.e.* the existence of various phases depending mainly on the applied temperature.

At low temperatures, the membrane is in a crystal phase L_c, where the tails are extremely ordered, nested together, and the headgroups arrange along an hexagonal lattice. When the temperature increases, the membrane adopts gradually a less ordered organization called gel phase L_β, in which headgroups and lipid molecules enjoy some rotational freedom while chain tails stay ordered. At high temperatures, one observes a fluid phase L_α, in which headgroup positions and tail conformations are both disordered, with thousands of different possible conformational isomers [12]. We can see on figure (1.12) a representation of the different phases in membranes composed of pure POPC at different temperatures.

The presence of cholesterol in large amount in some membranes motivated studies on the cholesterol-membrane structure relationship, and also on the phase behavior of phospholipid-cholesterol mixtures. First came experimental evidences of a fluid-fluid coexistence in binary mixtures. This coexistence is still debated today as different experimental techniques deliver seemingly conflicting conclusions

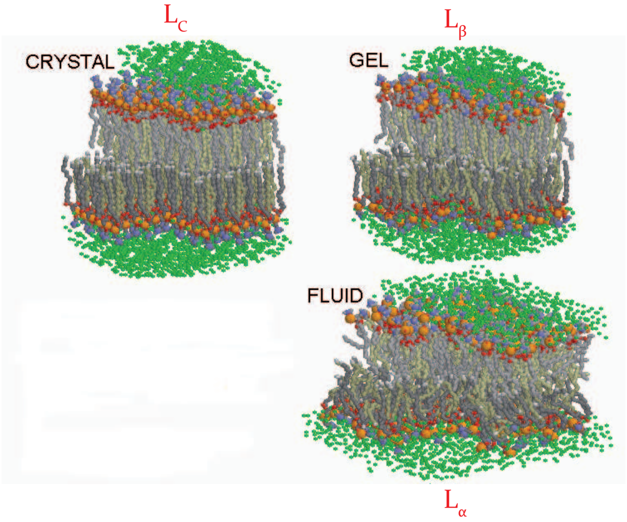

Figure 1.12 – *The three phases for a pure lipid POPC mixture, as predicted by molecular dynamics simulations. Orange: phosphorus, red: oxygen, blue: nitrogen, gray: palmitic chains, green: oxygen water, beige: oleic chains [13].*

(see experimental section below). The fluid-fluid coexistence in ternary mixtures is, however, widely accepted.

In this fluid-fluid coexistence, one of the phase is depleted in cholesterol and sound similar to the L_α fluid phase. This phase is referred as the *disordered phase* L_d in the context of phospholipid cholesterol systems. The other phase is enriched in cholesterol, and phospholipid tails look much more ordered, thereby leading to a *liquid ordered* phase L_o. The liquid ordered phase, however, is less ordered and less densely packed as the gel phase L_β. Cholesterol molecules confer to the phospholipid bilayer containing them both order and fluidity.

We can notice on the figure (1.13) that the insertion of cholesterol orders lipids in membrane by decreasing the width of the middle zone where the lipids from the upper and lower layers join, and induce a membrane thickening [14]. Moreover, cholesterol plays a role in the rigidity of membrane in increasing its flexibility [15].

1.2.2 Mechanical properties of the membrane

A widely accepted argument states that the self-assembled lipid structure depends primarily on the molecular shape, as illustrated on figure (1.14). The molecular shape enters as a dimensionless ratio between the occupied molecular volume and the product of the headgroup area with the chain length. One distinguishes three

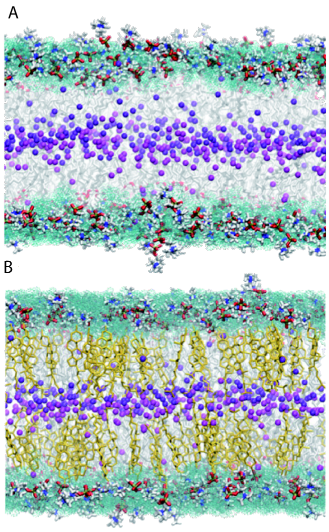

Figure 1.13 – ***A***) *L_d Disordered-liquid (DOPC),* ***B***) *L_o Ordered-liquid (DOPC/Cholesterol). Cholesterol molecules, colored goldenrod, are shown in stick representation, the terminal methyl groups are represented as spheres and colored purple and magenta to distinguish the methyls of each leaflet. Acyl chains shown in stick representation are gray. Phosphatidylcholine headgroups are also shown in stick representation and colored according to the element (red: oxygen; blue: nitrogen; gold: phosphorus; white: hydrogen). Water is represented by the aquamarine bands. [14].*

general lipid shapes: an inverted conical shape (A) which gives micelles or cylindrical micelles, a cylindrical shape (B) which forms preferentially bilayers, and finally a conical shape , which gives the hexagonal cylindrical inverted micelles H_2.

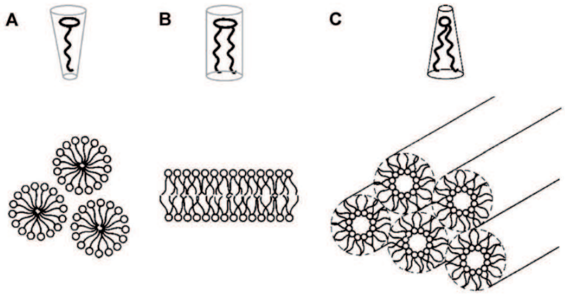

Figure 1.14 – *Illustration of the shape-structure concept of lipid polymorphism, indicating the overall shape of the molecules and examples of the aggregated structures[16].*

The optimal packing of lipids with non spherical shapes corresponds ideally to a curved monolayer, such as in hexagonal or micellar assemblies. The lipid assembly is therefore associated with a non vanishing spontaneous curvature C_0. In the case of a symmetric bilayer, with two leaflets of identical composition, the overall spontaneous curvature of the membrane vanishes, and the membrane stays flat. If the two leaflets have an asymmetric composition, the bilayer may show a non vanishing spontaneous curvature (figure 1.15). A spontaneous curvature may also be induced by an asymmetric composition (ionic content, pH...) of the solutions across the bilayer.

Even in a symmetric bilayer, each leaflet (or monolayer), can be associated to a spontaneous curvature C_0, consequence of the individual lipid shapes, corresponding to the curvature that the monolayer would adopt if it was possible to isolate it from its environment. The monolayer spontaneous curvature C_0 is an important intrinsic property of the membranes, linked to the functional properties of associated proteins [6].

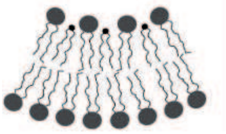

Figure 1.15 – *Bilayer made of two different monolayers.*

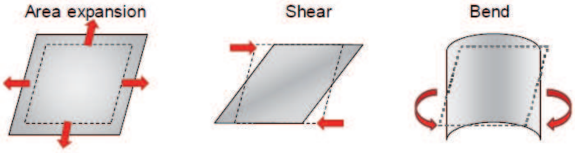

Figure 1.16 – *Three modes of membrane deformations [17].*

Out of the three main deformation modes represented on figure (1.16), two are elastic: the bending and the stretching deformation. Shear deformation offers no static resistance in fluid membranes, although the existence of a cytoskeletton in biological membranes renders the situation more complex. Each elastic mode is characterized by an elastic coefficient. The stretching coefficient K_A is defined as the ratio $K_A = A\mathrm{d}\sigma/\mathrm{d}A$ of the variation of surface tension σ accompanying a change in membrane area (strain $\mathrm{d}A/A$). The mechanical determination of K_A for pure DOPC is estimated to $K_A \approx 270 mN.m^{-1}$ for a range of tensions between 10^{-6} N and 10^{-4} N [15].

The bending moduli appear in the total bending energy E_S of the system, which is given by the Helfrich expression:

$$E_S = \int \left[\frac{\kappa}{2} \left(\frac{1}{R_1} + \frac{1}{R_2} - \frac{2}{R_0} \right)^2 + \frac{\kappa_G}{R_1 R_2} \right] \mathrm{d}A \tag{1.1}$$

Here R_1 and R_2 are the two principal radii of curvature describing the local curvature, R_0 the spontaneous radius of curvature of the membrane (figure 1.17), κ is the normal bending modulus and κ_G the Gaussian bending modulus. Expression (1.1) describes a situation of bending at constant area. This limit is indeed justified in many experimentally relevant situations, as stretching a membrane is energetically much less favorable than bending it.

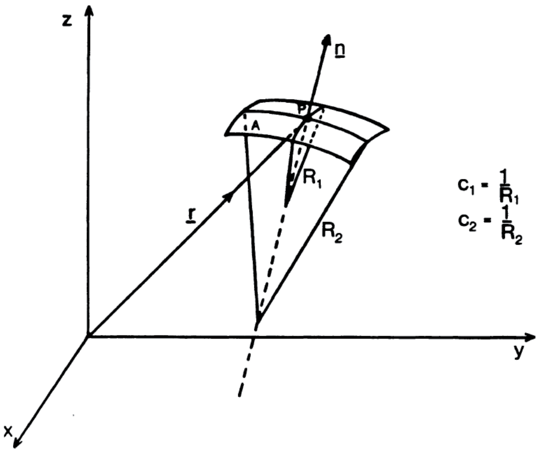

Figure 1.17 – *Main curvature radius[9].*

In the case of a closed object the Gauss-Bonnet theorem allows us to rewrite E_S as below:

$$E_S = \int \left[\frac{\kappa}{2} \left(\frac{1}{R_1} + \frac{1}{R_2} - \frac{2}{R_0} \right)^2 \right] \mathrm{d}A + \kappa_G 4\pi (1-g) \tag{1.2}$$

with g, the genus number which describes the topology of the object ($g = 0$ for a sphere and higher values for more complex objects with "holes"). In many practical cases, the Gaussian modulus plays no role.

The bending modulus changes by a large amount at the lipid main transition. Unsurprisingly, the rigidity of the fluid phase is much less than the one of the gel phase, leading to values of the bending modulus respectively equal to $\kappa \simeq 10kT$ (fluid phase) and $\kappa \simeq 200kT$ (gel phase).

There is a work by S.Leibler and D.Andelman [18] which relates curvature and composition, with the prediction that regions of strong curvature accommodate better the lipid fluid phase because the cost in energy to curve the membrane is higher when the lipids are ordered.

We show in figure (1.18) the lateral pressure profile $\pi(z)$ of the membrane as a function of the depth z in the membrane. The interfacial tension located at the polar-apolar interface induces a negative pressure compensated by a positive lateral pressure in the headgroups and acyl chains region due to steric repulsive forces. We can estimate the lateral pressure in the interior of the lipid bilayer by considering that the interfacial tension at the hydrophobic-hydrophilic interface is about 50 mN/m [19]. The lateral pressure in the interior of the membrane has to balance this interfacial tension, leading to $p_{\text{int.}} = 2\gamma/d \simeq 350$ atm, $d \simeq 3nm$ being the membrane thickness. The lateral pressure profile is related to the lipid shapes and to the spontaneous monolayer curvature C_0. Membrane proteins embedded in membranes have therefore to deal with significant lateral stresses.

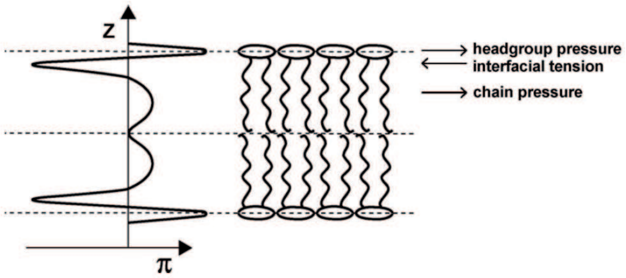

Figure 1.18 – *Schematic representation of the lateral pressure profile in the lipid bilayer. [16].*

1.2.3 Lateral membrane organization: Hydrophobic matching and rafts

Hydrophobic matching

Transmembrane proteins display a significant hydrophobic lateral surface, which must be coated with lipids in order to minimize their exposure to water molecules. When the length of the hydrophobic domain differs from the length of the hydrophobic region of the bilayer, the latter tries to adjust its thickness to the protein domain. The concept of hydrophobic matching is believed to play a leading role in the organization of biological membranes. We notice on the figure (1.19.a) that the lipids try to match the transmembrane protein thickness, similar to the meniscus seen when a liquid wets a solid surface. This restructuring is a 3D phenomenon, as seen on the figure (1.19.b), which alters the local membrane thickness. In the thickness matching process, a transverse elongational or compressive work is balanced with a reduction of the interfacial hydrophobic energy [20]. It is therefore legitimate to consider that the local lipid environment of an inclusion may differ significantly, in terms of lipid composition or lipid tail elongation, from the average membrane state.

The need of accommodating several different proteins may be one of the reasons behind such a diversity of lipid compounds in a real membrane. Similar issues arise when it comes to design nanocarriers with optimal membrane interactions.

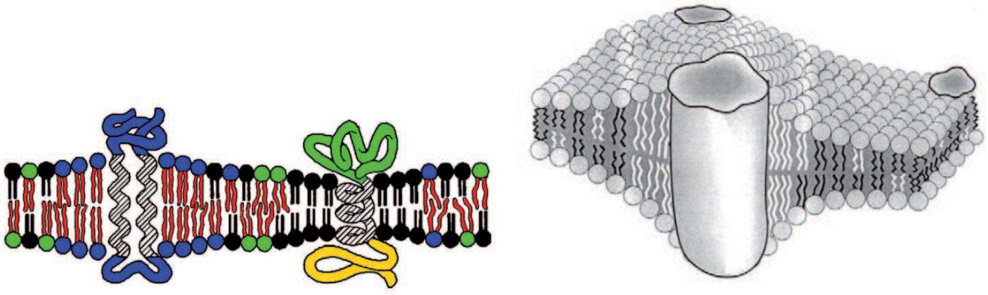

(a) Schematic hydrophobic mismatch in a lateral cut view.

(b) Schematic hydrophobic mismatch in a 3D view.

Figure 1.19 – *Hydrophobic mismatch[21].*

Rafts

This lipids reorganization accompanying protein inclusions is believed to induce domains with specific lipids and electrostatic bonding that could act as receptors for signaling an entrance point in the cell. Domains could be formed with 40 to 80 lipids molecules, depending on the associated protein diameter [6]. The presence of very small lateral structures in biological membranes, called rafts, is currently a domain of intense speculations and investigations, because it could be a key ingredient of the signalling and endocytic pathway across cell membranes [22].

Up to now, these structures were not put in evidence because of their nanometric length scales, and because of the difficulty to demonstrate that a lipid or a protein is indeed confined into a such a tiny and transient region of the membrane surface (1.20). These rafts are composed of cholesterol and sphingolipids with long, saturated, elongated chain tails, similar to some extent to the liquid ordered phase L_o seen in mixtures of saturated PC and cholesterol. These domains are believed to be significantly thicker than the rest of the membrane. They should therefore accommodate preferentially proteins with extended hydrophobic domains and peripheral proteins with grafted long hydrocarbon tails.

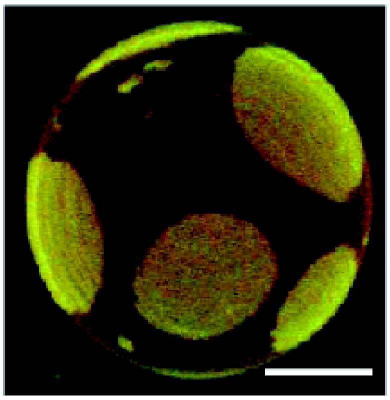

Figure 1.20 – *Confocal fluorescence microscopy in ternary mixture DOPC/DPPC/Chol in which fluid-ordered/fluid-disordered (round domains) phases coexist [23].*

1.3 Main phase transition ($L_\beta \to L_\alpha$)

We can notice on Table (1.2) that pure lipids transit at a well defined temperature T_m from their gel phase to their fluid phase. This transition is first order, characterized experimentally by a narrow peak of calorific capacity (figure 1.21), associated with a finite enthalpy of transition ΔH. Saturated lipids such as DPPC, DLPC, or DMPC have a significantly higher transition temperature than unsaturated lipid such as DOPC or POPC. This is a consequence of the poor packing properties of the *cis*-unsaturated chains (kinks) which lower the stability of the low temperature phase.

Lipid formula	T °C	ΔH kcal/mol (kj/mol)
DOPC	-21	7.7 (32.2)
DPPC	41.5	8.7 (36.5)
POPC	-3	5.4 (22.6)
PSM	41	7.5 (31.4)
DPPC-d62	37.8	8.7(36.5)
DiphyPC	-120	7.4 (31)
DSPC	55.5	10.6 (46)
DMPC	23.5	6.2 (26)
DMPE	49.5	5.8 (24.3)
DLPC	-1.8	4.8 (20)
DPPE	63	8.8 (36.8)

Table 1.2 – *Transition temperatures and enthalpy changes for selected pure lipids.*

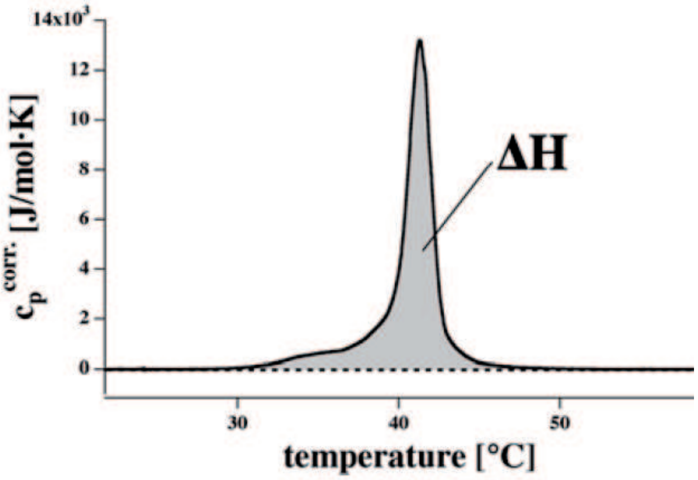

Figure 1.21 — *Heat capacity as a function of temperature (adapted from [19]).*

1.3.1 Binary systems phase diagrams

As a rule, a binary lipid mixture at a temperature comprised between the two pure species melting temperatures is subject to demixing, or equivalently, phase separation. Binary separation is driven by the competition between two antagonistic effects: the entropy of mixing which favors homogeneity and the enthalpic interactions which favors the aggregation of likewise molecules. In the precise case of binary lipid mixtures, the repulsive interactions originate from the incompatible packing properties between the high temperature melting lipids which tend to adopt an ordered gel-like conformation and the low temperature melting lipids which adopt a disordered fluid-like conformation. The chemical mismatch between insaturated and saturated chains comes as an additional interaction term.

We can observe this mechanism at work on the DOPC/DPPC-d62 phase diagram, represented on figure (1.22), and which shows a phase separation between the upper and lower transition temperatures of the lipids (between −21°C and 37.8°C).

The coexisting phases are a gel phase containing an excess of high melting point lipid species (compared with the average mixture composition) and a fluid phase depleted in the same compound. The respective amount of gel and fluid obeys the thermodynamic lever rule.

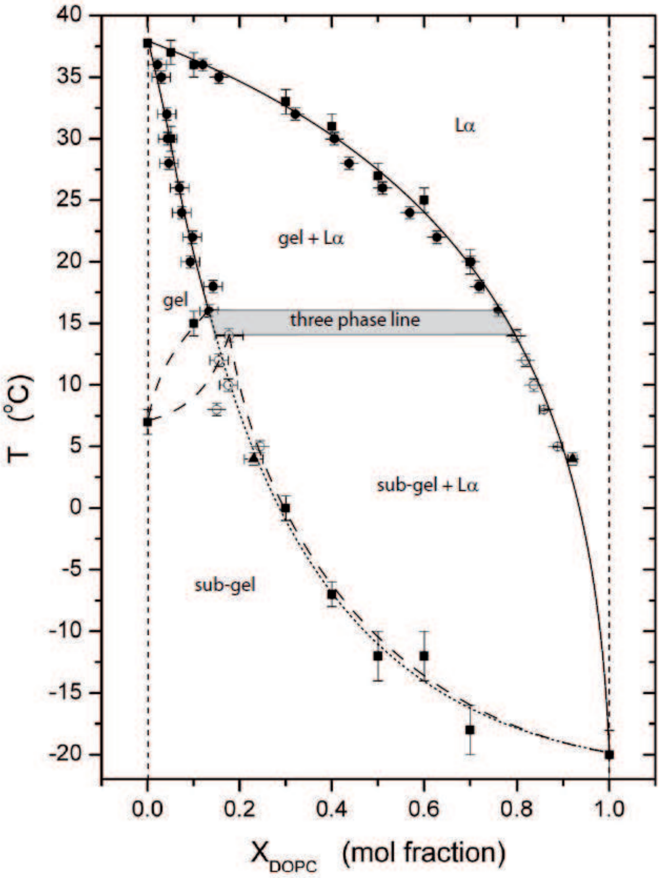

Figure 1.22 – *Binary lipids mixture diagram DOPC/DPPC[24].*

1.3.2 Lipid-cholesterol binary phase diagrams

The binary mixture lipid/cholesterol is one of the most important topic in lipid science with regards to the central role of cholesterol in membrane cell biology. Cholesterol is unique in its ability to stabilize the liquid ordered phase L_o, along with only a few other higher sterols, such as ergosterol.

Cholesterol is a small molecule compared with usual phospholipids, it occupies only half of the area of a phospholipid (about 0.40 nm^2). It inserts in the fluid disordered phase more easily than in the tightly packed gel ordered phase. As a matter of fact, gel phases can only accommodate tiny amounts of cholesterol. On the other hand, the stiff and planar steroid rings interact more favorably with the elongated lipid tails than with the disordered conformational chains that dominate the L_α phase. Therefore, cholesterol has a tendency to increase the amount of order in the surrounding chains, thereby favoring the emergence of an intermediate fluid but axially ordered environment, the liquid ordered phase L_o. Beyond this basic principles, the existence of specific favorable interactions with some species (sphingolipids for instance) and unfavorable interactions with insaturated lipid chains complete this complex picture.

Cholesterol is twice a shorter molecule than phospholipids and it promotes a tilting of the molecules around it to prevent the water intake in the membrane. This effect is called *umbrella effect* [25, 26] (see section 1.5.4 below).

There are both experimental and theoretical evidences that the preference of cholesterol for a locally ordered environment is strong enough to promote a real binary phase coexistence, in which cholesterol accumulates into L_o regions. The striking feature of the ordered regions is that cholesterol preserves a high lateral mobility of the membrane components, similar by a factor 2 to the mobility in the disordered phase. This is in stark contrast with the gel phase mobilities which are so low that the overall phase seems almost solid.

We present on figure (1.23) an experimental DPPC-d62/Cholesterol phase diagram, and on figure (1.36) another measurement above the transition temperature of DPPC-d62 (deuteration is required for NMR studies). We observe a coexistence between two fluid phases above the phospholipid main melting transition temperature T_m. We also see that the liquid ordered phase is not subject to a melting phenomenon at T_m. First the binary coexistence bubble ends in a critical point (upper critical solubility transition) which marks the convergence of the two fluids region. It is worth mentioning, however, that other recent observation denied the existence of fluid-fluid coexistence in binary systems, allowing only for gel-fluid coexistence below the melting temperature T_m (see figure 1.37).

1.3.3 Ternary mixture of lipids and cholesterol

The existence of fluid-fluid domain coexistence is non ambiguous in the case of ternary mixtures, as if the third component was enhancing the trends towards domain formation. Quite naturally, these ternary lipid systems have been considered as canonical raft forming mixtures, speculating on the connexion between liquid ordered phase and biological raft domains. Another reason to consider ternary mixtures is the need to simplify the complex composition of biological membranes in order to disentangle the respective contribution of each lipid species. There is, obviously, a limit in what membranes of artificial composition can reproduce, in the absence of active processes or biochemical transformations. Nevertheless model systems have proved valuable for structural and mechanical investigations.

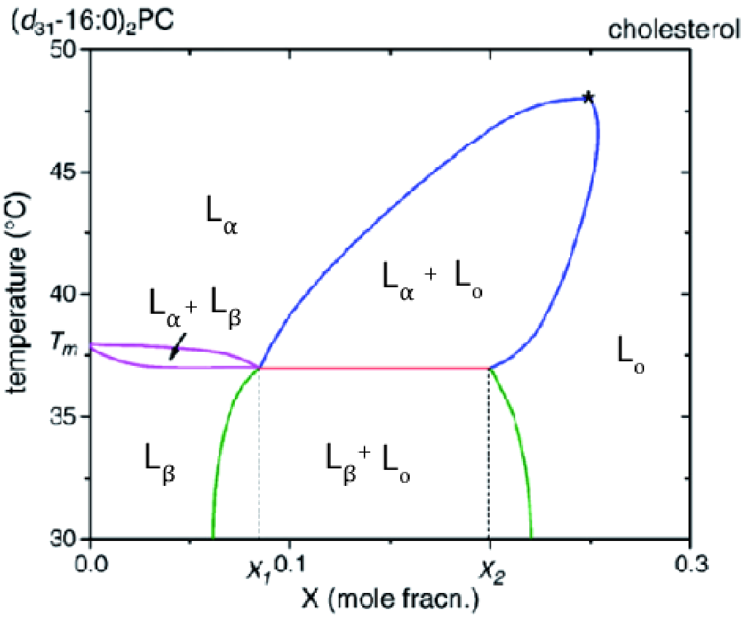

Figure 1.23 – *Binary lipid mixture DPPC-d62/Chol diagram. The asterisk indicates the approximate location of the critical point [27].*

Canonical raft mixtures are composed of a low melting point lipid, a high melting point lipid and cholesterol. Low melting point lipids often present unsaturated chains while high melting point lipids have saturated chains. We show on figure (1.24) the Gibbs triangle representation at a fixed temperature of a ternary mixture of lipids and cholesterol. Usually, the unsaturated lipid is placed at the left corner of the triangle and the saturated species at the right corner, while the cholesterol is located on top.

Each side of the triangle is an isothermal cut-line of the binary phase diagram of the two species located on this side. One distinguishes on the Gibbs diagram a triple coexistence zone (triangular shape) surrounded on its upper left side by a “bubble” of binary fluid L_d-fluid L_o coexistence, ending at a critical *plait* point. On the lower and right sides of the triple coexistence domains are two binary coexistence regions between L_d and L_β and between L_o and L_β respectively. To establish the ternary coexistence diagram, the GUV were observed by confocal fluorescence microscopy with selective probes showing the fluid phase as green and the gel phase as red. The boundary between domains depends on temperature.

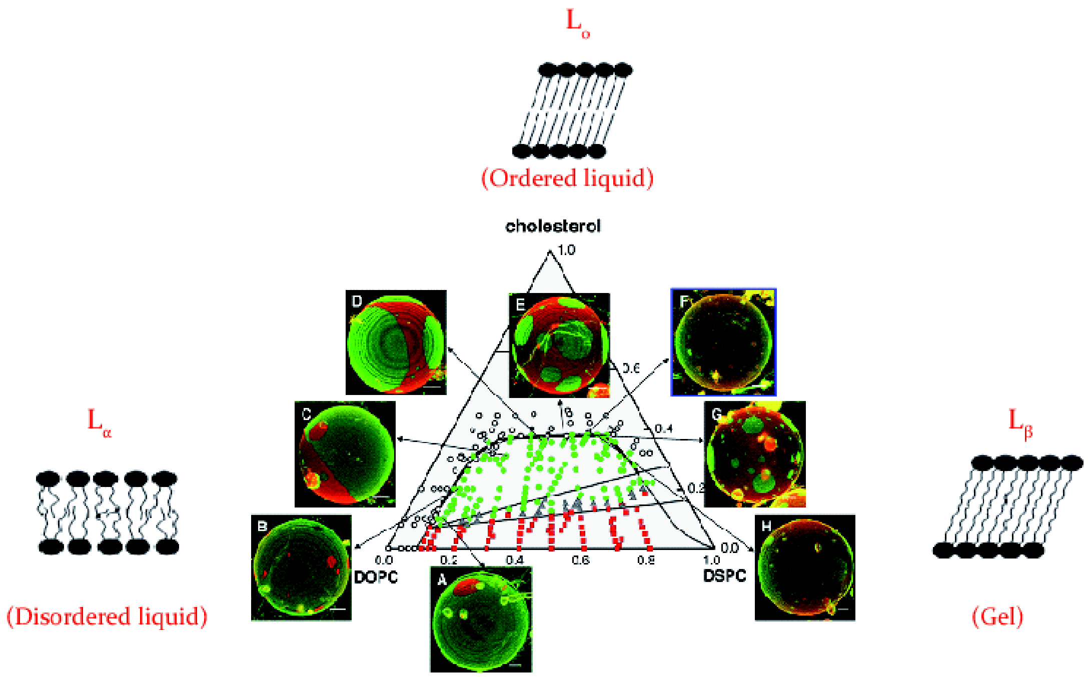

Figure 1.24 – *Ternary mixture of lipids and cholesterol. GUV images reveal the upper and side boundaries of* $L_\alpha + L_o$. *Samples range from mostly* L_α *(green, A–C) to mostly* L_β *(red, G and H). Vesicles close to the top nearly horizontal boundary (D, E and G) change abruptly to uniform (e.g., F) with a small addition of cholesterol (0.5 mol% more cholesterol from panel G to F). GUVs were prepared by gentle hydration[28].*

1.3.4 Phase transitions in membrane

Phase transition is an ubiquitous phenomenon which describes the sudden switching between two states of organization, characterized by some kind of internal order: spin orientation in magnetism, atomic positions in melting processes, lateral arrangement of lipid headgroups and elongation of lipid chains in lipid bilayers... Phase transitions belongs to two different classes, following Ehrenfest, either first order or second order.

A first order transition is a discontinuous phenomenon, with coexistence of two phases at constant temperature, and an associated latent heat due to a finite jump in the specific entropy and enthalpy of these two phases. The heat capacity (second derivative of the free energy) can be assimilated to a singular Dirac distribution. Well known examples are the melting and boiling transitions of pure species.

A second order transition is a more continuous process with no latent heat and a single, though strongly fluctuating, state throughout the system. The presence of a critical point at the transition temperature is the hallmark of second order transitions. At the vicinity of the critical point, the calorific capacity scales as $C(T) \approx C_0 + |T_c - T|^{-\alpha}$ with a critical exponent $\alpha < 1$ (as the singularity in $C(T)$ remains integrable). Other system susceptibilities show similar divergences and singularities. The paramagnetic/ferromagnetic transition (Curie-Weiss temperature) and the liquid-vapor critical point are well known examples.

In membranes, we can observe several phase transitions of DPPC between the low temperature crystalline phase L_c and the liquid disordered phase L_α, schematically depicted on figure (1.25). These transitions are easily put in evidence by means of calorimetric measurements, as showed on figure (1.26), where we see first the small peak of the *pretransition* between the tilted gel phase $L_{\beta'}$ and the ripple phase $P_{\beta'}$, and then the large peak of the main transition between the ripple phase and the fluid phase L_α. Not shown is the *subtransition* between the crystalline phase L_c and the gel phase $L_{\beta'}$. This sequence of transitions is typical from PC headgroups.

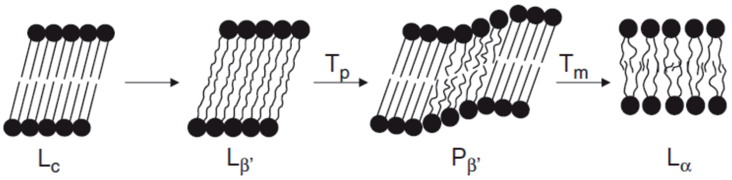

Figure 1.25 – *Schematic representation, according to T.Heimburg, of lipid bilayer phases at different temperatures:* L_c *crystalline phase,* $L_{\beta'}$ *gel-phase (tilted phase),*$P_{\beta'}$ *ripple phase,* L_α *liquid disordered phase.* T_p *and* T_m *denote the pretransition and the main transition temperatures respectively [29].*

The picture is notably different when the membrane is a binary mixture, with an enlargement of the calorimetric peak between the two main melting temperatures. In ternary lipid mixtures, calorimetry alone cannot provide a determination of the phase coexistence regions. Figure (1.27) shows a simulated lipid system with domains which are good raft candidates.

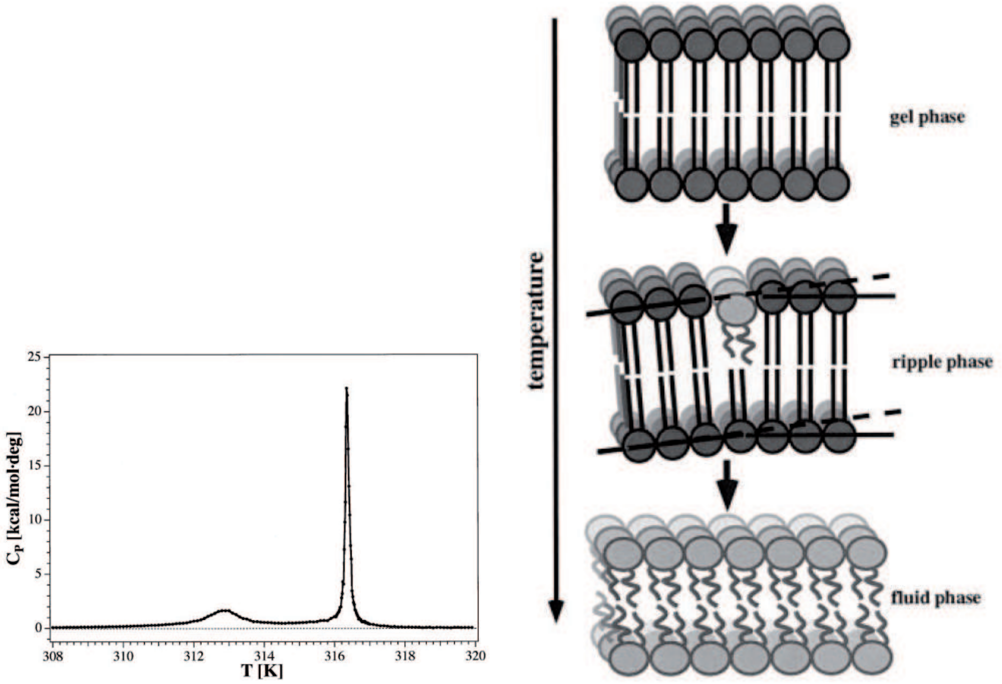

Figure 1.26 – *Calorimetric peaks of the pretransition and the main transition [30].*

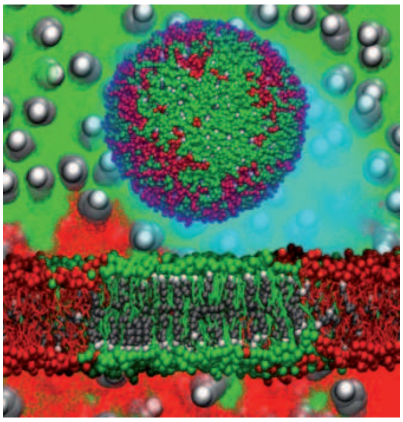

Figure 1.27 – *Simulation of a raft in the framework of the coarse-grained Martini model [31].*

1.4 Experimental methods

In lipid science, there are several methods to investigate the membrane properties, and we present below the principles and the validity domains of some of the most useful ones.

1.4.1 X-ray diffraction and neutron scattering methods

Scattering methods rely on the interaction between an incident wave and a sample to determine its structure and dynamics. The scattered wave contains an elastic and an inelastic contribution. The inelastic component probes the dynamical changes in the sample, while the elastic part measures the static, equilibrium structural properties. We restrict the discussion to the elastic scattering, which preserves the energy $\hbar\omega$ of the scattered wave, and gives access to spatial correlations in the sample.

X-ray and neutron scattering are two essential methods to determine the membrane structure, and are often used together to refine the results.

In small angle X-ray scattering (SAXS), the variation of the wave vector is small and reveal structural features of the order of 1 nm or more, *i.e.* the order of magnitude of the bilayer thickness. At the opposite, wide angle scattering (WAXS) probes smaller length scales, but cannot be used on the highly disordered fluid membrane structures. However WAXS is useful for studying low temperature gel or crystalline phases, where hydrocarbon chain tails packing details can be resolved [32].

Small angle scattering can be performed on oriented lamellar phases or small unilamellar vesicles (SUV). X-ray interact mainly with electrons, and probe the *electronic density profile* (EDP) distribution. Neutrons interact with nuclei, which are spatially less extended, and reveal a *scattering length density* (SLD) distribution. Neutrons and X-rays are therefore complementary, as strong neutron scatterers and strong X-ray scatterers are very distinct: X-ray interact strongly with heavy atomic elements, while neutrons are strongly scattered by hydrogen nuclei. Neutrons offer the possibility to match the bilayer-solvent contrast by means of selective deuteration of the lipids. X-ray have a short penetration length and are used for surface studies while neutrons penetrate the bulk, so that they are used also for volumic investigations. Finally, X-ray beams are much more intense than neutrons beam, resulting in different irradiation times and damages.

The outcome of a scattering experiment consists in the determination of the structure factor $F(R)$, by measuring the intensity $I(R) \approx |F(R)|^2$ of the scattered wave. The incident wave (with wave vector $\vec{k}_i$) hits at the sample and is diffracted as a new wave (wave vector $\vec{k}_s$) in a direction forming an angle 2θ with the incident direction, with a transfer momentum $\vec{R} = \vec{k}_s - \vec{k}_i$ (figure 1.28). The structure factor $F(R)$ is the Fourier transform of the electronic density profile $\rho(\vec{r})$. Different distributions $\rho(r)$ can be tested, until agreement with the experimental $|F(R)|$ is obtained.

$$\rho(\vec{r}) = \int F(R) e^{-i\vec{r}.\vec{R}} \mathrm{d}R \tag{1.3}$$

On figure (1.29), the electron density profile of a DMPC bilayer at a fixed temperature is shown. We notice the two main peaks associated with the phosphate groups, a plateau for the double-chain methylenes on each side of the bilayer and a central hole at the terminal methyls. The electron density profile in the gel (L_β) phase shows a pair of distinct secondary peaks.

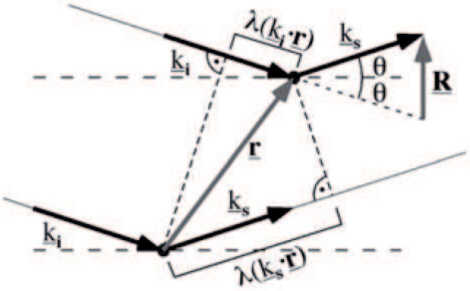

Figure 1.28 – *X-ray or neutron scattering by two points in a plane [19].*

Neutron scattering probes the so-called scattering length density profiles, which depend on which nuclei isotopes are presents in the solvent and the bilayer. Combining electron density profiles and scattering length density profiles allows for the determination of the main structural informations: bilayer thickness and area per lipid for instance.

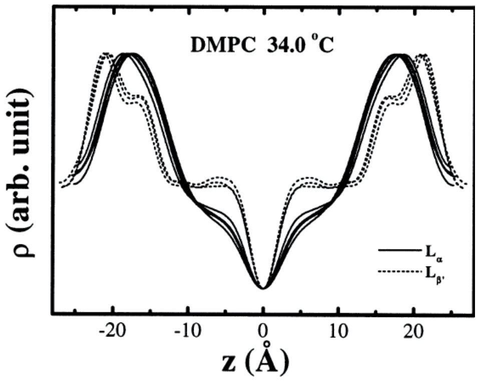

Figure 1.29 – *Electron density profiles of a DMPC membrane for different phases[33].*

Finally, neutrons and X-rays can be used for reflectivity studies. In this set-up, a beam is sent on a thin layer oriented on a flat surface, and the reflected beam gives the structural information. The specular reflectivity corresponds to a reflection angle equal to the incident angle (Descartes reflection) and probes the electron density or the scattering length density in the direction normal to the surface, in good agreement with small angle diffusion results. Off-specular diffusion gives access to the out-of-plane fluctuations of the bilayer (roughness) which is linked with the mechanical properties of the bilayer [34, 35].

1.4.2 Nuclear Magnetic Resonance (NMR)

NMR determines the chemical compositions and the molecular orientations by using the dynamic properties of nucleus subject to a strong magnetic field. A nuclear magnetic moment μ with a non-zero spin I put in a magnetic field B_0 has $(2I + 1)$ energy states. For instance, the nuclear spin of hydrogen is $I = \frac{1}{2}$, so that the magnetic moment shows two orientations separated by a gap in energy ΔE, proportional to the product of the gyromagnetic ratio γ and the magnetic field B_0. The nuclear magnetic resonance is obtained by applying an additional time-dependent orthogonal magnetic field B_1 which leads to transitions between these two levels. Two identical nuclei in two different environment gives different peak positions (chemical shifts). The NMR relaxation signal depending on the different ΔE is treated with a Fourier transform, and gives characteristic peaks relative to each nucleus.

NMR studies of lipid bilayers belong to a class of solid state techniques because lipids have very slow orientational dynamics. This downgrades the resolution of the NMR spectra and makes the use of the technique very challenging. NMR can be usefully applied to ^{31}P nucleus naturally present in glycerophospholipids.

However, the most striking use of NMR concerns the deuterated lipid compounds, for which a special phenomenon called deuterium quadrupolar splitting provides very accurate information on the lipid ordering with respect to the magnetic field. Deuterium, which has a nuclear spin 1, is sensitive to the relative orientation of the chemical bond C-D with the applied field B_0. This averaged orientation of the bond C-D is encoded in an order parameter S_{CD}, called NMR order parameter [36], and similar to the order parameter of a nematic liquid crystal.

Figure (1.30) shows two NMR spectra of a cholesterol-DOPC-DPPC mixture.In the first case, the spectrum was done with deuterated cholesterol-d1, and in the second case with perdeuterated DPPC-d62. The mixture at 25°C has a phase separation, with two L_o and L_d phases, and a single phase above this temperature.

Well oriented C-D bonds lead to wide NMR signals. The orientation is better in the gel or liquid ordered phases than in the disordered fluid phases, so that each phase has a clear spectroscopic signature. In the presence of coexistence, and provided the domains are large enough, the spectra can be decomposed into contributions proper to each participating phase. In the case of small domains, the diffusional exchanges are so fast than the signatures of the two phases disappear leading to a composite spectrum.

Veatch et al. [37] determined a phase diagram by means of NMR spectra, a few of them being represented on figure (1.30). At a temperatures above 25°C, there is only one phase and the deutered cholesterol presents a standard quadrupolar spectrum with a weak signal due to the single deuterium label on the molecule (a). At a temperature below 25°C the phase separation temperature, cholesterol presents two peaks since the existence of two phases because its different orientations in the two phases(b). Above the transition temperature the methyl groups are well mixed in the membrane, and all the groups share the same average environment, leading to a superposition of about the same signal with a small splitting (c) while below 25°C the middle methyl group peak (d) split due to the difference of environment between the two phases.

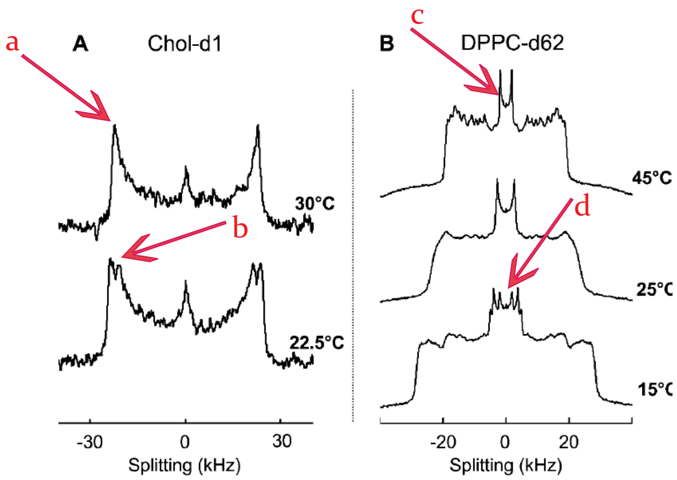

Figure 1.30 – *NMR spectra for 1:1 DOPC/DPPC + 30% Chol-d1 (A) and for 1:1 DOPC/DPPC-d62 + 30% Chol (B) (adapted from[37]).*

1.4.3 Fluorescence microscopy

Fluorescence techniques such as SPT (simple particle tracking), FRET (fluorescence resonance energy transfer), FCS (fluorescence correlation spectroscopy), and FRAP (fluorescence recovery after photobleaching) are currently used to visualize lipid domains and phase separations, to measure diffusion coefficients and fluctuations. We give hereby a brief overview on fluorescence techniques, and point out their use for the characterization of phase separations.

Many of these fluorescence methods use confocal microscopes, based on a very small depth of field given by a pinhole which leads to a plane by plane scanning, allowing for a 3D image reconstruction. Confocal microscopy provides a unique way of visualizing domains in 3D.

Single particle tracking

SPT is based on the observation of a fluorescently labelled particles, such as proteins, in a membrane to determine their diffusion behavior. Their trajectories provide information on the interactions that drive the particle motion. This technique yields properties lateral mobility and diffusion coefficients. For example figure(1.31) shows the motion of charged nanoparticles on the cell surface, tracked by SPT, and gives information on lipid headgroups-particles electrostatic interactions.

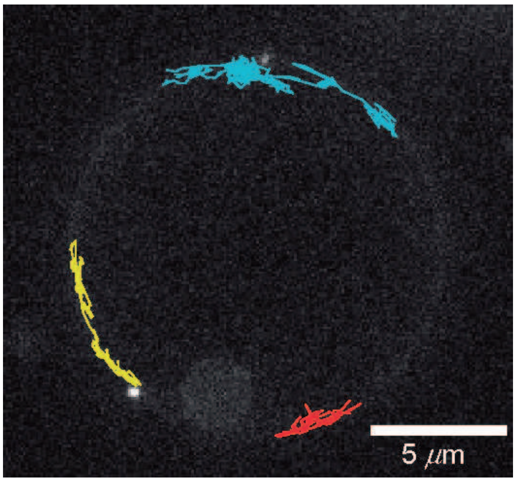

Figure 1.31 – *Trajectories of three fluorescent-labeled nanoparticles, indicated in different colors on a GUV surface[38].*

FRET

The FRET phenomenon consists in a non-radiative energy transfer between two fluorophores, a donor and an acceptor, due to electromagnetic dipole-dipole coupling.

In order to interact, it is necessary that the emission spectra of the donor overlaps with the absorption spectra of the acceptor, and that the fluorophore separation remains under a critical distance called Förster radius R_F. Förster radii are all in the range 1 to 10 nm.

Special fluorescently labelled lipids must be chemically prepared in order to target specifically one of the lipid phase. For instance, J.Silvius used the 7-nitrobenz-2-oxa-1,3-diazol-4-yl (NBD)-labeled tetraacyl lipids as donor, and a rhodaminyl-labelled acceptor [39]. When the donor transfers its energy to the acceptor, the acceptor radiates according to its own emission spectrum, leading to a significant spectroscopic change in the fluorescent signal (figure1.32). Roughly speaking, the color of the secondary fluorescent emission changes, and is red-shifted.

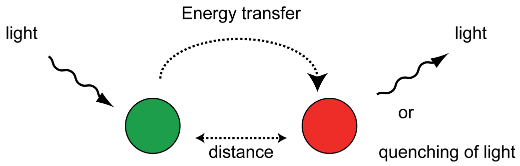

Figure 1.32 – *The donor (green) looses its energy in favor to the acceptor (red).*

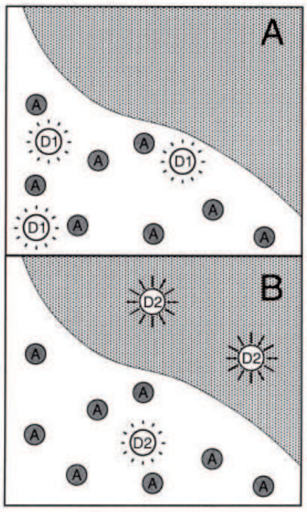

Figure 1.33 – *FRET mechanism with one acceptor matched with two donors[39].*

One can investigate lateral inhomogeneities in membranes by the FRET technique by using two donors D_1 and D_2 matched with the same acceptor A. The idea is illustrated schematically on figure (1.33).

Two domains are represented in black (disordered phase) and in gray (ordered phase). The acceptor A and the donnor D_1 have a strong preference for the disordered phase, while the donnor D_2 has a clear preference for ordered phase. The affinity of donors and acceptors for each phase depends on the chemical structure, and must be carefully checked experimentally. In the situation A, donors and acceptors are spatially close and homogeneously mixed (figure 1.33(A)). Energy transfer is efficient and the signal associated with the donnor is significantly reduced. In the situation B, donors and acceptors are spatially separated, except at the vicinity of the boundary between domains (figure 1.33(B)), and the energy transfer is inefficient. The fluorescence efficiency of the two samples can be measured, and the reduction of the donor fluorescence efficiency (quenching) is interpreted as an evidence of domains of nanometric size.

Fluorescence labelling of domains

Fluorescence is often used as an evidence for phase separation phenomena in giant vesicles. In the case of ternary mixtures of lipids and cholesterol, it is possible to discriminate liquid ordered phases and liquid disordered phases with different probes having their own color and phase preference. It leads to colored domains at the vesicle surface, and allows for identification of the domain boundaries between binary and ternary coexistences in the Gibbs diagram (figure 1.24). We can see on figure (1.34) a vesicle composed of DOPC, sphingomyeline and cholesterol subject to phase separation, labelled by two probes, one of them preferring the ordered liquid phase and the other the disordered liquid phase. Such images of domains were seen for the first time by Bagatolli et al. [40]. Since then, it has become a method of choice for studying domain coexistence and lateral separations in giant vesicles.

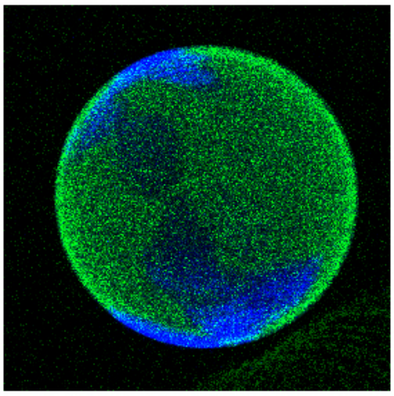

Figure 1.34 – *Labelling phase separation on a vesicle surface [41].*

1.4.4 Differential Scanning Calorimetry (DSC)

We show on figure (1.35) the principle of a DSC apparatus which measures the heat capacity with respect to the temperature, and allows to determine the enthalpy jump at the transition. We can notice the reference-cell which contains water or buffer, the cell which contains the sample, and the heating and temperature control system. The apparatus scans in temperature the two cells, and always keeps the temperature difference between the two cells equal to zero. In order to have the same temperature in the two cells, the system heats the sample-cell to compensate for the heat absorbed or released upon melting, and finally plots this supplied heat as a function of temperature (figure 1.21). The area under the thermal capacity peak is the enthalpy of transition at melting. DSC is an universal technique for detecting structural changes induced by temperature variations. This is because all phase transitions are associated to specific heat anomalies.

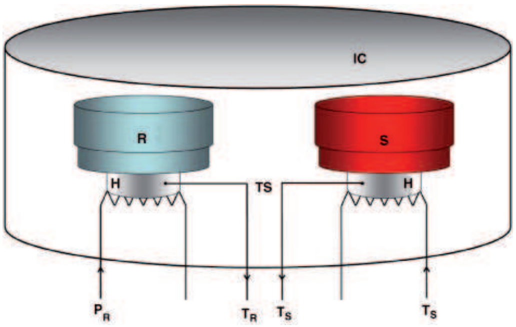

Figure 1.35 – *DSC apparatus: S, sample cell; R, reference cell; H, heating coil; IC, insulating casing;* T_S*, temperature sensor;* T_S *and* T_R *are the currently measured temperatures in sample-and reference cell and; (*P_R*; left) and (*T_S=P_S*; right) are the heat output for the reference and sample cell [42].*

1.5 Theoretical study of binary and ternary mixtures: the state of the art

1.5.1 Transition liquid/gel for one lipid

The first theoretical investigations on membrane behavior started with Whittigton [43] and Chapman [44] with Monte-Carlo simulations on the hard-core repulsion effects and carbon chain packing in different isomeric states, for which they found that chains can rotate in the case of low molecular density. Afterwards, J.F Nagle [45] in 1973 proposed a statistical model of the lipid membrane, assuming that the excluded volume interactions and conformational change of lipids (kinks) are the main driving factors of the melting transition. He built a microscopic model taking in account the details of bond/bond orientations. He considered long chains and repulsive interactions between molecules located on a lattice. These assumptions were pointing to a phase transition.

S.Marcelja in 1974 [46] considered the attractive interaction between chains, with a phenomenological orientation potential inspired by nematic liquid crystals concepts. He showed that although the transition is of first order, it is close to a critical point and could be a second order transition. The same year D. Marsh [47] proposed an explicit statistical calculation of the different rotation isomers along the carbon chains, and calculated enthalpies and entropies in the fluid state. He could also estimate the enthalpy change at the transition.

In 1975, H.L.Scott [48] and R.E.Jacobs et al. [49] estimated the partition function of the excited states of the molecular chain in a molecular field representing the Van Der Waals chain-chain, headgroup dipolar attractive forces and the sterical repulsion forces.

In 1978, S. Doniach [50] took into account that the transition is close a critical point [46] and mapped the problem onto a 2d Ising model under low magnetic field. By doing so, he neglected the positional degrees of freedom at the transition (0.5 k_BT per molecule) compared with the contribution of intrachain melting entropy (14 k_BT per molecule). Secondly, he lumped together all the excited states into a single representative state whitout the microscopic molecular details of the chain, using Ising variables with two order/disorder states. This amounts to considering that at the transition, the chains move from a rigid and long state to a kinked and short state. At the same time, Caille et al. [51] introduced a two states Ising-like model including Van der Waals interactions.

In 1988, J.H.Ipsen and O.G.Mouritsen [20] proposed a thermodynamical model, based on a regular solution approach, and where the interaction parameters between species with same headgroups but different tail lengths are inferred from mechanical stresses and hydrophobic mismatch considerations. In particular bilayer thickness variations are found to depend on the membrane stretching coefficient. They obtained very accurate binary phase diagrams with only one adjustable parameter, and the extension to mixtures of different headgroups were quite satisfactory as well.

In 1989, R.Goldstein and S.Leibler [52] introduced a Landau model with an order parameter $\psi = \frac{\delta-\delta_o}{\delta_o}$ related to the membrane thickness, δ_o standing for the equilibrium thickness of the membrane in its liquid phase, and δ being the actual membrane thickness. They obtain a phase diagram for multilamellar meso-phase structures, accounting for hydration effects and direct interactions between membranes.

1.5.2 Binary mixture of lipids

A.G.Lee, in 1977 and 1978 [53, 54] was the first to calculate diagrams of binary lipids mixtures. These were obtained with a theory of regular solutions, *i.e.* considering the entropy of mixing of an ideal solution plus an adjustable parameter for describing the non-ideality of the mixture. Shortly after, Simon et al. [55] showed that the regular solution model is not satisfactory for lipids membranes, based on a partition coefficient argument.

In 1980, R.G.Priest [56] proposed a Landau [57] phenomenological model with an order parameter S related to the fraction of gauche bonds in the aliphatic chain tails. Thanks to a number of adjustable parameters, he fitted binary diagrams for the PC sequence of lipids. I.Sugar and G.Monticelli [58], in 1983, extended the Priest model to lipids with different headgroups and obtain several other binary diagrams.

1.5.3 Binary mixture of lipids with cholesterol

The experimental approach of M.R.Vist in 1984 [59] on mixtures of cholesterol and lipids, using deuterium NMR spectroscopy, improved by M.R.Vist and J.H.Davis in 1990 [60] gave the binary diagram for a cholesterol/DPPC mixture (figure 1.36). Their diagram clearly displays a fluid-fluid coexistence above the DPPC melting temperature.

Based on such results, H.J.Ipsen et al. introduced a statistical model for binary

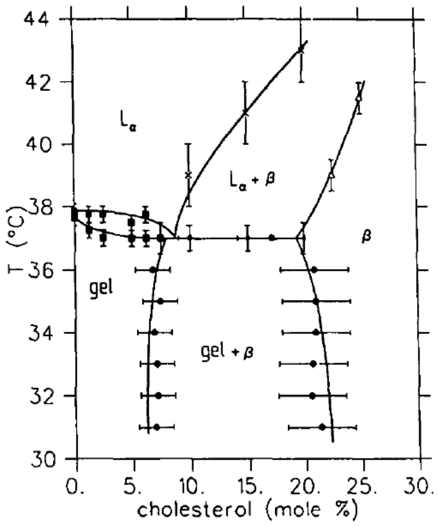

Figure 1.36 – *Partial phase diagram for cholesterol/DPPC mixtures.*

cholesterol-lipid mixtures which was able to reproduce the main experimental trend [61]. This very important study opened a new era in lipid understanding because they experimentally brought to light the ordered liquid phase L_o, or L_β, induced by specific cholesterol/lipid interactions.

The initial observation of H.J.Ipsen et al. was that the lipid main transition consists in a simultaneous elongation of the chain tails and ordering of the lipid center of mass, but that these two phenomena could under some specific circumstances be dissociated. In the presence of two distinct transitions, an intermediate phase, elongated along the bilayer normal direction, but still disordered in the lateral directions could exist, which was named liquid ordered. Cholesterol was then seen as the element provoking this dissociation.

Their model is a lattice gas with two order parameters, one for the tails order (ordered or disordered liquid), and one for the relative positional order, modeled with a 10 states Potts variable (symmetric liquid phase or symmetry broken solid phase) and a number of coupling parameters to fit the data. They considered that cholesterol interacts favorably with the liquid phase, but disturbs ordered solid states (the gel phase). Note that in 1995, T.MacMullen and R.McElhaney [62] proposed a new DPPC/Cholesterol binary diagram using DSC (figure1.37), in partial disagreement with the previous work of Vist and Davis [60].

In 1999 Nielsen et al. performed Monte Carlo simulations of binary mixtures of phospholipid and cholesterol, and showed that the insertion of cholesterol in membranes causes a decoupling effect between the two types of order present in the gel phase, which are the lipid-chain crystalline packing (translational degrees of freedom) and lipid-chain conformational ordering (internal degrees of freedom)[63]. Finally, in 1999 Sugar et al. simulated with Monte Carlo a two components lattice model, and reproduced heat capacity curves, and conforted the first order nature of the transition [64].

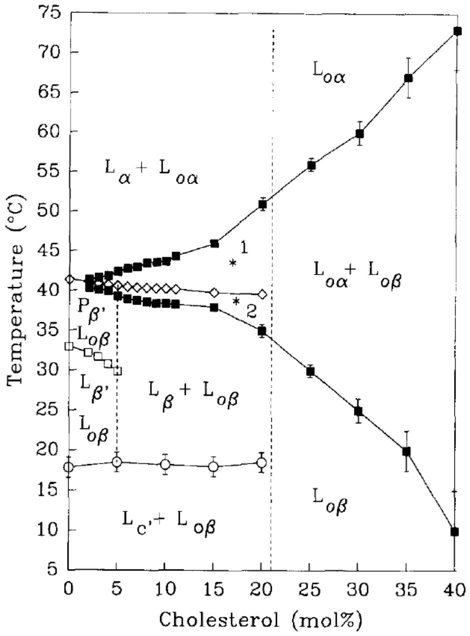

Figure 1.37 – *Phase diagram for cholesterol/DPPC mixtures.*

Following the works of Sankaram and Thompson in 1991 [65] on lipids-cholesterol interactions (NMR and calorimetry), in which they showed that the membrane thickness increases in the presence of large amounts of cholesterol , Komura et al. in 2004 presented a thermodynamic mean field theory [66]. They used an order parameter related to the membrane thickness analogue to the one originally introduced by Goldstein and Leibler [52], in addition to a special interaction term for the cholesterol, interfering with chain melting and assimilable to an external field.

They obtained diagrams for ternary mixtures of saturated and unsaturated lipids and for binary mixtures of lipid and cholesterol. They distinguished the ordered liquid phase L_o and the disordered liquid phase L_d based on the value taken by the order parameter ψ, close to zero in the L_d phase and finite in the L_β phase.

1.5.4 Ternary mixture of lipids and cholesterol

In the early 2000s, Huang, used Monte Carlo simulations to investigate cholesterol super-lattices (highly regular lateral distributions) and showed that this structure necessites multiples interactions and not only pairwise interactions [67] . Moreover, he found that cholesterol super-lattices reveal favorable mixing between lipid and cholesterol but an unfavorable chain multibody interaction which increases with the number of cholesterol contacts. This result is called "umbrella effect" and consists for polar phospholipid headgroups in covering the non-polar cholesterol molecules to shield them from exposure to water, and compensating for the sharp decrease of acyl chain conformational entropy due to the proximity of cholesterol.

Recently, several experimental results on ternary mixtures of lipids and cholesterol were published, such as DOPC/DPPC/Cholesterol by Veatch et al.[37], [68] using NMR and fluorescence microscopy, and PSM/POPC/Cholesterol by Almeida et al. [69] using fluorescence techniques.

Following this results, Komura et al. [70] built Gibbs ternary diagram with three lipids whithout cholesterol in extending the model they used for binary diagram cited above [66].

In 2008, G.Putzel and M.Schick [71] used a phenomenological model with an order parameter δ representing the saturated chain order equal to 0 for unsaturated pur lipid, equal to 1 for saturated pur lipid and equal to 2 for the gel, and parameters to fit the experimental data. They considered three interactions, first the saturated/saturated lipid, secondly the saturated/unsaturated lipid because of their poor mutual packing, and finally the saturated/cholesterol interaction. More recently in 2011, de Joannis et al. [72] showed with the help of molecular dynamic simulations that the affinity of DOPC and DPPC with cholesterol depends on the tilting distribution of cholesterol, confirming that cholesterol has a condensing effect.

1.6 Wetting

1.6.1 Wetting and lipid domain formation

We have reviewed in the sections above how, under certain conditions, two distinct liquid phases can form in a ternary mixture of lipids containing cholesterol, leading to phase coexistence phenomena such as that showed in the figure (1.38) where different coexisting L_o and L_d domains can be seen. Whether or not similar domains can form at the nano-scale has been debated in the literature following publication [73, 74] of the so called raft hypothesis. Lipid rafts, supposedly small lipid domains enriched in cholesterol and saturated lipids such as sphingomyelin would, under this hypothesis, play a crucial role for cell metabolism, contributing for instance to the recruitment of proteins and other biomolecules that initiate cell signalling and other membrane-supported functions. It is thus of prime interest to understand how a lipid mixture reacts to the presence of membrane inclusions such as proteins, the different interactions between the inclusion and the lipids being potentially a factor for a local enrichment of the protein vicinity by certain species of lipids. In three dimensions, the perturbations of local composition changes of liquid mixtures in the presence of interfaces have been studied in the context of wetting. In this paragraph we introduce the reader to wetting and recall some of the theoretical concepts developed to understand wetting phenomena. The concepts will be further developed in Chapter 4 to study two-dimensional wetting phenomena in ternary lipid mixtures.

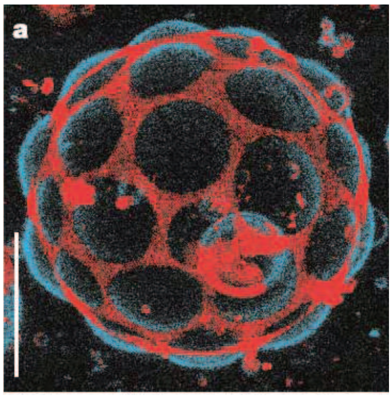

Figure 1.38 – *Two-photon microscopy images of GUVs with L_o and L_d phase coexistence [75].*

Wetting phenomena is related to the very general issue of spreading of a liquid on a solid or a liquid surface or to the adhesion between two solids such as the adhesion that explains the peculiar properties of the gecko when it walks on a vertical wall (fig 1.39). A water droplet deposited on a substrate can either totally or partially spread or remain just as a droplet . Partial or total spreading of the droplet is named respectively partial-wetting or complete-wetting. The same phenomenon can be seen in a capillary filled with a liquid, where we can observe that the liquid climbs in the tube, the raising level depending on the interactions between the liquid, the air, and the glass (fig 1.39). When a droplet is deposited on a substrate (fig 1.40),

Figure 1.39 – ***Left***:*A geko on a sheet;* ***Center***:*Partial wetting of water droplet on a plant;* ***Right***:*Water in a capillary.*

wetting results from the balance of its weight and the three line tensions γ, γ_{SL}, and γ_{SG} acting at the triple line. There is a competition between two opposite aspects. On one hand, the affinity between the droplet and the substrate which tends to spread the droplet by reducing its energy and on the other hand the extension of the liquid/gas interface which requests a surplus of energy.

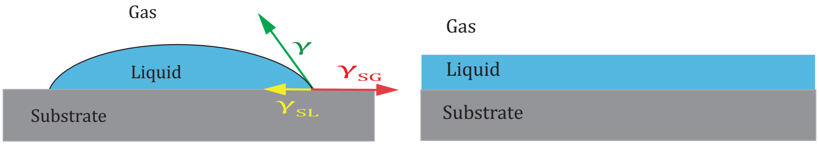

(a) Partial wetting. (b) Complete wetting.

Figure 1.40 – *Water droplet on a substrate.*

When one considers off-coexistence systems, such as a stable phase of a binary mixture of liquids where we insert a inclusion (for instance a colloidal particle) with curvature radius R, the interactions between the colloidal particle and the liquid might result into preferential wetting of the colloidal surface by one of the liquids. Under certain conditions, one can observe strong changes in the nature of the liquid layer that wets the colloidal surface as a function of temperature, a phenomena called a wetting transition. Such transition is characterised by the enrichment and growth of the interfacial layer domain as the temperature changes. In membranes prone to liquid-order liquid-disorder coexistence, an inclusion inserted in a homogeneous phase close to the coexistence boundary – see fig 1.41) – might induce the formation of a two-dimensional wetting layer around the inclusion. The changes of composition and thickness ξ of the wetting layer with temperature or with inclusion radius R can be studying with the framework of wetting theory.

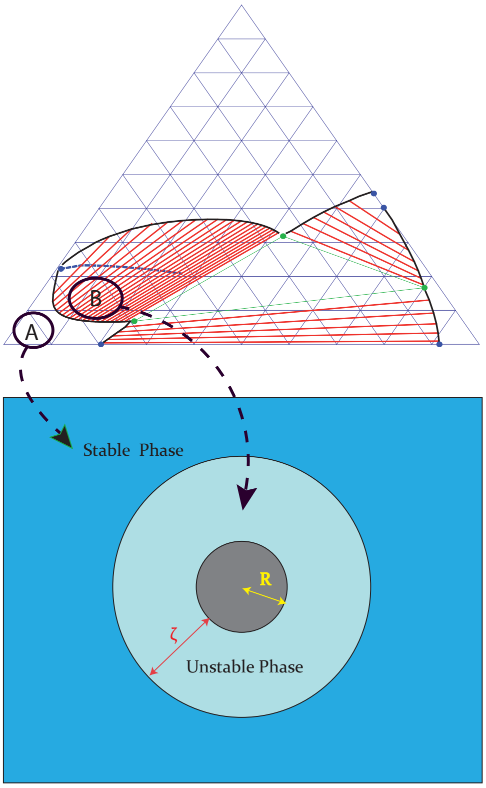

Figure 1.41 — *Pre-wetting of width ξ surround a circular inclusion in a stable phase (corresponding point A in the diagram) of radius $\boldsymbol{R}$ by an unstable phase (corresponding point B in the gibbs diagram).*

1.6.2 Wetting theory for a binary system at coexistence

The wetting theory for a binary system was first developed by J.W.Cahn [76] , here we follow the arguments and the notation of a review on wetting published D.Bonn and D.Ross [77]. We first briefly remind Cahn's approach. We consider two coexisting phases ϕ_A and ϕ_B in contact with a one dimension-wall, such as a water droplet and its vapour in contact with a substrate (fig 1.40). We assume that the phase ϕ_A has some chemical affinity with the substrate that leads to spreading of the phase ϕ_A on the substrate reducing the total energy of the system. At the same time, spreading increases the interface between the two phases ϕ_A and ϕ_B and costs a surplus of energy for the system. The droplet can either completely wet the substrate if the gain of the energy of wetting is higher that the loss of the energy of interface or partially wet in the opposite case.

In order to model the binary system (liquid and vapour), we use an energy density functional that measures the thermodynamic potential V(ϕ) at each point of the profile as well as the penalty for concentration profile distortions by square gradient terms. V(ϕ) is the free energy of the binary system as a double well function. Surface field contributions E_S account for the specific interactions between the liquid and the substrate ($z = 0$ is the position of the wall):

$$E_S(\phi_S) + \int_0^\infty \left[V(\phi) + \frac{\alpha}{2}\left(\frac{\mathrm{d}\phi(z)}{\mathrm{d}z}\right)^2 \right] \mathrm{d}z \tag{1.4}$$

The surface field energy represents both the wetting interaction between the phase ϕ_A and the substrate (lowing the total energy) and the interaction between the two phases ϕ_A and ϕ_B (increasing the total energy) denoted by: $E_S = h\phi_S^2 - \gamma\phi_S$.

We minimize this functional (AnnexB) of energy with respect to ϕ and ϕ_s and obtain the associated Euler-Lagrange differential equations with corresponding boundary conditions ($\alpha = 1$):

$$\frac{\mathrm{d}V}{\mathrm{d}\phi} = \alpha \frac{\mathrm{d}^2\phi}{\mathrm{d}z^2}$$

$$\frac{\mathrm{d}\phi_S}{\mathrm{d}z} = 2h\phi_S - \gamma \tag{1.5}$$

By multiplying the first equation by $\mathrm{d}\phi/\mathrm{d}z$ one gets:

$$V = \frac{1}{2}(\frac{\mathrm{d}\phi}{\mathrm{d}z})^2 \tag{1.6}$$

Finally we have:

$$\frac{\mathrm{d}\phi}{\mathrm{d}z} = \pm\sqrt{2V}$$

$$\frac{\mathrm{d}\phi_S}{\mathrm{d}z} = 2h\phi_S - \gamma \tag{1.7}$$

We assume that $\phi_A > \phi_B$ and then we choose the solution $\mathrm{d}\phi/\mathrm{d}z = -\sqrt{2V}$ because $\phi(z)$ decreases from $\phi(z = 0)$ to $\phi(z = \infty) = \phi_B$. We now recall the Cahn method [77] for determining the solutions for the profile and its thermodynamic stability.

For that, we plotted the two equations(1.7) on fig(1.42a) on the axis $(\phi, -\mathrm{d}\phi/\mathrm{d}z)$. We can observe three solutions ϕ_1, ϕ_2 and ϕ_3 which correspond to the intersections between the two curves. Cahn proved that the thermodynamic stability of the solutions ϕ_1, and ϕ_3 is determined by the ratio of the area **B** to the area **C**; the solution ϕ_2 being always unstable . If the ratio is greater than 1, the solution ϕ_1 is more stable (partial wetting) than the solution ϕ_3. In the opposite case, when the ratio is shorter than 1, the solution ϕ_3 (complete wetting) is more stable than ϕ_1.

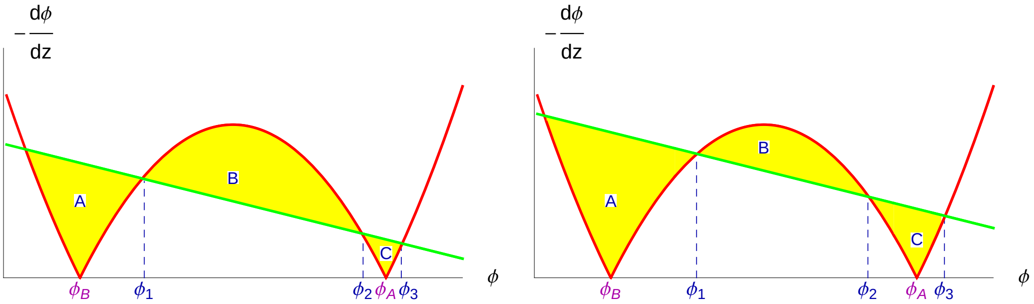

(a) $T < T_W$ (b) $T \approx T_W$

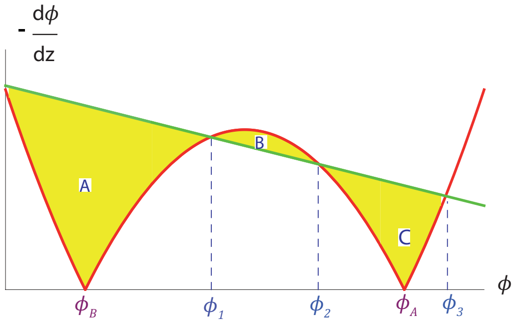

(c) $T > T_W$

Figure 1.42 – *Cahn Diagrams.*

We also show on the diagrams(1.42) how those area ratios as modified as the temperature changes, due to the modification of the free energy V. For a temperature below the wetting temperature (a), the system has a partial wetting and the solution ϕ_1 is a decreasing exponential function without any swelling of the ϕ_A phase near the wall; on the other side for a temperature above the wetting temperature (c), the system has a complete wetting with a macroscopic swelling of the ϕ_A phase near the wall which is characterised by a swelling length ξ. We plotted on the figure (1.43) the two profiles ϕ_1 and ϕ_3 which are respectively partial wetting and complete wetting solutions for which one can see the swelling of the phase ϕ_A.

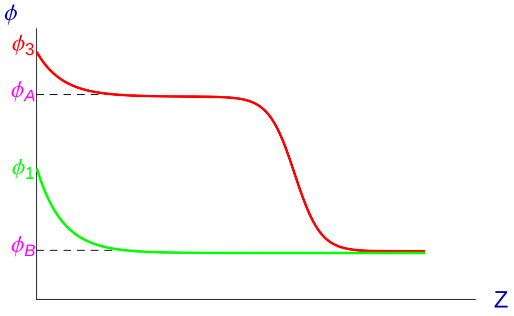

Figure 1.43 – *Partial wetting in green and complete wetting in red.*

Finally, we show on figure(1.44) the binodal coexistence curve of a binary mixture and the transition wetting temperature. Below this temperature the system displays partial wetting while above the system undergoes a wetting transition which leads to a complete wetting.

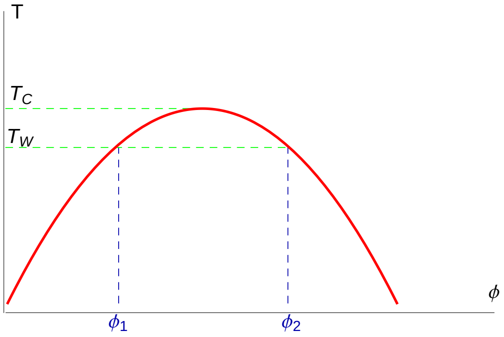

Figure 1.44 – *Binary phase diagram with the wetting transition temperature.*

1.6.3 Wetting at off-coexistence

In this section we study the effect of exposing an off-coexistence binary mixture to the contact with an interface. The mixture composition is represented by a point **A** which is at a short distance from the coexistence line at a temperature above the wetting transition temperature as showed in figure (1.45).
We plotted the energy profile on the figure (1.46) for this off-coexistence system in which we can observe that the point **A** is a minimum of the curve (stable phase) but

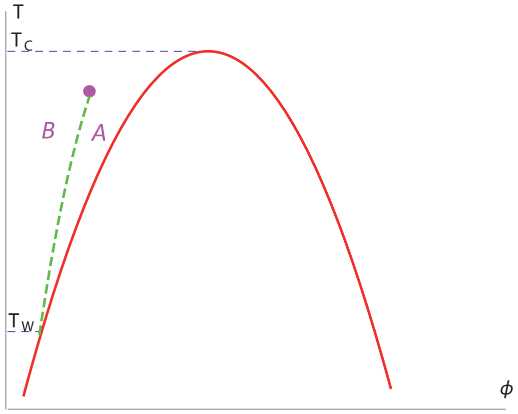

Figure 1.45 – *Binary phase diagram with the pre-wetting horn.* ***A*** *is a point in the stable phase inside the horn which gives pre-wetting in off-coexistence.* ***B*** *is a point in the stable phase outside the horn which doesn't give pre-wetting.*

the other unstable minimum **C** is located at a higher value, because it is no longer a coexistence point; the profile keep its double well topology.

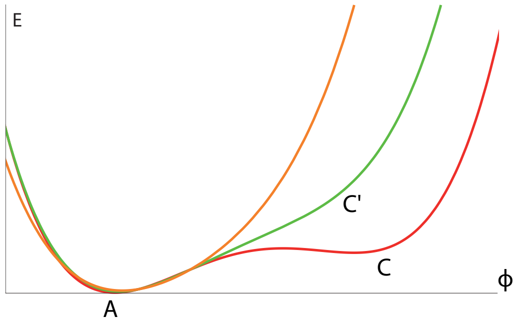

Figure 1.46 – *Energy profile for an off-coexistence system; in red the profil for* ***A*** *near from the coexistence line; in green the profil for* ***A*** *far from the coexistence line; in orange disappearing from the second well.*

It can be shown that as **C** goes up (and becomes **C'**) as high as **A** is distant from the coexistence line. When the point **A** exceeds a certain distant from the coexistence line, the point **C** disappears and the profil is no longer a two wells profil. Henceforth we have choosen a point **A** in a such manner that the energy profile conserves two wells, in order to have a binary system. In the case that the point **A** is not so far from the coexistence line and keeps a double wells energy profil, the system could patially or completely wet somewhere near the **C** point under the same conditions described in the previous section with the Cahn diagram represented in figure(1.47). This wetting is called pre-wetting, because the off-coexistence nature of the system and the green dashed line in the figure(1.45) called pre-wetting horn fixes the pre-wetting limit.

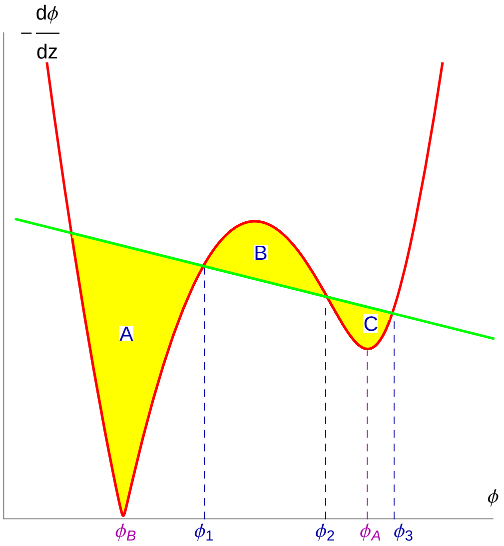

Figure 1.47 − *Cahn diagram for a off-coexistence binary system.*

Chapter 2

Thermodynamic model

2.1 Presentation

In the Introduction, we reviewed the different statistical and thermodynamical approaches used in previous works, from the early 1970s till very recently, to determine the behavior of mixtures of phospholipids with cholesterol. In this chapter, we present a theoretical model based on a mean field treatment of an Ising-like model with an internal order parameter. Our purpose is to build a simple and predictive model starting from the thermodynamic data of each species.

First we build the model for the lipid/lipid and lipid/cholesterol binaries, by introducing an order parameter relative to the specific phospholipid tail ordering in the liquid and gel phases, with an additional interaction between this order parameter and cholesterol. Secondly we present the results obtained for binary mixtures such as the phase diagram, the heat capacity curve and a comparison with experimental results. Finally we extend this study to ternary mixtures of saturated and unsaturated lipids and cholesterol, leading to a Gibbs diagram at a fixed temperature as well as its temperature evolution, in the case of a mixture DOPC/DPPC/Cholesterol.

2.2 Theory of regular solutions

The theory of regular solutions describes mixtures by considering two terms, one for the ideal entropy of mixing contribution, the other for a quadratic interaction term between inequivalent species.

The mixing component of the free-energy $\mathcal{G}_{reg}(x)$ of a binary mixture is:

$$\beta \frac{G_{reg}}{N}(x) = g(x) = x\ln(x) + (1-x)\ln(1-x) + \chi x(1-x) \tag{2.1}$$

with x the molar fraction, N the total number of molecules, $\beta = 1/kT$ and χ the interaction parameter, which traduces the differences of shape and chemical affinity between the two species.

This expression works well for mixtures composed of similar components, which can be mutually substituted for without changing too much their statistical molecular arrangements. The main feature of this approach is the existence of a critical value $\chi = 2$ for the interaction parameter, above which the binary mixture undergoes a phase separation known as spinodal decomposition. This arises because the function $g(x)$ ceases to be a globally convex function of x, as it is clear from its second derivative $g''(x) = 2\chi - 1/[x(1-x)]$.

Flory and Huggins realized that the theory of regular solutions was not describing satisfactorily a class of mixtures called polymer melts. These systems are characterized by macromolecules with sometimes very dissimilar molecular masses, and a strong entropic contribution of their internal conformational degrees of freedom [78]. They proposed a new expression for these melts, originally derived from a mean-field lattice model of the polymer chains. The results can be expressed in terms of the volume fraction ϕ.

$$\beta \frac{G_{FH}(\phi)}{N} = \frac{\phi}{a}\ln(\phi) + \frac{(1-\phi)}{b}\ln(1-\phi) + \chi\phi(1-\phi) \tag{2.2}$$

with a and b the dimensionless molecular masses of each component. In the next chapter, we will make use this model in an attempt to account for the variation in area per molecule at the transition.

The theory of regular solutions cannot account for differences related to the internal order of the lipid chains. As the driving force behind lipid lateral separations comes primarily from these effects, the only way to describe binary lipid mixtures would require an *ad-hoc* behavior of χ and would not be predictive. For this reason we need something different for incorporating the order parameter into the picture. Residual interactions between different species, however, will be accounted for by quadratic terms as in eq. (2.2).

2.3 Mean field model for lipid/lipid interaction

This section introduces the Doniach order parameter m.

We assume that each phospholipid tail can adopt two states, called gel in the ordered, low temperature state and liquid in the disordered, high temperature state. The two phospholipid species, labelled with an index $r = 1, 2$, are characterized by their gel/liquid main transition temperature T_{M_r}, and their entropy jump at the transition ΔS_r, in the pure component limit. The variation ΔS_r is linked to the enthalpy change ΔH_r by $\Delta H_r = T_{M_r} \Delta S_r$ as usual in first order transitions.

We can expand the free-energy difference between the gel and fluid phases at the vicinity of the main transition temperature. The result reads $G_l - G_g = (\Delta S)_r (T - T_{M_r})$, given that these free-energies are, by definition, equal at the transition temperature. This expansion is consistent with a stable liquid state for $T > T_M$ and a stable gel state for $T < T_M$.

We place all the molecules on a square lattice with N_t sites, and assign to each site i an occupancy variable C_i equal to 1 or 2 depending on the chemical nature of the species occupying the state (Potts variables), and an internal state variable Q_i arbitrarily set to 1 for the liquid state, and to -1 for the gel state (Ising variable). We consider that the area per site in the lattice is equal to a^2, so that the total area of the system is given by $\mathcal{A} = N_t \cdot a^2$. The variable Q_i is similar to the spin variables introduced by Doniach. A spin hamiltonian follows:

$$\beta \mathcal{H} = \sum_i \Big[- h^{(1)} \delta_{c_i,1} Q_i - h^{(2)} \delta_{c_i,2} Q_i \Big] - \sum_{(i,j)} J Q_i Q_j \tag{2.3}$$

$h^{(r)}$ is a dimensionless number vanishing linearly with temperature near the melting transition T_{M_r} of species r. It acts like a "switch", favoring the liquid phase $Q_i > 0$ for $T > T_{M_r}$, and the gel phase $Q_i < 0$ for $T < T_{M_r}$. Its expression reads:

$$h^{(r)} = \frac{(\Delta S)_r}{k} \frac{T - T_{M_r}}{2 T_{M_r}}, \tag{2.4}$$

with k the Boltzmann constant. Within the Ising model analogy, $h^{(r)}$ is the magnetic induction. J is an interaction parameter which tend to propagate spatially the internal tail order, *i.e.* the ferromagnetic coupling.

A mean-field expression associated with the above hamiltonian can be derived by rewriting the statistical variables as a sum of a non-fluctuating and a fluctuating part: $Q_i = m + \delta Q_i$ and $\delta_{C_i,r} = \phi_r + \delta \phi_{i,r}$, $r = 1, 2$. Denoting with brackets $\langle \cdot \rangle$ the statistical average over Q_i, C_i, one has by construction $m = \langle Q_i \rangle$ the order parameter and $\phi_r = \langle \delta_{C_i,r} \rangle$ the surface fraction. As $\delta_{C_i,1} + \delta_{C_i,2} = 1$, the relation $\phi_1 + \phi_2 = 1$ holds automatically.

The mean-field hamiltonian is obtained by neglecting the quadratic fluctuation terms $\delta Q_i \delta\phi_{r,i}$ in eq. (2.3), leading to

$$\beta\mathcal{H}_{MF} = N_t \cdot a^2 \left[h^{(1)}\phi_1 m + h^{(2)}\phi_2 m + \frac{zJm^2}{2} \right] + \sum_i \left[-h^{(1)}\phi_1 - h^{(2)}\phi_2 - zJm \right] \delta Q_i$$
$$+ \sum_i \left[-h^{(1)} m \delta_{C_i,1} - h^{(2)} m \delta_{C_i,2} \right] \tag{2.5}$$

Here z is the coordination number of the lattice (number of neighbors of a given site), *i.e.* $z = 4$ for a plane square lattice. The partition sum over the statistical variables $\delta_{C_i,r}$, Q_i can be carried out exactly. The free-energy can be expressed a sum of the averaged hamiltonian, expressed in terms of m and ϕ_i, and an entropic contribution $-TS$.

The averaged mean-field hamiltonian reads:

$$\beta\langle\mathcal{H}_{MF}\rangle = -N_t \cdot \left[h^{(1)}\phi_1 m + h^{(2)}(1-\phi_1)m + 2Jm^2 \right] \tag{2.6}$$

where N_t is the total number of sites. The canonical entropy S is given by a sum over all microstates probabilities p_u.

$$S = -k \sum_u p_u \ln(p_u) \tag{2.7}$$

In the mean field theory, one consider each spin with its own probability. One has $Q_i = 1$ with probability $(1+m)/2$, $Q_i = -1$ with probability $(1-m)/2$, $\delta_{C_i,1} = 1$ with probability ϕ_1 and $\delta_{C_i,1} = 0$ with probability $1-\phi_1$. Therefore,

$$-TS = N_t \cdot kT \Bigg[\phi_1 \ln(\phi_1) + (1-\phi_1)\ln(1-\phi_1)$$
$$+ \left(\frac{1+m}{2}\right) \ln\left(\frac{1+m}{2}\right) + \left(\frac{1-m}{2}\right) \ln\left(\frac{1-m}{2}\right) \Bigg] \tag{2.8}$$

Adding both terms, one obtains the free-energy

$$\beta G = \beta\langle\mathcal{H}_{MF}\rangle + \sum_u p_u \ln(p_u) \tag{2.9}$$

Finally the total free energy of the lipid/lipid mixture $a^2\beta G_{ll}/\mathcal{A}$ is given by:

$$\frac{a^2\beta G_{ll}}{\mathcal{A}} = -h^{(1)}\phi_1 m - h^{(2)}(1-\phi_1)m - 2Jm^2 + \phi_1\ln(\phi_1) + (1-\phi_1)\ln(1-\phi_1)$$
$$+ \left(\frac{1+m}{2}\right) \ln\left(\frac{1+m}{2}\right) + \left(\frac{1-m}{2}\right) \ln\left(\frac{1-m}{2}\right) \tag{2.10}$$

with $\mathcal{A}/a^2 = N_t$, a^2 the surface area per molecule.

It may be noted that our lipid/lipid free energy term is closed from a version of the Blume-Emery-Griffiths model (1970's) which was developped by Lajzerowicz et al. [79].

In the following we note: $\mathcal{G}_{ll}(T,\phi_1,m) = \beta a^2 G_{ll}/\mathcal{A}$, the free energy density per unit area. We observe that all the references to the square lattice have been removed, and that expression (2.10) is meaningful in terms of continuous, off-lattice description of the system.

We first consider binary mixtures and set $\phi_1 = \phi$ to simplify the notation. The order parameter m is not directly controllable. As the internal state is correlated with various structural properties (membrane thickness, area per lipid), the order parameter m is indirectly coupled to external fields, such as the membrane tension or the isotropic pressure. Provided that these external fields remain low, one can consider that m is unconstrained. If we integrate the Boltzmann distribution over all the values of m, one finds that, in the thermodynamic limit, the integral is dominated by a saddle-point value m^*, minimum of $G_{ll}(T,\phi,m)$ with respect to m.

$$\int_{m=-1}^{m=1} e^{-\beta G_{ll}(T,\phi,m)}\,\mathrm{d}m \simeq e^{-\beta G_{ll}(T,\phi,m^*)} \tag{2.11}$$

The value m^* is determined by:

$$\frac{\partial \mathcal{G}_{ll}}{\partial m} = 0 = -h^{(1)}\phi - h^{(2)}(1-\phi) - 4Jm^* + \frac{1}{2}\ln\left(\frac{1+m^*}{1-m^*}\right) \tag{2.12}$$

It results that the total free-energy depends on the temperature T and the surface fraction ϕ and we call $g_{ll}(T,\phi)$ this free-energy function. The minimum m^*becomes implicitly a function of ϕ, so that the free-energy $\mathcal{G}_{ll}(T,\phi,m)$ reduces to a function of T, ϕ only. g_{ll} corresponds to the projection of the free-energy surface $\mathcal{G}_{ll}(T,\phi,m)$ onto a direction perpendicular to the m axis, as shown on figure (2.1). Depending on the value of J, the shape of $g_{ll}(T,\phi)$ may display a double wells, with cusps resulting in a swallow tail topology as depicted on the yellow curve (2.1). In fact $\phi(m^*)$ is given by equation (2.12) and as a consequence, one must study $\phi(m^*)$ in details to understand the behavior of the system and find the best value of J.

Spinodal stability requires that the free-energy surface $\mathcal{G}(T,\phi,m)$ is locally convex, or in other words, the Hessian, matrix of the second derivatives of the free-energy surface,

$$\mathcal{H}_{\mathcal{G}} = \begin{pmatrix} \dfrac{\partial^2\mathcal{G}}{\partial\phi^2} & \dfrac{\partial^2\mathcal{G}}{\partial\phi\partial m} \\ \\ \dfrac{\partial^2\mathcal{G}}{\partial\phi\partial m} & \dfrac{\partial^2\mathcal{G}}{\partial m^2} \end{pmatrix} \tag{2.13}$$

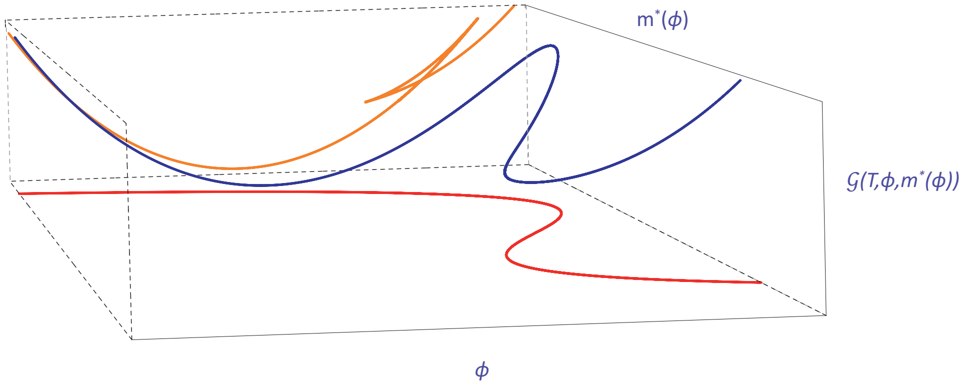

Figure 2.1 – *$\phi(m^*)$ in red, $\mathcal{G}(\phi, m^*(\phi))$ in blue and $g(\phi)$ in yellow. In this calculation we put these following values: $T_{M_1} = 1$, $T_{M_2} = 2$, $T = 1.5$, $(\Delta S)_1/k = (\Delta S)_2/k = 1$, $J = 0.3$*

must be a positive definite matrix. A breakdown of this condition means that the system free-energy can be lowered by splitting the system into two or more components with distinct (ϕ, m) values. As in most regions the criterion is satisfied, it is possible to locate the boundary between stable and unstable region by solving

$$\det(\mathcal{H}_{\mathcal{G}}) = 0. \tag{2.14}$$

This defines the spinodal line.

Setting $\alpha = h^{(1)} - h^{(2)}$, we find that the spinodal line obey the equation (cf appendix A)

$$\phi(1-\phi) = \frac{1 - 4J(1 - {m^*}^2)}{\alpha^2(1 - {m^*}^2)} \tag{2.15}$$

We now discuss the trajectory $\phi(m)$ compared with the location of the thermodynamic stability region (spinodal line) that has been derived above. In the following discussion, we take the following numerical values $T_{M_1} = 1$, $T_{M_2} = 2$, $T = 1.5$, $(\Delta S)_1/k = (\Delta S)_2/k = 1$.

The spinodal region appears when the coupling constant value reaches $J_{cri.} = 0.2422$, and presents a contact point at $m^* = 0$ with $\phi(m^*)$, as showed on figure (2.2). $J_{cri.}$ is obtained by replacing $m^* = 0$ in the equation (2.12). One has $\phi_{cri.} = \frac{h^{(2)}}{h^{(2)} - h^{(1)}}$, which is inserted in the spinodal equation (2.15).

When J reaches a value $J_{cusp} = 0.25$, $\phi(m^*)$ becomes non-monotonous and presents two extrema. When m sweeps the interval $[-1, 1]$, ϕ increases up to the point **A**, decreases down to **B**, and increases again as shown on figure (2.3). The function $m^*(\phi)$ becomes multivalued.

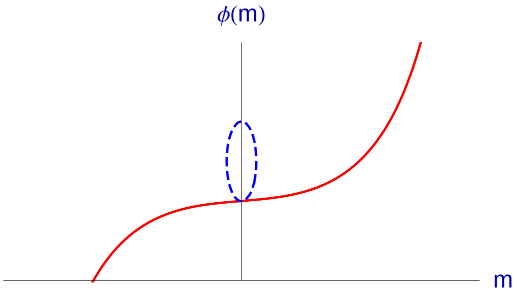

Figure 2.2 – $\phi(m^*)$ *representation in red with the spinodal in blue dashed line for* $J = 0.2422$*. The two curves are in contact at* $m^* = 0$

The equation $\frac{\partial\phi}{\partial m^*} = 0$ reads $J = \frac{1}{4(1-m^{*2})} > 1/4$. Therefore, J must be greater than $J_{cusp} = 1/4$ for the equation to have a solution.

In order to obtain a two wells shape of energy it is necessary that $J > J_{cusp}$ although that all the points inside the spinodal which are between **M** and **N** represent unstable thermodynamic states as **A** and **B** the two extrema. The positions of the extrema relative to the spinodal endpoints are determined by replacing the condition $\frac{\partial\phi(m^*)}{\partial m^*} = 0$ in the Hessian and find it is negative as an unstable state.

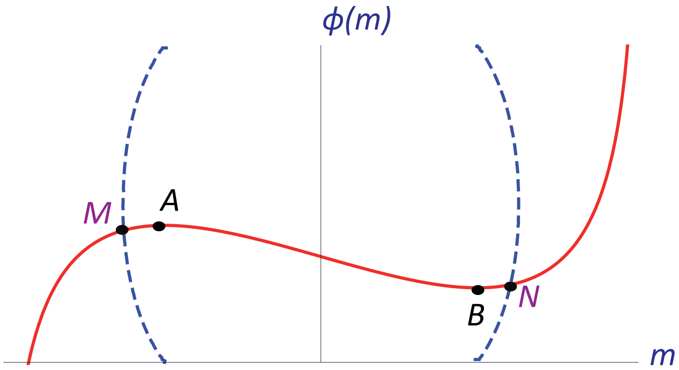

Figure 2.3 – $\phi(m^*)$ *representation in red, with the spinodal in blue dashed line for* $J = 0.25$*.*

We plot the corresponding free-energy for $J = 0.25$ on the figure (2.4) and mark some important points as **A**, **B** the extrema of $\phi(m^*)$, and **M**, **N** the spinodal endpoints. The result is a swallow-tail shape with two intersecting branches which are thermodynamically stable up to **M** for the branch 1 and from **N** for the branch 2.

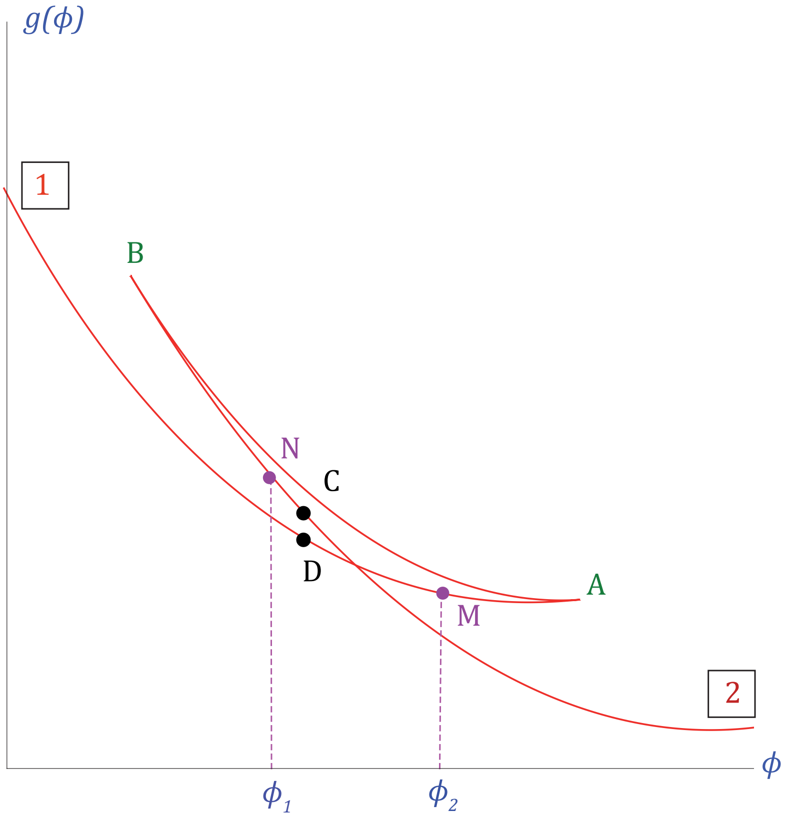

Figure 2.4 – *Representation of $g(\phi)$ for J=0.25.*

We notice for example on this picture that the point **C** is stable with respect to ϕ as the point **D** below, although it has an other value of m which confers it a meta-stable state. From an external point of view, **C** and **D** are not distinguishable, because they share the same value of ϕ but with a different value of the order parameter m. These two states are therefore not identical, one representing a predominantly fluid state, the other a predominantly gel state.

2.4 Determination of $(\Delta S)_r$ for a lipid

The single component $\phi_1 = 1$ free-energy reads:

$$\mathcal{G}_{ll}(T,\phi,m^*) = -h^{(r)}m^* - 2Jm^{*2} + \left(\frac{1+m^*}{2}\right)\ln\left(\frac{1+m^*}{2}\right) + \left(\frac{1-m^*}{2}\right)\ln\left(\frac{1-m^*}{2}\right) \tag{2.16}$$

Thermodynamic data tables, established after DSC measurements, list the melting temperature T_M and the enthalpy jump (ΔH) at the transition. A classic thermodynamic identity relates the Gibbs free-energy G and the enthalpy H:

$$\Delta H = \frac{\partial(\beta \Delta G)}{\partial \beta} \tag{2.17}$$

with $\beta = 1/(kT)$. Using the expression (2.16), we obtain:

$$-\frac{\partial h^{(r)}}{\partial \beta}\Delta m = -\frac{\partial h^{(r)}}{\partial T}\frac{\partial T}{\partial \beta}\Delta m = \frac{T_{M_r}(\Delta S)_r}{2}\Delta m = (\Delta H)_r \tag{2.18}$$

The optimal values m^* have the same magnitude but opposed signs. At the coexistence temperature $h = 0$, the discontinuity in m is simply $\Delta m = 2m^*$. From the relation (2.12) reduced to one component, one finds that m^* obey

$$4Jm^* = \frac{1}{2}\ln\left(\frac{1+m^*}{1-m^*}\right), \tag{2.19}$$

a transcendental equation which can be solved numerically, as represented on figure (2.5).

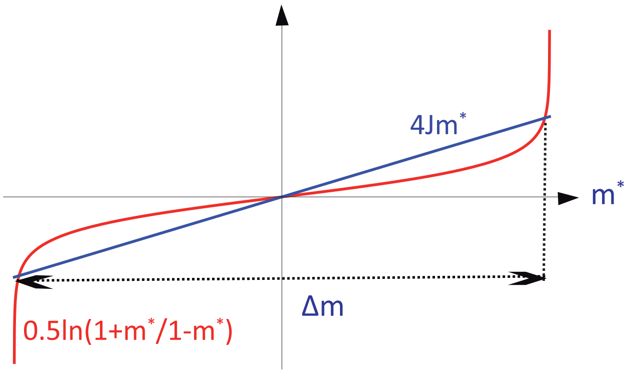

Figure 2.5 — *Geometric representation of the transcendent equation* 2.19.

In fact we find that Δm is generally of the order of 1.8 and close to 2. In the following we simply write:

$$(\Delta H)_r \approx T_{M_r}(\Delta S)_r \tag{2.20}$$

2.5 Binary phospholipid phase diagram

2.5.1 Maxwell construction

If the two lipids are similar, the molar fractions x_A, x_B and the surface fractions ϕ_A, ϕ_B are identical. The molar fractions are $x_A = N_A/(N_A + N_B)$ and $x_B = N_B/(N_A + N_B)$, and $\phi_A = x_A$, $\phi_B = x_B$. The reason for using surface fractions here is that it is consistent with the Flory-Huggins expression. When the area per lipid differs between species, one looses the equivalence between x and ϕ.

We so far obtained an expression for the free-energy of homogeneous binary systems. Looking at the free-energy curve shown on figure (2.7), one realizes that at temperature low enough, the curve looses its convexity. The total free-energy can therefore be lowered by separating the system into two coexisting phases with different composition , see figure (2.6). The Maxwell constructions allows to find out the optimal composition of the two coexisting phases which appear in the instability region, as illustrated on figure (2.7).

Let $N_{A,1}$, $N_{B,1}$, $N_{A,2}$, $N_{B,2}$ the number of A and B molecules respectively in phase 1 and phase 2, and the associated surface fractions $\phi_{A,1} = N_{A,1}/(N_{A,1} + N_{B,1})$, $\phi_{A,2} = N_{A,2}/(N_{A,2} + N_{B,2})$. Let η be the ratio between the surface occupied by phase 1 and the total surface. Mass and area conservation of A (and B) molecules implies $\phi_A = \eta\phi_{A,1} + (1 - \eta)\phi_{A,2}$. On the other hand, the free-energy of the biphasic system per unit of area is

$$\mathcal{G}_{tot.} = \mathcal{G}(\phi_{A_1})\eta + \mathcal{G}(\phi_{A_2})(1 - \eta) \tag{2.21}$$

provided one neglects all interfacial contributions. When η increases from 0 to 1, the free-energy $\mathcal{G}$ appearing in eq. (2.21) spans the straight segment lying below the curve of figure (2.7), thus lowering the free-energy compared with the one of a monophasic system with similar composition. The Maxwell construction consists in finding the unique double tangent to the curve, touching the latter on points of abscissa $\phi_{A,1}$ and $\phi_{A,2}$. This geometrical construction determines the composition of the two coexisting phases, as well as the fraction η of each one of them (lever rule).

This geometrical construction leads to the following set of analytical equations,

$$\frac{\partial \mathcal{G}(\phi_{A_1})}{\partial \phi_{A_1}} = \frac{\mathcal{G}(\phi_{A_2}) - \mathcal{G}(\phi_{A_1})}{\phi_{A_2} - \phi_{A_1}}$$

$$\frac{\partial \mathcal{G}(\phi_{A_2})}{\partial \phi_{A_2}} = \frac{\mathcal{G}(\phi_{A_2}) - \mathcal{G}(\phi_{A_1})}{\phi_{A_2} - \phi_{A_1}} \tag{2.22}$$

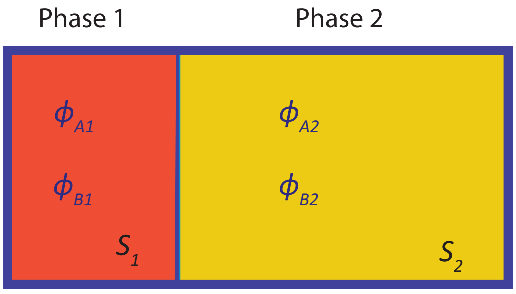

Figure 2.6 – *Phase separation of a binary mixture.*

which must be solved in terms of ϕ_{A_1} and ϕ_{A_2}. We observe that the equations (2.22) correspond to a double equality, first between the slopes at ϕ_{A_1} and ϕ_{A_2}, and second the equality between the common slope and the slope of the straight line joining ϕ_{A_1} and ϕ_{A_2} (figure2.7).

These equations can be viewed as the equality of chemical potentials $\mu_i = \partial\mathcal{G}(\phi_{A_i})\partial\phi_{A_i}$ (up to a constant) and the equality of the osmotic pressure $p = \mu_i\phi_{A_i} - \mathcal{G}(\phi_{A_i})$ in each phase i.

2.5.2 Binary phase diagram of DOPC/DPPC

In the context of our model, we calculate the chemical potential and the osmotic pressure and obtain:

$$\mu = -h^{(1)}m^* + h^{(2)}m^* + \ln(\phi) - \ln(1-\phi) \tag{2.23}$$

$$p = h^{(2)}m^* + 2Jm^{*2} - \left(\frac{1+m^*}{2}\right)\ln\left(\frac{1+m^*}{2}\right) - \left(\frac{1-m^*}{2}\right)\ln\left(\frac{1-m^*}{2}\right) - \ln(1-\phi) \tag{2.24}$$

We solve numerically the system of equations (2.22) for a given value of the temperature T, and plot the binary diagram for a mixture of DOPC ($T_{DOPC} = -21$°C, $\Delta H = 7700$kcal/mol [5]) and DPPC-d62 ($T_{DPPC} = 37.8$°C, $\Delta H = 8700$kcal/mol [80]), with a value of $J = 0.35$ which was chosen in a way to offer the best agreement with the experimental data. We plot on the same figure (2.8) our theoretical diagram and the experimental data points (green pluses) published by Schmidt and Davis [24].

The plot agrees fairly with the experimental data, and the deviations seen on the gel phase coexistence line close to the upper transition temperature could in principle be improved by accounting for the area differences between the two lipids. An attempt to do this in this direction will be attempted in next section.

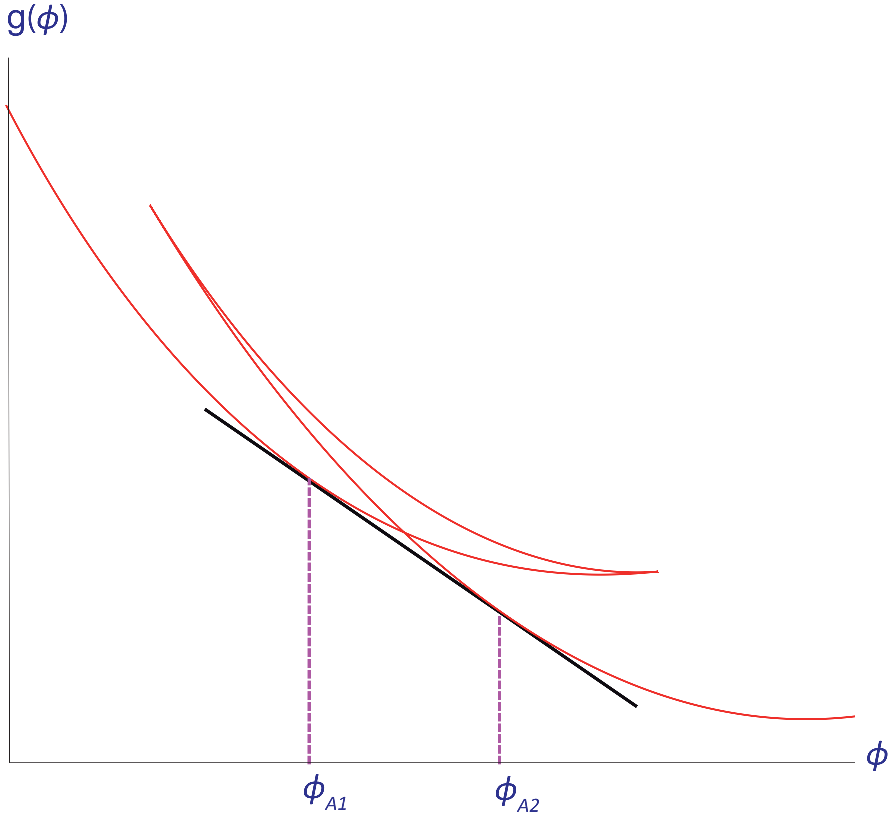

Figure 2.7 – *Maxwell double tangents construction (in black the double tangent),* ϕ_A *and* ϕ_B *the phases in equilibrium.*

We plot the same DOPC/DPPC binary phase diagram on figure (2.9), superimposing a color chart map of the internal order parameter m values. One notices that the order parameter switches bluntly from $m \simeq -1$ (gel state in red) to $m \simeq 1$ (liquid state in blue), and there are no intermediate values associated with a smooth transition. The abruptness of the transition is controlled by the value of the coupling parameter J.

2.6 Determination of the heat capacity

In this section, we determine the heat capacity as a function of temperature within the context of our model, and compare our results to published calorimetric results. The heat capacity is defined as the first derivative of the enthalpy with respect to the temperature $C_P = dH/dT$ with $H = d\beta G/d\beta$. In order to calculate the heat capacity, we have to consider a fixed value of ϕ_0 the surface fraction of DOPC, to

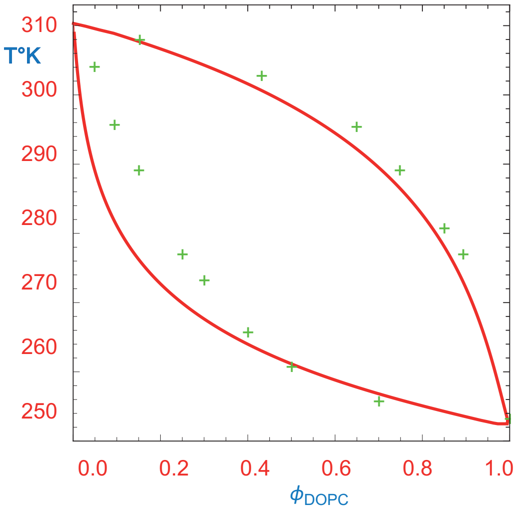

Figure 2.8 — *Calculated DOPC/DPPC phase diagram (J=0.35) in red and experimental data in green pluses. Comparison between our theoretical prediction (full line) and data (pluses) from Schmidt and Davis [24] on the DPPC-DOPC coexistence diagram as determined from NMR.*

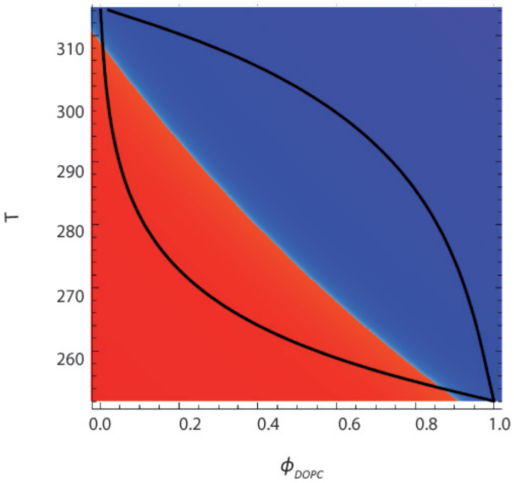

Figure 2.9 — *Calculated DOPC/DPPC phase diagram ($J = 0.35$) with the superimposition of m, (blue $m = 1$, liquid state and red $m = -1$ gel state).*

evaluate the enthalpy first and finally the heat capacity.

There are two categories of points, labeled M and N on figure (2.10). M corresponds to an homogeneous phase and N to a biphasic ϕ_1 and ϕ_2 point. For the biphasic mixture (point N) the enthalpy is:

$$H_{ll}(T,\phi_0) = \eta H_{ll}(T,\phi_1,m) + (1-\eta)H_{ll}(T,\phi_2,m') \tag{2.25}$$

with $\eta = (\phi_2 - \phi_0)/(\phi_2 - \phi_1)$ the fraction of the molecules in phase 1. The heat capacity reads:

$$C_p(T,\phi_0) = \frac{d\eta}{dT}\left[H(T,\phi_1,m) - H(T,\phi_2,m')\right] + \eta\left[\frac{\partial H(T,\phi_1,m)}{\partial T} + \frac{\partial H(T,\phi_1,m)}{\partial \phi_1}\cdot\frac{\partial \phi_1}{\partial T}\right]$$
$$+(1-\eta)\left[\frac{\partial H(T,\phi_2,m')}{\partial T} + \frac{\partial H(T,\phi_2,m')}{\partial \phi_2}\cdot\frac{\partial \phi_2}{\partial T}\right] \tag{2.26}$$

For a point of homogeneous composition M, the heat capacity is given by the equation (2.26) with $\eta = 1$. Details of the derivation of the expression of the heat capacity are provided in the appendix (D).

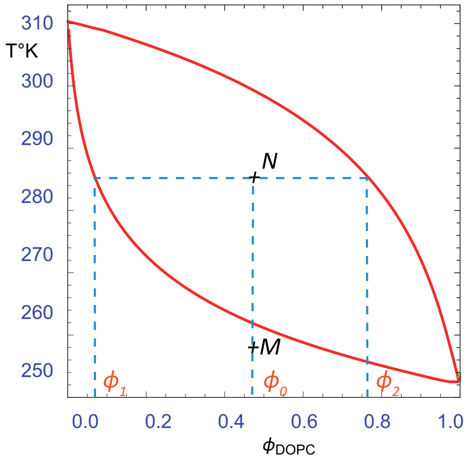

Figure 2.10 – *Calculated DOPC/DPPC phase diagram with the labeled points M for the homogeneous phase, and N for the biphasic region.*

We compute the heat capacity for different ratio of DOPC/DPPC (figure 2.11) and compare it to the measurement by Schrader et al. We observe that the results are in good agreement with the experiment datas.

Various hypothesis can be formulated to explain the discrepancy between our theoretical and the experimental data. First the experimental apparatus induces a widening of the curve, due to the kinetics of the thermal response and to the structural polydispersity of the system, causing a rounding of the peaks.

It is important to note that the height of the calculated peaks is systematically larger than the experimental ones. In 2001, Ivanova et al. [82] made Monte-Carlo simulations on the thermodynamics of liposomes, took into account the strong curvature of these small systems and especially the area difference between the inner

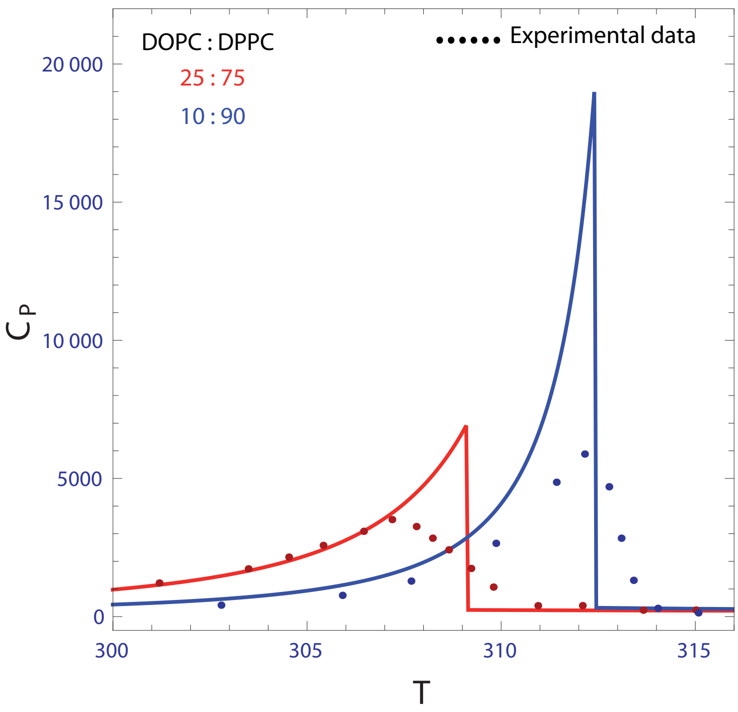

Figure 2.11 – *Calculated heat capacity curves for three DOPC/DPPC binary mixtures. The DOPC/DPPC proportions are indicated in the table (25/75 in red, 10/90 in blue). The values shown on the dotted line indicate the experimental data found in [81].* C_P *is given in* $kJ/mol.K$

and the outer leaflets. They proved that the heat capacity curves show a significant dependence with curvature, reaching a factor of three (figure2.12) for vesicles of 100 nm, the size of the ones that were used in [81]. This effect could very well explain the difference between our calculation at zero curvature, and the measures done with liposomes.

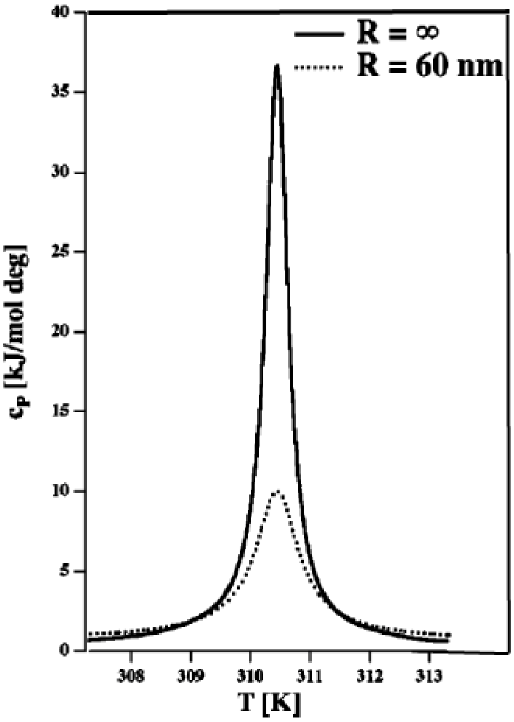

Figure 2.12 – *Heat capacity profiles for bilayers with two different mean curvatures, c=0 (solid lines) and 1/c=r=60 nm (dotted lines)[82].*

2.7 Binary cholesterol-phospholipid phase diagram

2.7.1 The specific cholesterol entropy: the umbrella effect

The specific interaction between cholesterol and lipid is dealt with separately because experiments and simulations either suggest that cholesterol may form transient bound complexes with phospholipid moieties surrounding them [25, 26]. The presence of such complexes prevents cholesterol molecules from occupying too many neighboring positions, thus giving the semblance of a large excluded volume. In order to model this *umbrella effect* in the study of ternary mixtures below, we consider a mixture composed of two lipids and cholesterol and derive a specific term for a entropy of mixing term.

In establishing the specific entropy of cholesterol $\mathcal{G}_{cl_e}(T, \phi_1, \phi_2, m)$, we assume that each of the N_c cholesterol molecules is surrounded by δ lattice sites (N_t the total sites in the lattice) which cannot be occupied by other cholesterol molecules (excluded cholesterol on figure 2.13).

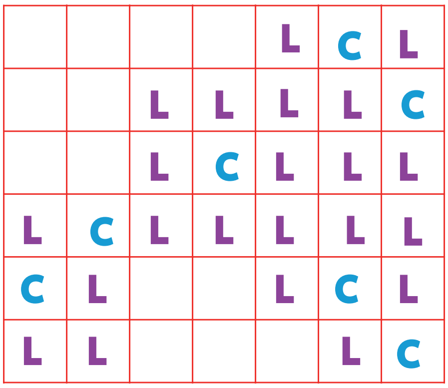

				L	C	L
		L	L	L	L	C
		L	C	L	L	L
L	C	L	L	L	L	L
C	L			L	C	L
L	L				L	C

Figure 2.13 – *Schematic representation from a lattice with cholesterol (C) and lipid (L) which are disposed in a such manner that cholesterol cannot be surrounded of more than one other cholesterol.*

We estimate the number of possible configurations with cholesterol molecules to be:

$$\begin{aligned}\Omega^{(2)} &= \frac{N_t(N_t-\delta)(N_t-2\delta)\ldots(N_t-N_c\delta+\delta)}{N_c!}\\ &= \frac{\delta^{N_c}(N_t/\delta)!}{N_c!(N_t/\delta-N_c)!}\end{aligned} \tag{2.27}$$

where correlations between the mutual cholesterol exclusion domains have been disregarded, as in the usual Flory-Huggins counting procedure. If two or more phospholipids components are present, one must account for a residual combinatorial contribution corresponding to the $N_t - N_c$ sites that are left available to these molecules. We obtain:

$$\Omega^{(3)} = \Omega^{(2)} \times \frac{(N_t-N_c)!}{N_1!N_2!} \tag{2.28}$$

and finally the specific entropy of cholesterol:

$$\begin{aligned}\mathcal{G}_{cl_e}(T,\phi_1,\phi_2) = -\ln(\Omega^{(3)}) &= \phi_1\ln(\phi_1)+\phi_2\ln(\phi_2)+\phi_C\ln(\phi_C)\\ &-(\phi_1+\phi_2)\log(\phi_1+\phi_2)+(\delta^{-1}-\phi_C)\log(1-\delta\phi_C)\end{aligned} \tag{2.29}$$

with $\phi_1 = N_1/N_t$, $\phi_2 = N_2/N_t$, $\phi_c = N_c/N_t$ and $\phi_1+\phi_2+\phi_c = 1$.

This non-ideal entropy term accounts for both the mixing properties and the cholesterol-cholesterol excluded surface, with the same level of accuracy as a Van der Waals description of interacting fluid mixtures. The physical content of this expression is that cholesterol molecules appear "bigger" to other cholesterol molecules than they do to phospholipid molecules. The mixture is non additive with respect to mutual exclusion distances. Expression (2.29) reduces to ideal mixing when $\delta \to 1$, and resembles the entropy of Komura *et al.* for binary systems and $\delta = 2$ [66]. It accounts for both the mixing term and the excluded volume between cholesterol molecules, consistent with the presence of cholesterol complexes. It finally sets a maximal value $\phi_C \leq 1/\delta$ to the mixture content in cholesterol.

In the case of the binary lipid (ϕ_2=0)-cholesterol (ϕ_C) mixture, $\mathcal{G}_{cl_e}(T, \phi_C)$ becomes:

$$\mathcal{G}_{cl_e}(T, \phi_C) = = \phi_C \ln(\phi_C) + (\delta^{-1} - \phi_C) \log(1 - \delta\phi_C) \tag{2.30}$$

The value of δ is bound by the maximum amount of cholesterol that a membrane can hold, estimated here to $\phi_C \simeq 0.45$, or equivalently $\delta = 1/\phi_C = 2.2$ [28].

2.7.2 Interaction lipid-cholesterol

Cholesterol-phospholipid interactions are further accounted for with a specific interaction term

$$\mathcal{G}_{cl_i}(T, \phi_C, m) = -\xi m(1 - \phi_C)\phi_C \tag{2.31}$$

Eq. (2.31) comprises a m-dependent contribution, proportional to ξ, which marks the preference of cholesterol for either the $m = 1$ liquid order, or the $m = -1$ gel order, according to the sign of ξ.

2.7.3 DPPC cholesterol diagram

The free energy of the cholesterol-lipid mixture $\mathcal{G}_{cl}$ corresponds to the sum of the specific cholesterol entropy, the lipid-cholesterol interaction and the internal entropy given by:

$$\begin{aligned}\mathcal{G}_{cl}(T, \phi_C, m) = {} & \phi_C \ln(\phi_C) + (\delta^{-1} - \phi_C) \log(1 - \delta\phi_C) - \xi m(1 - \phi_C)\phi_C \\ & -h^{(1)}(1 - \phi_C)m - 2Jm^2 + \left(\frac{1+m}{2}\right)\ln\left(\frac{1+m}{2}\right) + \left(\frac{1-m}{2}\right)\ln\left(\frac{1-m}{2}\right)\end{aligned} \tag{2.32}$$

We use the same method as in section 2.5.2 to compute the DPPC/chol phase

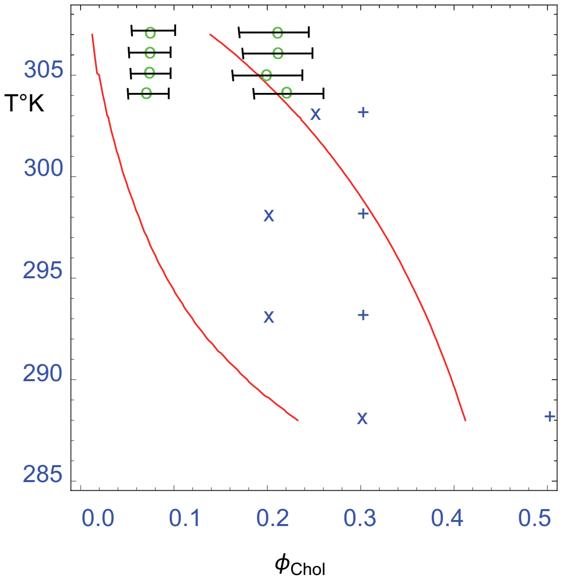

Figure 2.14 — *Comparison between our theoretical prediction (full line) and boundary data (circles, from NMR) from Vist and Davis [60] and (crosses and pluses, from GUVs observation) from Veatch et al. [68]. Pluses indicate a membrane composition for which an homogeneous fluid state has been observed, they constitute an upper bound for the right phase-boundary line. Crosses denote membrane compositions containing a gel phase, and are expected to lie to the right of the upper phase boundary for the gel phase.*

diagram. We chose $\xi = 1.8$ to reproduce well the temperature behavior of the miscibility gaps occurring between the L_β-gel phase and the L_o liquid ordered phase as determined from Giant Unilamellar Vesicles in [83] and from NMR [60] - see fig. (2.14).

The plot on figure (2.14) shows experimental data for phase boundaries of the binary system DPPC-Cholesterol. Data points at and above 304 K were determined by NMR on dense lamellar structures, while data at lower temperatures was collected from the optical observation of Giant Unilamellar Vesicles. We did not find in the literature a comprehensive and consistent determination of the phase diagram boundaries for this binary system. The incomplete data that we plot in figure (2.14) clearly shows that a precise comparison between experiments and theory cannot as yet be attempted. However, many predictions of our theory do correspond to observed experimental properties. First, we do find as in experiments a succession of three regions as the concentration of cholesterol is increased: the first and the last regions corresponding to single phases respectively poor and rich in cholesterol, separated by a phase coexisting region. Also, the theoretical and the experimental widths of the phase coexisting gap are comparable, particularly when one considers the method used to determine the data points obtained from experiments in GUVs. Indeed the only information that we have is that pluses and crosses must be to the right of the actual respective phase boundaries.

2.8 Ternary phase diagram DOPC/DPPC/Cholesterol

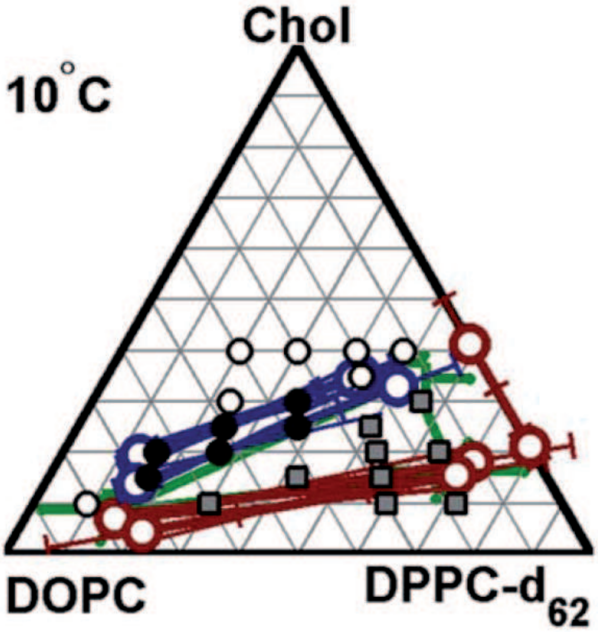

Figure 2.15 – *Gibbs ternary diagram DOPC/DPPC/Cholesterol [68].*

2.8.1 Free energy of the system

Arguably, the most widely studied ternary lipid phase diagram for membranes containing cholesterol is the ternary mixture DOPC/DPPC/Chol -see figure (2.15). DOPC is a double tail molecule with 18 carbons per tail and a *cis*-unsaturated bond on the ninth carbon. It has a low main transition temperature T_1 at −21°C and an associated enthalpy change ΔH_1 evaluated at 7.7 kcal/mol [5]. DPPC has also a phosphatidylcholine head but here the two 16-carbon tails have no unsaturated bonds, leading to a higher transition temperature T_2 at 42°C, and associated enthalpy change $\Delta H_2 = 8.7$ kcal/mol [5].

Equation 2.32 requires to determine three parameters, δ, J, ξ: $\delta = 2.2$ which is bound by the maximum amount of cholesterol that a membrane can hold, $\xi = 1.8$ which quantifies the preference of cholesterol for the liquid disordered phase with respect to the gel phase [6, 61] and $J = 0.35$ as discussed above. For a satisfactory description of the ternary phase diagram our model also needs a repulsive m-independent interaction between cholesterol and the unsaturated component (here DOPC), given by χ. ξ takes in account the tails state of the species whereas χ reflects the chemical nature of the lipids doing differences between saturated and unsaturated molecules.

The free energy of the ternary mixture ($\phi_1 + \phi_2 + \phi_C = 1$) is therefore given by:

$$\begin{aligned}
\mathcal{G}(T,\phi_1,\phi_2,m) &= \mathcal{G}_{llc}(T,\phi_1,\phi_2,m) \\
&= \phi_1 \ln(\phi_1) + \phi_2 \ln(\phi_2) + \phi_C \ln(\phi_C) - (\phi_1+\phi_2)\log(\phi_1+\phi_2) \\
&\quad +(\delta^{-1} - \phi_C)\log(1-\delta\phi_C) - h^{(1)}\phi_1 m - h^{(2)}\phi_2 m - 2Jm^2 \\
&\quad + \left(\frac{1+m}{2}\right)\ln\left(\frac{1+m}{2}\right) + \left(\frac{1-m}{2}\right)\ln\left(\frac{1-m}{2}\right) \\
&\quad -\xi m(\phi_1+\phi_2)\phi_C + \chi\phi_1\phi_C
\end{aligned} \tag{2.33}$$

We end up with four parameters: δ, J, ξ, χ. The parameter χ is free and must be chosen in order to reproduce the phase diagram as well as possible.

2.8.2 Method for the numerical Maxwell construction

We developed an original method for determining the different coexistence regions of ternary mixtures. This method is by no means restricted to our own proposal, and other models could be studied and compared with ours as well. This is why we believe that this method should be exposed in detail here.

In the absence of surface tension, and assuming that changes in internal state occur at constant volume, m fluctuates around its optimal value $m^\star$, with $m = m^\star$ in the thermodynamic limit. Therefore, the free-energy of mixing $g_{\text{mix}}(T,\phi_1,\phi_2)$ is obtained by minimizing $\mathcal{G}(T,\phi_1,\phi_2,m)$ with respect to m at fixed temperature and surface fractions.

$$\begin{aligned} g_{\mathrm{mix}}(T,\phi_1,\phi_2) &= \min_m \left[\mathcal{G}(T,\phi_1,\phi_2,m)\right]\big|_{T,\phi_1,\phi_2} \\ &= \mathcal{G}(T,\phi_1,\phi_2,m^\star(T,\phi_1,\phi_2)). \end{aligned} \tag{2.34}$$

The Gibbs free-energy surface g_{mix} arises from projecting out m from the four-dimensional potential $\mathcal{G}$. Equivalently, g_{mix} can be viewed as the restriction of $\mathcal{G}$ to the submanifold $\partial_m \mathcal{G} = 0$. For $J > J_{cusp}$, the constraint $\partial_m \mathcal{G} = 0$ defines two stable submanifolds, a negative $m_g(T,\phi_1,\phi_2)$ and a positive $m_l(T,\phi_1,\phi_2)$ branch, linked respectively with the gel and liquid phases. At fixed (T,ϕ_1,ϕ_2), only one of the two branches is the stable one, while the other branch remains metastable. Phase coexistence is dictated by the convexity properties of $g_{\mathrm{mix}}(T,\phi_1,\phi_2)$ relative to ϕ_1, ϕ_2. The convex minimization of g_{mix} reveal regions of three kinds. Points of the convex hull in contact with the original surface are stable monophasic regions. Regions lying above triple tangent planes corresponds to triple coexistence. The remaining part of the convex hull correspond to developable patches of surface, wrapped around double tangent lines that connects pairs of points with distinct composition (tie-lines) [84]. It is of higher practical importance to determine the lower convex hull $\tilde{g}_{\mathrm{mix}}$ of the free-energy of mixing, which constitutes the proper generalization of the Maxwell construction for cases where the Gibbs phase rule allows for three or more coexisting phases. We used a public domain routine, *qhull*, to compute a discrete approximation of $\tilde{g}_{\mathrm{mix}}$ [85]. The starting point is a fine mesh discretization of g_{mix} over the relevant domain of composition $\{\phi_1, \phi_2 \geq 0, \phi_1 + \phi_2 \leq 1 - 1/\delta\}$. Then *qhull* computes a triangulated surface approaching $\tilde{g}_{\mathrm{mix}}$ (fig. 2.16). Triple coexistence correspond to facets with all sides much larger than the initial mesh size. Double coexistence is associated with elongated triangles, with a shortest side much smaller than the two longer sides, the latter being oriented parallel with the tie-lines. Finally, small facets of the convex minimization are linked with stable monophasic regions. The projection of the triangulated $\tilde{g}_{\mathrm{mix}}$ surface onto the composition plane provides directly an accurate approximation of the Gibbs phase diagram.

2.8.3 Results

At 10°C a value of $\chi = 6.0$ promotes both a triple coexistence region and a large biphasic domain, with oblique L_o/L_d tie lines of positive slope and a plait point on the left side of the Gibbs triangle, in agreement with experimental findings [23]. A larger value of χ would open there a miscibility gap, unseen for DOPC/Chol, while a smaller value would drastically reduce the biphasic L_o/L_d domain. In our model a continuous path connects the L_o and L_d regions around the critical point, where

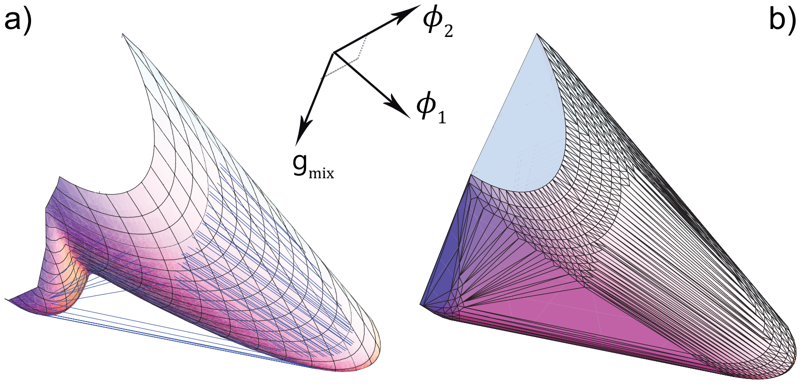

Figure 2.16 – *a) 3D representation of* $\tilde{g}_{\mathrm{mix}}$ *with the tie-lines in blue. b)3D representation of* $\tilde{g}_{\mathrm{mix}}$ *with the computed triangulated surface.*

the order parameter m remains positive. The L_β phase on the lower right corner of the phase diagram is associated with a negative m-value and separated from the rest of the diagram by a discontinuity in m across the coexistence gap (figure2.17).

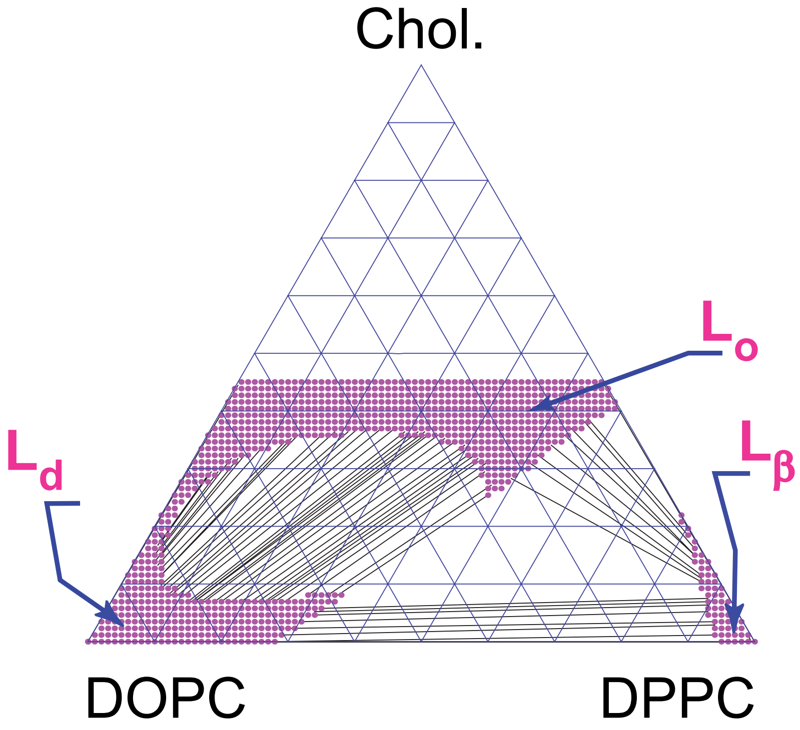

Figure 2.17 – *Computed Gibbs diagram with our model.* $J = 0.35$, $\delta = 2.2$, $\xi = 1.8$, $\chi = 6$.

Chapter 3

Improvement and applications of the model

3.1 Boundaries of the Gibbs triangular phase diagram

The Gibbs diagram obtained in the previous chapter was computed with a discrete triangulation method. Refinements of this discrete solution are necessary to locate precisely the diagram boundaries, the tie-lines, and the possible critical points. These boundaries are found by solving nonlinear systems of coupled equations, to which the discrete approach provides an accurate initial seed. Similar nonlinear equations can be obtained for triple coexistence regions and critical plait points. Details of these calculations are given below.

3.1.1 Derivative of the implicit free-energy function

The potential $g_{\text{mix}}(T, \phi_1, \phi_2)$ defined in equation 2.34 corresponds to a minimization of the order parameter dependent expression $\mathcal{G}(T, \phi_1, \phi_2, m)$. The minimization equation $\partial\mathcal{G} = 0$ may lead to many branches of solution $m_\alpha(\phi_1, \phi_2)$ (theorem of implicit functions). In the case that is considered in this approach, there are only two relevant branches associated respectively with the liquid ($m_l > 0$) and the gel state ($m_g < 0$). The projection step is equivalent to projecting out a shadow of the original surface onto the (ϕ_1, ϕ_2) plane (figure3.1).

Working with an internal order parameter requires an adjustment of the standard equations of thermodynamics describing phase coexistence. We show in the following how these equations can be written in terms of $\mathcal{G}(T,\phi_1,\phi_2,m)$ without having to exhibit explicitly the dependence of m in ϕ_1,ϕ_2. Our procedure is generic and could be applied to all similar approach, such as, for instance the model of Putzel and Schick [71].

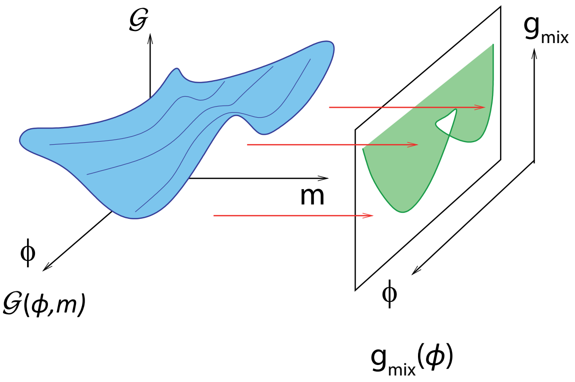

Figure 3.1 – *Projection of the free energy in the* (ϕ_1,ϕ_2) *plane.*

It is convenient to introduce the generalized derivatives

$$\begin{aligned} D_{\phi_1} &= \partial_{\phi_1} + \partial_{\phi_1} m \cdot \partial_m \\ D_{\phi_2} &= \partial_{\phi_2} + \partial_{\phi_2} m \cdot \partial_m \end{aligned} \tag{3.1}$$

where $m(\phi_1,\phi_2)$ is one of the local branch solving $\partial\mathcal{G} = 0$. The generalized derivatives correspond to a differentiation of $\mathcal{G}$ following the local minimum in m. For instance:

$$D_{\phi_1}\mathcal{G} = \partial_{\phi_1} g \text{ and } D_{\phi_2}\mathcal{G} = \partial_{\phi_2} g \tag{3.2}$$

Derivatives of m with respect of ϕ_1 and ϕ_2 follows from a differentiation of the identity

$$\mathrm{d}\partial_m\mathcal{G} = 0 \tag{3.3}$$

from which one gets the two required partial derivatives

$$\begin{aligned} \partial_{\phi_1} m &= -\frac{\partial_{m\phi_1}\mathcal{G}}{\partial_{mm}\mathcal{G}} \\ \partial_{\phi_2} m &= -\frac{\partial_{m\phi_2}\mathcal{G}}{\partial_{mm}\mathcal{G}} \end{aligned} \tag{3.4}$$

It is easy to check that the generalized derivatives commute

$$[D_{\phi_1}, D_{\phi_2}] = 0 \tag{3.5}$$

and it is possible to define generalized partial derivatives of higher order. For instance:

$$D^2_{\phi_1\phi_2} = D_{\phi_1} D_{\phi_2} = D_{\phi_2} D_{\phi_1} = D^2_{\phi_2\phi_1} \tag{3.6}$$

Thanks to the generalized derivatives, one can translate the well-known coexistence conditions originally derived by Gibbs [84] to any thermodynamic function $\mathcal{G}$ depending implicitly on a single explicit scalar order parameter.

3.1.2 Tie-lines and binary coexistence

The Maxwell conditions for two extreme conjugate points $(\phi_1, \phi_2; m)$ and $(\psi_1, \psi_2; n)$ across a tie-line read:

$$\begin{aligned}
\partial_m \mathcal{G}(\phi_1, \phi_2, m) &= 0 \\
\partial_n \mathcal{G}(\psi_1, \psi_2, n) &= 0 \\
D_{\phi_1} \mathcal{G}(\phi_1, \phi_2, m) &= D_{\phi_1} \mathcal{G}(\psi_1, \psi_2, n) \\
D_{\phi_2} \mathcal{G}(\phi_1, \phi_2, m) &= D_{\psi_2} \mathcal{G}(\psi_1, \psi_2, n) \\
\mathcal{G}(\psi_1, \psi_2, n) &= \mathcal{G}(\phi_1, \phi_2, m) + D_{\phi_1} \mathcal{G}(\phi_1, \phi_2, m)(\psi_1 - \phi_1) \\
&\quad + D_{\phi_2} \mathcal{G}(\phi_1, \phi_2, m)(\psi_2 - \phi_2)
\end{aligned} \tag{3.7}$$

It is important to realize that in the general case, the potential g_{mix} is not explicitly given, and that one must resort to the original expression for $\mathcal{G}$. The three last relations are the standard ones for obtaining the tie-lines, expressed in term of generalized derivatives, while the two first ones enforce the local minimization condition. The six unknown parameters $\phi_1, \phi_2, \psi_1, \psi_2, m, n$ obey five simultaneous relations. The resulting binary coexistence boundary can be parameterized by a one dimensional set of values, *e.g.* in terms of ϕ_1, in agreement with the Gibbs phase rule.

3.1.3 Equations for the limits of the triple coexistence region

The three conjugate points (ϕ_1, ϕ_2, m), (ψ_1, ψ_2, n), and (κ_1, κ_2, s) delimiting the triple coexistence region correspond to a triple contact with a tangent plane.

$$\begin{aligned}\partial_m \mathcal{G}(\phi_1, \phi_2, m) &= 0\\ \partial_n \mathcal{G}(\psi_1, \psi_2, n) &= 0\\ \partial_s \mathcal{G}(\kappa_1, \kappa_2, s) &= 0\end{aligned} \tag{3.8}$$

$$\begin{aligned}D_{\phi_1} \mathcal{G}(\phi_1, \phi_2, m) &= D_{\psi_1} \mathcal{G}(\psi_1, \psi_2, n) = D_{\kappa_1} g(\kappa_1, \kappa_2, s)\\ D_{\phi_2} \mathcal{G}(\phi_1, \phi_2, m) &= D_{\psi_2} \mathcal{G}(\psi_1, \psi_2, n) = D_{\kappa_2} \mathcal{G}(\kappa_1, \kappa_2, s)\\ \mathcal{G}(\psi_1, \psi_2, n) &= \mathcal{G}(\phi_1, \phi_2, m) + D_{\phi_1} \mathcal{G}(\phi_1, \phi_2, m)(\psi_1 - \phi_1) + D_{\phi_2} \mathcal{G}(\phi_1, \phi_2, m)(\psi_2 - \phi_2)\\ \mathcal{G}(\kappa_1, \kappa_2, s) &= \mathcal{G}\psi_1, \psi_2, m) + D_{\psi_1} \mathcal{G}(\psi_1, \psi_2, m)(\kappa_1 - \phi_1) + D_{\psi_2} \mathcal{G}(\psi_1, \psi_2, m)(\kappa_2 - \psi_2)\end{aligned} \tag{3.9}$$

3.1.4 Critical points

The spinodal line corresponds to the locus of points where the Hessian matrix (matrix of second derivatives) is singular. In most cases, the singular Hessian has possesses a single non degenerate eigenvector $\vec{E} = (E_{\phi_1}, E_{\phi_2})$ corresponding to the direction of vanishing Gibbs surface curvature. The critical points are the points where the eigenvector $\vec{E}$ is tangent to the spinodal line, or equivalently, normal to the gradient of the determinant of the Hessian.

$$\vec{E} \cdot \vec{\nabla} \det(\mathbf{H}) = 0 \tag{3.10}$$

This is because $\det(\mathbf{H})$ vanishes exactly on the spinodal line. The Hessian must be expressed with generalized derivatives:

$$\det(\mathbf{H}) = \begin{vmatrix} D^2_{\phi_1\phi_1}\mathcal{G} & D^2_{\phi_1\phi_2}\mathcal{G} \\ D^2_{\phi_1\phi_2}\mathcal{G} & D^2_{\phi_2\phi_2}\mathcal{G} \end{vmatrix} \tag{3.11}$$

The gradient of $\det(\mathbf{H})$ involves derivatives up to third order of $\mathcal{G}$:

$$\vec{\nabla} \det(\mathbf{H}) = \begin{pmatrix} (D^3_{\phi_1\phi_1\phi_1}\mathcal{G} \times D^2_{\phi_2\phi_2}\mathcal{G} - D^2_{\phi_1\phi_2}\mathcal{G} \times D^3_{\phi_1\phi_1\phi_2}\mathcal{G}) \\ +(D^2_{\phi_1\phi_1}\mathcal{G} \times D^3_{\phi_1\phi_2\phi_2}\mathcal{G} - D^3_{\phi_1\phi_1\phi_2}\mathcal{G} \times D^2_{\phi_1\phi_2}\mathcal{G}) \\ \\ (D^3_{\phi_1\phi_1\phi_2}\mathcal{G} \times D^2_{\phi_2\phi_2}\mathcal{G} - D^2_{\phi_1\phi_2}\mathcal{G} \times D^3_{\phi_1\phi_2\phi_2}\mathcal{G}) \\ +(D^2_{\phi_1\phi_1}\mathcal{G} \times D^3_{\phi_2\phi_2\phi_2}\mathcal{G} - D^3_{\phi_1\phi_2\phi_2}\mathcal{G} \times D^2_{\phi_1\phi_2}\mathcal{G}) \end{pmatrix} \tag{3.12}$$

We can choose for the eigenvector $\vec{E}$ the following pair:

$$\vec{E} = \begin{pmatrix} D^2_{\phi_2\phi_2}\mathcal{G} \\ -D^2_{\phi_1\phi_2}\mathcal{G} \end{pmatrix} \tag{3.13}$$

The critical points correspond to the solutions (ϕ_1, ϕ_2, m) of the following system of three nonlinear equations:

$$\begin{aligned} \partial_m \mathcal{G} &= 0 \\ \det(\mathbf{H}) &= 0 \\ \vec{E} \cdot \vec{\nabla} \det(\mathbf{H}) &= 0 \end{aligned} \tag{3.14}$$

We list the generalized derivatives of $\mathcal{G}$ in term of partial derivatives of $\mathcal{G}(\phi_1, \phi_2, m)$, and give the expressions our specific case in the appendix (E).

3.2 Refinements of the DOPC/DPPC/Cholesterol Gibbs diagram

We use the above set of equations to determine all the boundaries in the Gibbs triangle using numerical equation solving iterative schemes, starting from the discrete convex minimization of g_{mix} (Mathematica).

We observe on figure (3.2) the refinements of the Gibbs diagram, which give in blue the position of the critical point, in red the tie-lines and in green the ternary coexistence domain. The set of parameters of our model $\{\tilde{J}, \delta, \xi, \chi\}$ was determined in

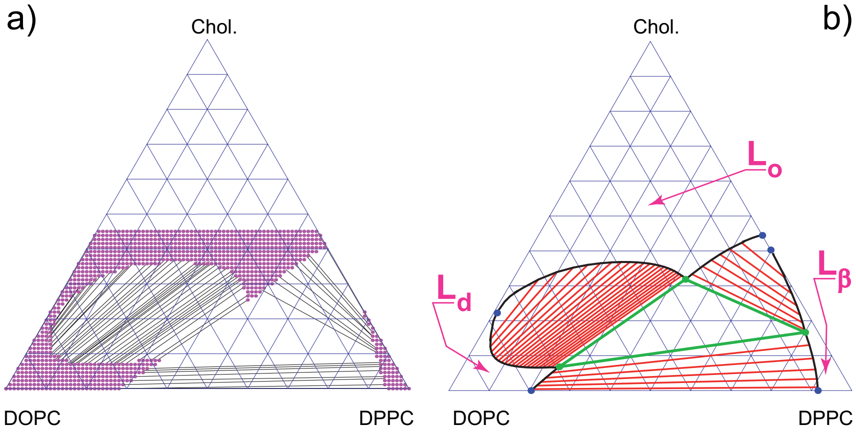

Figure 3.2 – *(a) Projected Gibbs diagram obtained after qhull calculation, viewed from below. (b) Analytical refinement leading to our final diagram.*

Ternary	χ	ξ	δ	$\tilde{J}$	$\Delta H_1^{(*)}$	$\Delta H_2^{(*)}$	$T_1^{(*)}$	$T_2^{(*)}$
DOPC/DPPC	6	1.8	2.2	0.35	7.7	8.7	-21.1	37.8
DOPC/PSM	6	1.8	2.2	0.35	7.7	7.5	-21.1	41
POPC/PSM	6.3	1.8	2.2	0.35	5.4	7.5	-3	41
DiPhy/DPPC	6.6	2	2.4	0.35	7.4	8.7	-120	37.8

Table 3.1 – *Tabular of data for our model.*
(*)ΔH en kcal/mol et T en °C.

the previous chapter for the DOPC/DPPC/Chol mixture. It is of prime importance to test the predictive power of the model by considering other ternary mixtures as well. For that, we consider the ternary phase diagrams of several ternary mixtures, namely: DOPC/DPPC/Chol., POPC/PSM/Chol., DiPhytanoyl/DPPC/Chol., and DOPC/PSM/Chol.

We also analyze the behavior of these ternary mixtures by computing the evolution of the diagrams for at least two different temperatures. The values used for each ternary mixture are summarized in Table (3.1). For the three first cases χ was adjusted to provide the best possible agreement with experimental data at low temperature. We notice that the values are fairly constant, and do not depend on the lipid species, but on the thermodynamic constraints. In the last case we had to change also ξ and δ. The reason is probably because DiPhytanoyl-PC has a different kind of melting transition, taking place at very low temperature.

3.2.1 DOPC/DPPC/Cholesterol

We plotted on figure (3.3) the computed Gibbs diagram, and aside the experimental diagram arising from NMR measurements at two temperatures [68]. We can compare the evolution of the binary and the ternary domains with respect to temperature. First, we remark that at T = 10 °C, the measures confirm the presence of a ternary triangular zone which disappears at about T = 30°C, and secondly the bubble binary coexistence zone swells but does not touch the left side of the Gibbs diagram. The evolution of the Gibbs diagram with respect to temperature is displayed in figure (3.4) in a single prism. The diagram was drawn here under the assumption of a constant ξ parameter, and a constant value of the coupling contribution $k_B T \cdot \chi$

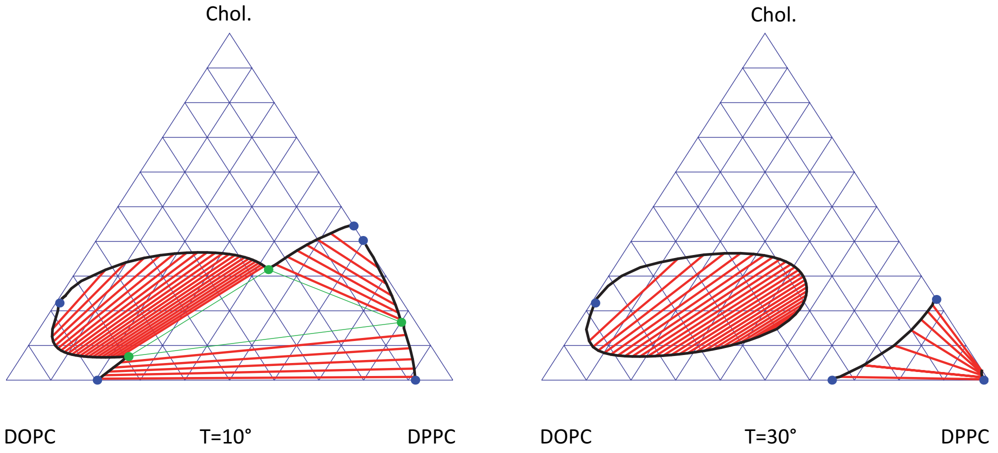

(a) Ternary diagram at T = 10°C (left) and T = 30°C (right). J = 0.35, δ = 2.2, ξ = 1.8, χ = 6

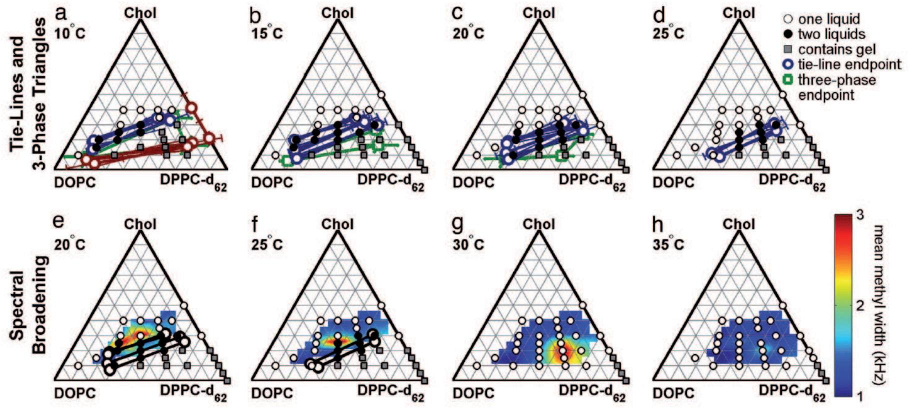

(b) Experimental results with NMR. [68].

Figure 3.3 – *DOPC/DPPC/Chol.*

denoting its pure enthalpic nature. Our diagram at the lower temperature in figure (3.4) displays the main expected features for a DOPC/DPPC/Chol mixture. As the temperature increases, the triple coexistence triangle shrinks and vanishes between 15°C and 20°C. Also, the L_o/L_d biphasic region, resting initially on the left side of the triangle, detaches and assumes a closed shape of decreasing area. A first critical point, on the left side of the Gibbs diagram, evolves slowly away from the edge [68]. A second critical point, initially hidden by the triple coexistence region, is predicted to emerge at the binary detachment temperature. Note also that within our approach the extension of the L_β domain, on the right bottom part of the diagram, gradually decreases up to T_2.

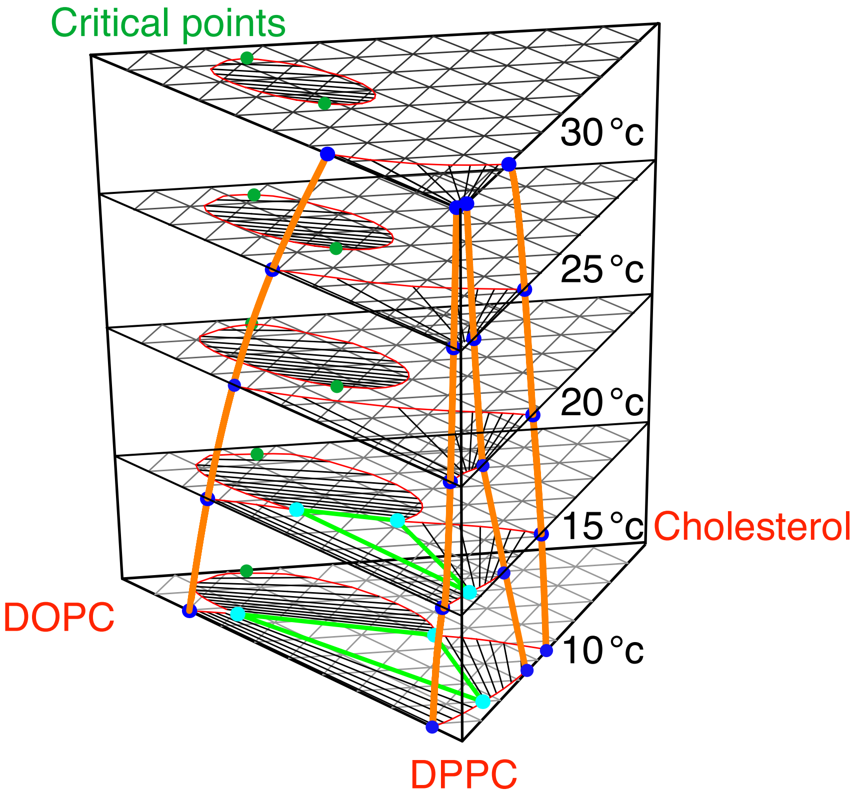

Figure 3.4 – *Computed evolution of the DPPC/DOPC/Chol triangular diagram with temperature. The computed diagrams display the main expected features for this lipid mixtures.*

3.2.2 DOPC/PSM/Cholesterol

Sphingomyeline is a phospholipid with a choline head but no glycerol backbone, and two inequivalent tails. One of the tail is variable, linked with an amide bond to the sphingosine chain. In PSM, this chain has 16 carbon atoms (the same as DPPC). The resulting transition temperature is close to the DPPC melting temperature. Sphingomyeline is an important component of cell membranes and contribute with

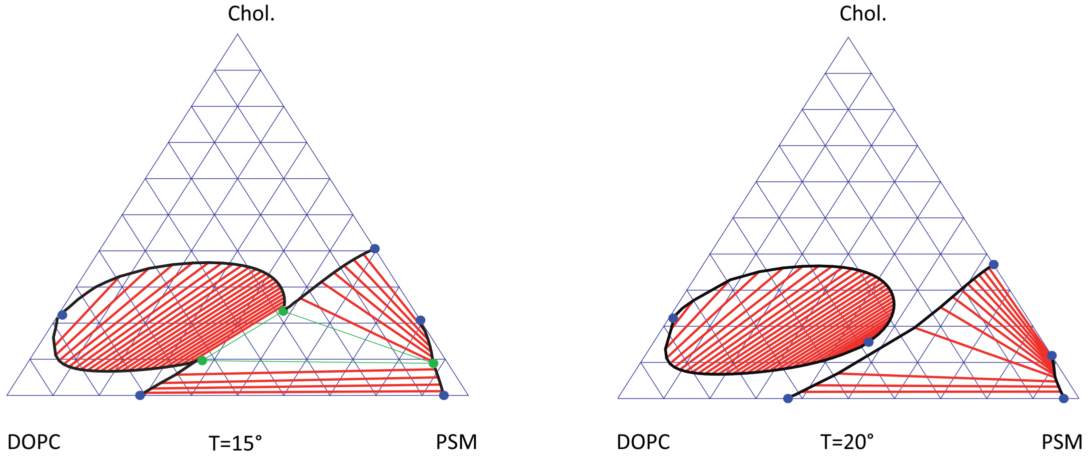

(a) DOPC/PSM/Chol. ternary diagram at T = 15°C and T = 20°C. $J = 0.35$, $\delta = 2.2$, $\xi = 1.8$, $\chi = 6$.

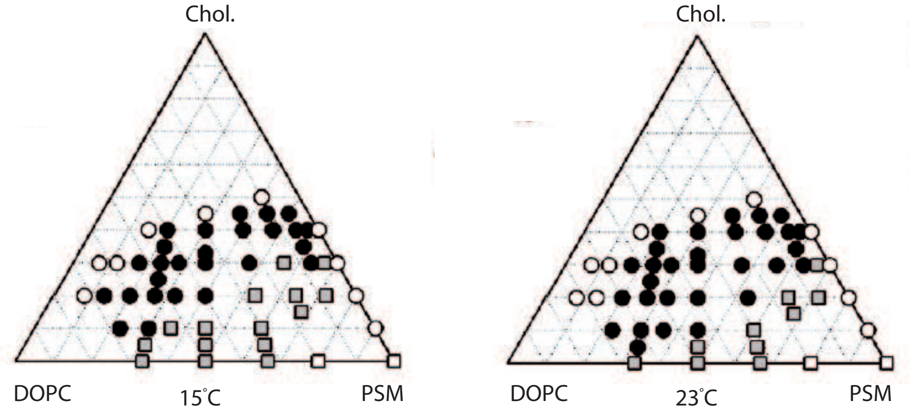

(b) DOPC/PSM/Chol. ternary diagram at T = 15°C and T = 23°C. Experimental results with fluorescence microscopy [86]. White symbols denote that membranes are in a single uniform phase, either liquid (circles) or solid (squares). Black circles denote coexisting liquid phases, and gray squares denote coexisting solid and liquid phases.

Figure 3.5 – *DOPC/PSM/Chol.*

cholesterol to form raft. So it it of prime importance to understand better the behavior of PSM, cholesterol and unsaturated lipid mixtures. We observe on figure (3.5) the computed diagrams and the fluorescence microscopy experimental measures. First, at T = 15°C, we notice on figure (3.5.b) a binary liquid/liquid phase coexistence domain at the center of the triangle (black circles) which swells at T = 23°C, as we find in our computed diagram (3.5.a). Secondly the diagram presents an other binary liquid/solid phase coexistence (gray squares) under the liquid/liquid coexistence domain, which shrinks at T = 23°C as we find in our computed triangle. Notice that our model predicts a ternary phase coexistence region as a recent compilation of experimental diagrams clearly shows [87]. Finally the two diagrams present a critical point on the left of the liquid/liquid domain, even if its position in our computed triangle is a too skewed to the left.

3.2.3 POPC/PSM/Cholesterol

After having substituted for the gel forming component in the previous diagram (PSM instead of DPPC), we consider now the consequences of substituting the fluid component DOPC in favor of POPC . POPC is a phospholipid with two different tails, a 16 carbons saturated chain at the *sn-1* position, and a 18 carbon unsaturated chain at the *sn-2* position. The *cis* insaturation occupies the 9th position, as in DOPC. POPC is considered as an hybrid lipid because of the dual fluid and gel character of the two tails, which are forced to coexist.

Brewster and Safran postulated that this unique property could confer to POPC the ability to mix equally well with the fluid and gel phases. In other words, POPC could be the natural *lineactant* (by analogy with *surfactant*) of biological membranes, and could play an fundamental role for promoting the formation of small domains and rafts [88]. This group investigated theoretically the influence of POPC on the gel and fluid boundaries, and concluded that it was indeed possible to lower in this way the line tension between these regions. The presence of POPC in biomembranes suggests that it is an important player in lateral separation phenomena.

We can compare the experimental results in figure (3.7) and our computed diagram in figure (3.6), and notice that the binary mixture of POPC and cholesterol gives a coexistence domain at about T=20°C which disappears at about T=25°C in our diagram. Both diagrams present a ternary phase coexistence domain at T = 25°C. Our diagram is consistent with the experiment data, whether one considers the phase boundaries or the transition temperatures.

In ref. [69], ternary coexistence was not seen at T = 37°C due to technical limitations with only a putative ternary coexistence zone represented with a dashed red line.(figure3.7)

The presence of domains in binary POPC cholesterol mixtures is a matter of controversy. Large domains are never seen while evidence of small domains (spectroscopic techniques) seem to exist.

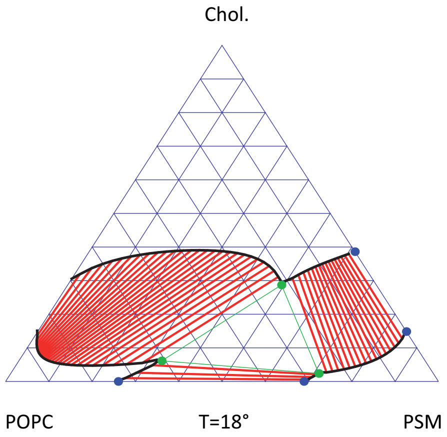

Figure 3.6 – *POPC/PSM/Chol. ternary diagram at* $T = 18$°C *and* $T = 25$°C. $J = 0.35$, $\delta = 2.2$, $\xi = 1.8$, $\chi = 6.3$

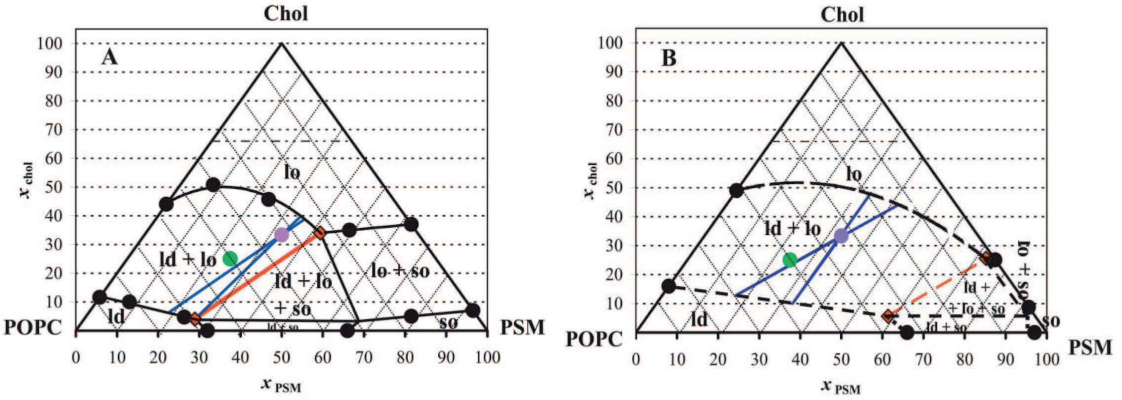

Figure 3.7 – *POPC/PSM/Chol. ternary diagram at* $T = 23$°C *(A) and* $T = 37$°C *(B). Experimental results with fluorescence microscopy and DSC method[69].*

3.2.4 DiPhytanoyl/DPPC/Cholesterol

Diphytanoyl is multi-branched acyl chain (figure 3.8) which was characterized by Lindsey and Chan in 1979 [89]. It has a very low melting temperature, estimated at $T < 120$°C. The bulky methyl groups work against the regular chain arrangements and the concomitant gain in cohesion energy which is the signature of the gel phase, thus disfavoring it on the thermodynamic point of view. The chains remains soft enough to preserve the fluidity of the bilayer. Diphytanoyl is a lipid of choice when one wishes to combine membrane fluidity and chemical stability such as the resistance to oxidative stress.

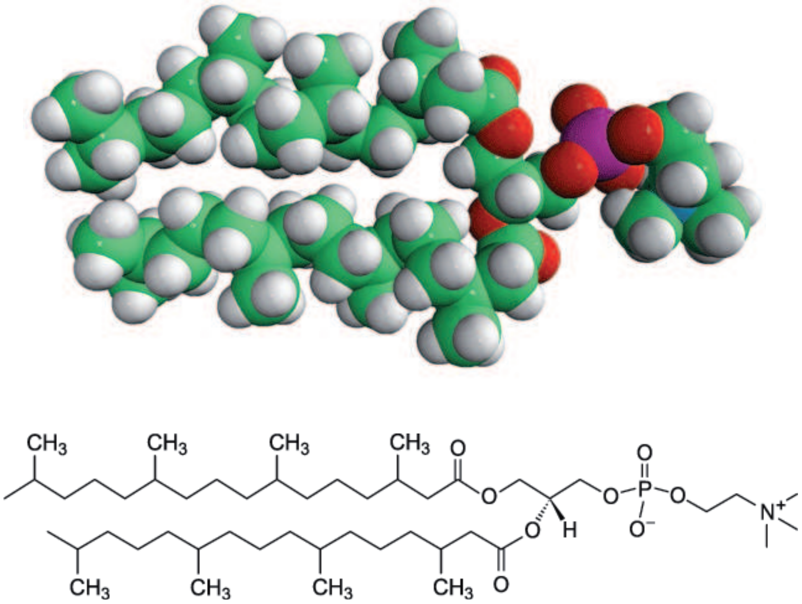

Figure 3.8 – *Diphytanoyl representation.*

Our model takes in account the transition temperature of the lipid species. We show below the experimental results obtained by NMR and notices on both diagrams the same topology of domains at comparable temperatures. First at $T = 16$°C, the diagram displays a triangle ternary domain and a binary bubble zone which is a slightly too swollen towards the left in the predicted diagram, while it is inflated towards the top in the experimental diagram. Moreover, the bubble deflates at the same temperature while the triangle disappears in the same time.

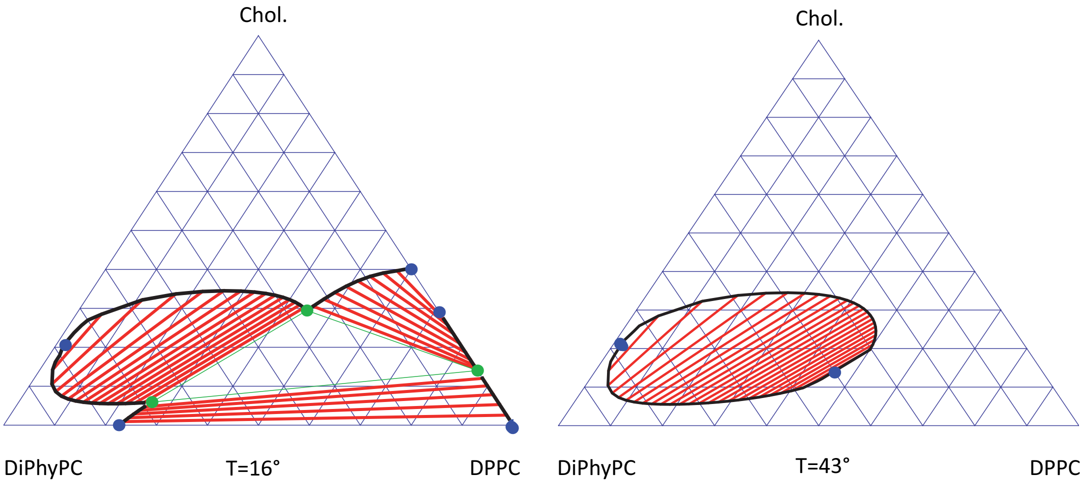

Figure 3.9 – *DiPhy./DPPC/Chol. ternary diagram at T=16°C and T=43°C.* $J = 0.35$, $\delta = 2.4$, $\xi = 2$, $\chi = 6.6$

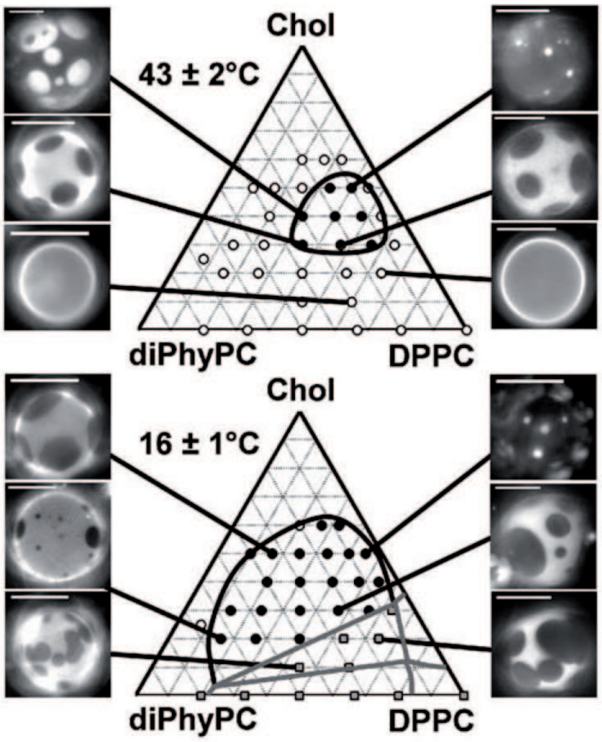

Figure 3.10 – *DiPhy./DPPC/Chol. ternary diagram at T = 16°C and T = 43°C. Experimental results with NMR method[90].*

3.3 Area changes in binary mixtures

In the previous chapter, we built the phase diagram of lipid/lipid binary mixtures without considering changes in the area per molecule. In this section, we suggest a way to take into account the variation of area per molecule occurring during the liquid-gel transition, based on the Flory-Huggins expression for the entropy of mixing of macromolecules with dissimilar molecular weights. We do not take into account cholesterol in this study.

The area per molecule increases at the transition by 15 to 20%. The authors of ref. [32] have performed structural studies of DPPC bilayers at 20 and 50°C (below and above the transition), and find the following values for the molecular volume, area per lipid and membrane thickness:

	20°C	50°C
V (Å^3)	1144	1232
a (Å^2)	47.9	64
D (Å)	44.2	38.3

In order to allow for changes in the area per molecule, it is necessary to work with the molecular fractions and not with the surface fractions as until now. If we assume a change in area per molecule, the total area of the system is not conserved, and the surface fraction is not well defined when molecules commute between gel and liquid states, and vice-versa.

We consider the molecular fractions x_i=$N_i/(N_1+N_2)$ of each components, along with a new expression of the Gibbs free energy $f_{\text{mix}} = \beta G_{\text{mix}}/(N_1+N_2)$, where N_1+N_2 is the total number of the molecules and N_1, N_2 the number of molecules of each species of lipids. We naturally assume that the number of molecules do not change, these ones being only converted internally back and forth, from the gel to the liquid state. We assume that the species 1 has N_A molecules in their liquid state, and N'_A molecules in their gel state, while the species 2 has N_B molecules in their liquid state, and N'_B molecules in their gel state. As a result, N_1= N_A+N'_A and N_2= N_B+N'_B (figure 3.11). Our notations are the following: $x_A = N_A/(N_A+N_B)$ and $x_B = N_B/(N_A+N_B)$ are the molecular fractions of the two lipids in the fluid state, $x'_A = N'_A/(N'_A+N'_B)$ and $x'_B = N'_B/(N'_A+N'_B)$ are the molecular fractions of the two lipids in the gel state.

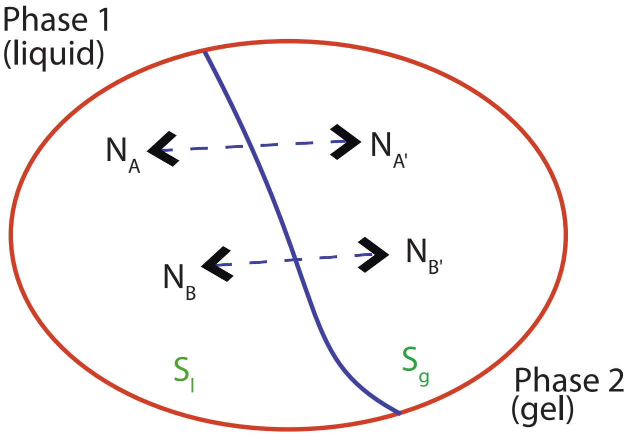

Figure 3.11 – *Phase separation in a binary mixture of lipids.*

Unlike what was done in the previous sections, we take here the limit $m = 1$ and $m = -1$ of our Gibbs free-energies, following in that sense the conventional approach, with two strictly disconnected phases. We therefore derive the expression of $f_{\text{mix}}(liq.)$, free-energy density in the liquid state $(m = 1)$ in terms of x_A, x_B, and of $f_{\text{mix}}(gel)$ in the gel state $(m = -1)$ in terms of x'_A, x'_B.

3.3.1 Calculation of $f_{\text{mix}}(liq.)$ and $f_{\text{mix}}(gel.)$

We consider that the fluid surface is S_l, and the gel surface S_g, such as $\mathcal{A} = S_l + S_g$ with $\phi_A = aN_A/S_l$, $\phi_B = bN_B/S_l$ in the liquid state and $\phi'_A = a'N'_A/S_g$, $\phi'_B = b'N'_B/S_g$ in the gel state. The parameters a, b, a', b' are the specific areas per molecule of the species A,B in their respective phases.

This leads to the relations between molecular and surface fractions

$$\begin{aligned}
\phi_A &= \frac{ax_A}{ax_A + bx_B} \\
\phi_B &= \frac{bx_B}{ax_A + bx_B} \\
\phi'_A &= \frac{a'x'_A}{a'x'_A + b'x'_B} \\
\phi'_B &= \frac{b'x'_B}{a'x'_A + b'x'_B}
\end{aligned} \tag{3.15}$$

$$
\begin{aligned}
x_A &= \frac{\phi_A/a}{\phi_A/a + \phi_B/b} \\
x_B &= \frac{\phi_B/b}{\phi_A/a + \phi_B/b} \\
x'_A &= \frac{\phi'_A/a'}{\phi'_A/a' + \phi'_B/b'} \\
x'_B &= \frac{\phi'_B/b'}{\phi'_A/a' + \phi'_B/b'}
\end{aligned}
\tag{3.16}
$$

In order to introduce the area per molecule, we set $g_{\text{mix,liq.}}$ and $g_{\text{mix,gel}}$ two dimensionless quantities separating the liquid state ($m = 1$) and the gel state ($m = -1$) and obtain:

$$
g_{\text{mix,liq.}} = \mathcal{A}\left[\frac{\phi_A}{a}\ln(\phi_A) + \frac{\phi_B}{b}\ln(\phi_B) - [h^{(1)}(T)\frac{\phi_A}{a} + h^{(2)}(T)\frac{\phi_B}{b}]\right]
$$

$$
g_{\text{mix,gel}} = \mathcal{A}\left[\frac{\phi'_A}{a'}\ln(\phi'_A) + \frac{\phi'_B}{b'}\ln(\phi'_B) + [h^{(1)}(T)\frac{\phi'_A}{a'} + h^{(2)}(T)\frac{\phi'_B}{b'}]\right] \tag{3.17}
$$

The first equality is obtained as a limit $m = 1$ of a Flory-Huggins entropy of mixing term, and the second as a limit $m = -1$ of the same expression.

We substitute the surface fractions with the molecular fractions and obtain:

$$
g_{\text{mix,liq.}} = N_A \ln\left(\frac{ax_a}{ax_a + bx_b}\right) + N_B \ln\left(\frac{bx_b}{ax_a + bx_b}\right) - (h^{(1)}(T)N_A + h^{(2)}(T)N_B)
$$

$$
g_{\text{mix,gel}} = N'_A \ln\left(\frac{a'x'_a}{a'x'_a + b'x'_b}\right) + N'_B \ln\left(\frac{b'x'_b}{a'x'_a + b'x'_b}\right) + (h^{(1)}(T)N'_A + h^{(2)}(T)N'_B) \tag{3.18}
$$

Finally we set $f_{\text{mix,liq.}} = g_{\text{mix,liq.}}/(N_A + N_B)$ and $f_{\text{mix,gel}} = g_{\text{mix,gel}}/(N'_A + N'_B)$:

$$
\begin{aligned}
f_{\text{mix,liq.}} = {} & x_A \ln(ax_A) + (1 - x_A)\ln(b(1 - x_A)) - [h^{(1)}(T)x_A + h^{(2)}(T)(1 - x_A)] \\
& - \ln(x_A(a - b) + b)
\end{aligned}
\tag{3.19}
$$

and

$$
\begin{aligned}
f_{\text{mix,gel}} = {} & x'_A \ln(a'x'_A) + (1 - x'_A)\ln(b(1 - x'_A)) + [h^{(1)}(T)x'_A + h^{(2)}(T)(1 - x'_A)] \\
& - \ln(x'_A(a' - b') + b')
\end{aligned}
\tag{3.20}
$$

We apply the Gibbs conditions for binary coexistence, rewrite the result in terms of surface fractions, to obtain finally the following set of equations:

$$\begin{aligned}\ln[\frac{1-\phi_A}{1-\phi'_A}] + \phi_A\frac{a-b}{a} - \phi'_A\frac{(a'-b')}{a'} - 2h^{(2)}(T) = 0\\ \ln(\frac{\phi_A}{\phi'_A}) + (1-\phi_A)\frac{b-a}{b} - (1-\phi'_A)\frac{b'-a'}{b'} - 2h^{(1)}(T) = 0\end{aligned} \tag{3.21}$$

3.3.2 Calculation of the slopes of each branches in the binary diagram at $\phi_{DOPC} = 0$.

The binary coexistence diagram is obtained by solving numerically the set of equations (3.21). It is possible to extract analytically the slopes of the coexistence lines in the limit ϕ_A, $\phi'_A \ll 1$ and $(1-\phi_A)$, $1-\phi'_A) \ll 1$. For instance, the expansion of (3.21) at low ϕ_A, ϕ'_A leads to

$$\left\{\begin{array}{ccc} \phi'_A\frac{b'}{a'} - \phi_A\frac{b}{a} & = & 2h^{(2)}(T) \\ \ln(\frac{\phi_A}{\phi'_A}) + \frac{b-a}{b} - \frac{b'-a'}{b'} & = & 2h^{(1)} \end{array}\right. \tag{3.22}$$

This expansion is consistent with

$$2h^{(2)}(T) \simeq \frac{(\Delta H_2)}{RT^2_{m,2}}(T - T_{m,2}) = C_B(T - T_{m,2}), \tag{3.23}$$

and

$$2h^{(1)} \simeq \frac{(\Delta H_1)}{RT^2_{m,1}}(T_{m,2} - T_{m,1}) = C_A(T - T_{m,2}) \tag{3.24}$$

where $2h^{(1)}$ is a positive constant. Alternatively, one may write a system of equations for the slopes.

$$\left\{\begin{array}{ccc} \frac{1}{\phi_A}\frac{d\phi_A}{dT} - \frac{1}{\phi'_A}\frac{d\phi'_A}{dT} + \frac{(a-b)}{b}\frac{d\phi_A}{dT} + \frac{(b'-a')}{b'}\frac{d\phi'_A}{dT} & = & C_A \\ \frac{d\phi'_A}{dT} - \frac{d\phi_A}{dT} + \frac{(a-b)}{a}\frac{d\phi_A}{dT} + \frac{(b'-a')}{a'}\frac{d\phi'_A}{dT} & = & C_B \end{array}\right. \tag{3.25}$$

with again $C_A = \frac{\Delta H_1}{RT_1^2}$ and $C_B = \frac{\Delta H_2}{RT_1^2}$. The second equation in (3.22) gives:

$$\frac{\phi_A}{\phi'_A} = \exp(2h^{(1)} + \frac{a}{b} - \frac{a'}{b'}) \tag{3.26}$$

After substitution of ϕ_A, we obtain:

$$\frac{d\phi'_A}{dT}|_{\phi_A=0} = \frac{(\Delta H_2)}{RT^2_{m,2}} \frac{\frac{a}{b}}{(\frac{b'a}{a'b}) - \exp(2h^{(1)} + \frac{a}{b} - \frac{a'}{b'})} \tag{3.27}$$

$$\frac{d\phi'_A}{dT}|_{\phi_A=0} = \frac{(\Delta H_2)}{RT^2_{m,2}} \frac{\frac{a}{b}\exp(2h^{(1)} + \frac{a}{b} - \frac{a'}{b'})}{(\frac{b'a}{a'b}) - \exp(2h^{(1)} + \frac{a}{b} - \frac{a'}{b'})} \tag{3.28}$$

Real slopes $dT/d\phi_A$ and dT/ϕ'_A follows immediately.

We consider a situation where the melting temperature of the first species is lower than the one of the second species ($T_1 < T_2$). When $\phi_{DOPC} \simeq 0$, one has $T \simeq T_2$, and consequently $h^{(1)}(T) \gg 1$, $h^{(2)}(T) \ll 1$ and $h_2(T) < 0$. To illustrate this effect, we also assume that $\frac{a}{a'} \simeq \frac{b}{b'}$. The new slopes $\frac{dT}{d\phi'_A}(\phi_a = 0)$, and $\frac{dT}{d\phi_A}(\phi_a = 0)$ therefore read:

$$\frac{dT}{d\phi'_A}(\phi_A = 0) = -\frac{(\exp(2h^{(1)}(T) + \frac{a}{b} - \frac{a'}{b'})}{2C_B\frac{a}{b}} \tag{3.29}$$

and

$$\frac{dT}{d\phi_A}(\phi_A = 0) = -\frac{b}{2aC_B} \tag{3.30}$$

3.3.3 Binary phase diagram with area variation

We observe that the slopes depend on the two ratios a/b and a'/b'. The neighborhood of $\phi_A \simeq 0$ is controlled by the ratio a/b provided a/b and a'/b' are small in front of $2h^{(1)}$. Conversely, the neighborhood of $\phi_A \simeq 1$ is controlled by the ratio a'/b', provided a/b and a'/b' are small in front of $2h^{(2)}$.

We computed the binary diagrams for decreasing ratios $b/a \simeq b'/a'$, in order to reduce the slopes of the two branches, with the constraints that the liquid phase area per molecule is larger than the gel phase area. We set $b = 1.4$, $a = 2$, $b' = 1$ and $a' = 1.8$ and plot in green color the binary diagram, with on the same figure in red the initial diagram corresponding to the constant areas (figure 3.12). We notice some improvement of the diagram due to the change in area at the liquid/gel transition. The use of a Flory-Huggins entropy of mixing is here phenomenological, but allows us to correct to some extent the shape of binary lipid phase diagram.

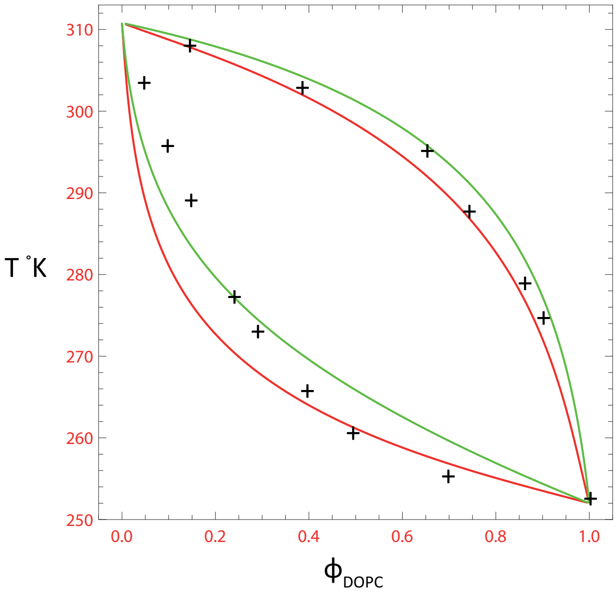

Figure 3.12 − *DOPC/DPPC binary diagram: experimental values represented with black crosses, in red the model without area variation, in green the model with area variation.*

3.3.4 Generalization for surface tension, and hydrostatic pressure

The previous calculation is only correct provided the membrane tension is low enough, which is usually considered as true. We can attempt to generalize the expression of f_{mix} by introducing the lateral membrane tension and the hydrostatic pressure. Tension and pressure play to that respect the same role as temperature in our thermodynamic model.

The intensive surface tension γ is conjugated with changes in molecular area Δ_a, and the intensive pressure P is conjugated with the variation of specific volume Δv_a of the molecules. Temperature was conjugated to enthalpy in the two first section (if one considers $\mathcal{G}$ instead of $\beta\mathcal{G}$, temperature is conjugated with entropy). We outline below the way our formalism should be extended to account for mechanical stresses. The expression for the lipid state ($m = 1$) is

$$\begin{aligned} f_{\text{mix}}(liq.) = {} & x_A \ln(ax_A) + x_B \ln(bx_B) - \ln(ax_A + bx_B) \\ & -m[h^{(1T)}(T)x_A + h^{2T}(T)x_B + h^{(1\gamma)}(\gamma)x_A \\ & +h^{(2\gamma)}(\gamma)x_B + h^{(1P)}(P)x_A + h^{(2P)}(P)x_B] \end{aligned} \tag{3.31}$$

with

$$h^{(1T)}(T) = (T - T_{ref})\Delta_a \tag{3.32}$$

$$h^{(1\gamma)}(\gamma) = (\gamma - \gamma_{ref})\Delta_a a \tag{3.33}$$

and

$$h^{(1P)}(P) = (P - P_{ref})\Delta v_a \tag{3.34}$$

The gel state is similar, and can be obtained by changing $a \to a'$, $b \to b'$, $A \to A'$, $B \to B'$.

Chapter 4

Line tension and Wetting

4.1 Line tension

4.1.1 Introduction

Giant Unilamellar Vesicles (GUV's) made from ternary mixtures of one unsaturated lipid such as DOPC, a saturated lipid like DPPC or sphingomyelin (SM) and cholesterol provide a convenient and direct experimental platform to observe and study phase coexistence between liquid-order and liquid-disorder domains. In this geometry, the phase separated vesicle usually displays two domains with different curvatures as shown in fig. 4.1. The crossover region between the domains, that can be described at the macroscopic level as a line, is the analog in these two-dimensional systems, of the water-vapour or the water-oil interfaces that separate two macroscopic phases at coexistence in three-dimensional systems. The cost of creating such a linear interface, the so called line-tension, is measured in units of energy per unit length or force. The line tension plays an important role in determining the shapes of vesicles with phase separated domains[91]. By determining vesicle shape under a fluorescent microscope while controlling membrane tension by micropipette suction one can precisely measure values for the line tension, for instance as a function of membrane composition. Typical values of line tension between two fluid phases are of order of 1 pN [92, 93].

In this chapter, we first extend our thermodynamic theory for phase coexistence in ternary lipid mixtures in order to account for composition inhomogeneities, thus providing for theoretical predictions of line-tension values as a function of lipid membrane composition, and for a direct comparison with experimental results. Then, we

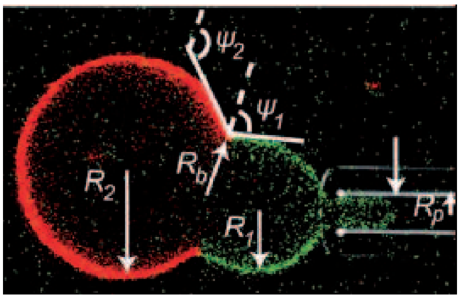

Figure 4.1 — *Measurement of the line tension between two phase-separated liquid-ordered and liquid-disordered domains. Given the pressure suction* ΔP *applied by micropipette aspiration and the different geometrical parameters shown in the figure, one can obtain the line tension values from* $\tau = \Delta P(\cot\psi_1 - \cot\psi_2)({R_b}^2 R_P \sin\psi_1)/(2(R_b - R_P \sin\psi_1))$*[91].*

will consider the consequences of inserting proteins or other inclusions in a ternary lipid membrane. The interplay of inclusion-lipid affinities may lead to phenomena, in these two-dimensional systems, akin to wetting at interfaces between three-dimensional coexisting phases [77]. After reviewing the classic concepts of wetting theory, we study how the local lipid environment can be modified in the close vicinity of an inclusion such as a protein.

4.1.2 The Landau-Ginzburg energy functional for an interface

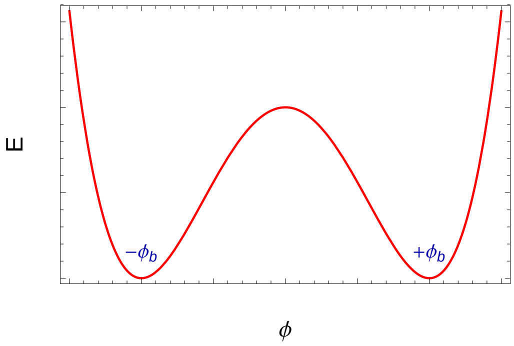

Figure 4.2 — *Schematic representation ("Mexican Hat") of the bulk energy density of two coexisting phases, with equilibrium values of order parameters* ϕ_b *and* $-\phi_b$*.*

A standard thermodynamic description of the interface between two coexisting phases is provided by the Landau-Ginzburg energy functional of the local order parameter $\phi(z)$ where z is the distance from the interface. For a magnetic system $\phi(z)$ would refer to the local magnetisation while for a binary system $\phi(z)$ would measure the local composition of one of the components. We recall here the simplest version of this description where two semi-infinite bulk phases of order parameter ϕ_b and $-\phi_b$ are separated by a flat interface. The order parameter $\phi(z)$ varies continuously from $-\phi_b$ to ϕ_b as z spans the whole system from $-\infty$ to $+\infty$. The most relevant variation takes place over a distance ξ around the interface position at $z = 0$. ξ is often referred to as the interfacial thickness. The Landau-Ginzburg functional $\mathcal{F}$

$$\mathcal{F} = \int_{-\infty}^{+\infty} \left[\frac{a}{2} \left(\frac{\mathrm{d}\phi}{\mathrm{d}z} \right)^2 + \frac{b}{2} \left(\phi^2 - {\phi_b}^2 \right)^2 \right] \mathrm{d}z \tag{4.1}$$

considers two contributions to the local energy density at height z-see equation (4.1). The first is the relevant Legendre transform of the bulk energy density displayed in figure (fig. 4.2) as a “ Mexican Hat“, a shape that reinforces constant chemical potential and osmotic pressure across the interface. The second contribution measures surface inhomogeneities by a quadratic gradient term. The equilibrium order parameter $\phi(z)$ is obtained by functional minimization of with respect to ϕ, leading to the associated Euler-Lagrange differential equation

$$-a \frac{\mathrm{d}^2\phi}{\mathrm{d}z^2} + 2b\phi(\phi^2 - {\phi_b}^2) = 0 \tag{4.2}$$

to be solved with boundary conditions, $-\phi(-\infty) = \phi(\infty) = \phi_b$ and $d\phi/dz|_{-\infty} = d\phi/dz|_{\infty} = 0$.

By introducing the reduced order parameter $Y = \phi/\phi_b$ and the length $\xi^{-2} = b{\phi_b}^2/a$ equation 4.2 can be rewritten as:

$$\frac{\mathrm{d}^2 Y}{\mathrm{d}z^2} = \frac{2}{\xi^2} Y(Y^2 - 1) \tag{4.3}$$

with the associated first integral

$$\left(\frac{\mathrm{d}Y}{\mathrm{d}z} \right)^2 = \frac{1}{\xi^2} (Y^2 - 1)^2 \ . \tag{4.4}$$

The solution of equation 4.4 is given by $Y(z) = \tanh(z/\xi)$, the profile $\phi(z)$ being thus written as $\phi(z) = \Delta/2 \tanh(z/\xi)$, with $\Delta = 2\phi_b$ as sketched in figure (4.3).

The interfacial energy τ associated with the inhomogeneous profile can be computed by replacing the equilibrium profile $Y(z)$ into the reduced form of the Landau-

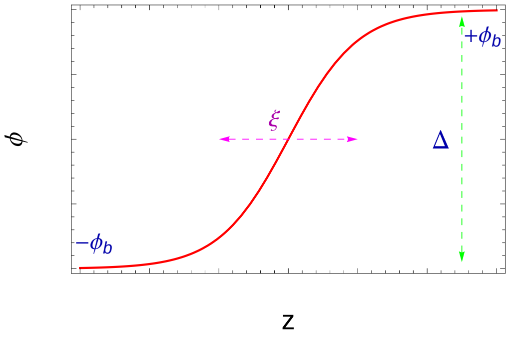

Figure 4.3 – *Equilibrium inhomogeneous profile of the order parameter $\phi(z)$ that minimizes the Landau-Ginzburg functional for an interface separating two coexistence phases of order parameters $-\phi_b$ and ϕ_b. The chemical difference between the two phases is measured by $\Delta = 2\phi_b$, ξ is the typical thickness of the interface.*

Ginzburg functional:

$$\tau = b{\phi_b}^4\xi \int_{-\infty}^{\infty} \left[\frac{1}{2}\left(\frac{\mathrm{d}Y}{\mathrm{d}\tilde{z}}\right)^2 + \frac{1}{2}(Y^2-1)^2 \right] \mathrm{d}\tilde{z} \tag{4.5}$$

with $\tilde{z} = z/\xi$. Note that the prefactor of the numerical integral can be viewed as the product of the typical scale for the bulk energy density $b{\phi_b}^4$ by the interfacial length ξ. For interfaces separating two three dimensional bulk phases at coexistence, $b{\phi_b}^4$ is an energy per unit volume and τ has thus the dimensions of a surface tension. For two coexisting bulk phases in two dimensions $b{\phi_b}^4$ is an energy per unit surface and τ measures the line tension between the two phases. By using the identity $\int_{-1}^{1}(1-Y^2)\,\mathrm{d}Y = 4/3$, one gets:

$$\tau = \frac{4b{\phi_b}^4\xi}{3} = \frac{a\Delta^2}{3\xi} \simeq \Delta^3 \tag{4.6}$$

Notice that τ scales as $\tau \approx \Delta^3$, where Δ measures the length of the tie-line between two coexisting phases, a classical result for this mean field description of the interfacial energy. In the following paragraph we extend the Landau-Ginzburg description of the interface to ternary lipid mixtures that involves two order parameters.

4.1.3 Interface between L_o and L_d domains

We consider the coexistence between the liquid ordered and liquid disordered phases in a ternary mixture of saturated and unsaturated lipids and cholesterol, governed by the Gibbs free energy $\mathcal{G}(\phi_1, \phi_2, m)$ introduced in the chapter 2, equation 2.33, where ϕ_1 and ϕ_2 are the surface fractions of each lipid, and m an order parameter associated with the tails.

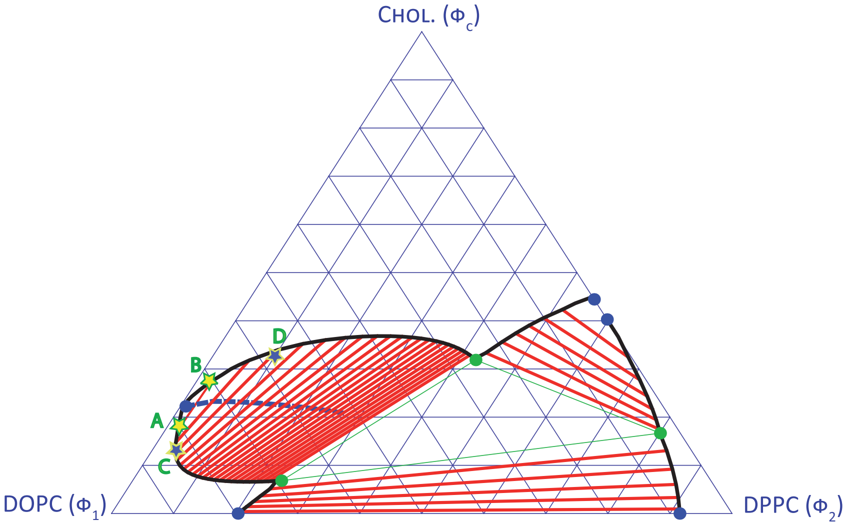

Figure 4.4 – *Gibb's diagram for the mixture DOPC/DPPC/cholesterol.*

We seek for a desription of the composition inhomogeneities $\phi_1(z)$ and $\phi_2(z)$ as z, the distance from the line separating the L_o and L_d phases, varies from $-\infty$, deep in the L_d phase, to $+\infty$ in the L_o phase. As an example we'll study the tenary mixture of DOPC/DPPC/Cholesterol. The Gibbs diagram for such mixture (fig. 4.4), obtained from the minimization of $\mathcal{G}(\phi_1, \phi_2, m)$ was discussed in chapter 2; it shows two typical coexistence points A and B connected by a tie-line near the critical point and two coexistence points C and D far from criticality. In our thermodynamic description (eq. 2.33) such points have, for all practical purposes $m = 1$ as discussed before. This simplifies the thermodynamic potential of the ternary mixture that is now reduced to:

$$\begin{aligned}\mathcal{G}(\phi_1, \phi_2, 1) = {} & \phi_1 \ln(\phi_1) + \phi_2 \ln(\phi_2) + \phi_C \ln(\phi_C) \\ & -(\phi_1 + \phi_2) \ln(\phi_1 + \phi_2) \\ & +(\delta^{-1} - \phi_C) \ln(1 - \delta\phi_C) \\ & -\{h_1(T)\phi_1 + h_2(T)\phi_2\} - 2\tilde{J} \\ & +\chi\phi_1\phi_C - \xi(\phi_1 + \phi_2)\phi_C\end{aligned} \tag{4.7}$$

where the free energy is written in unit of $k_B T/S$, with S a molecular lipid area. As explained in the previous section, the relevant energy density for the description of two bulk phases at coexistence is given by the grand potential, which for two composition variables reads

$$\mathcal{G}^{(F)}(\phi_1, \phi_2) = \mathcal{G}(\phi_1, \phi_2, 1) - \phi_1 \mu_{\phi_{1b}} - \phi_2 \mu_{\phi_{2b}} + \Pi_b \tag{4.8}$$

where $\mu_{\phi_{1b}} = \partial\mathcal{G}/\partial\phi_1$ and $\mu_{\phi_{2b}} = \partial\mathcal{G}/\partial\phi_2$ are the chemical potentials conjugated with ϕ_1 and ϕ_2, ϕ_{1b} and ϕ_{2b} are the values of ϕ_1 and ϕ_2 in the respective bulk phases and $\Pi_b = \mu_{\phi_{1b}}\phi_{1b} + \mu_{\phi_{2b}}\phi_{2b} - \mathcal{G}(\phi_{1b}, \phi_{2b}, 1)$ is the osmotic pressure. Extending to two order parameters the previous interface description, we write

$$\mathcal{F} = \frac{k_B T}{S} \int_{-\infty}^{\infty} \left[\frac{l^2}{2} \left(\frac{\mathrm{d}\phi_1}{\mathrm{d}z} \right)^2 + \frac{l^2}{2} \left(\frac{\mathrm{d}\phi_2}{\mathrm{d}z} \right)^2 + \mathcal{G}^{(F)}(\phi_1, \phi_2) \right] \mathrm{d}z \tag{4.9}$$

where l, which has the dimensions of length, measures the penalty for distorsions of the composition profiles. Here, for simplicity, we use the same coefficient l for both gradient terms, but extension into non-equal square gradient coefficients would be straightforward. Notice that comparison between the experimental and the computed phase diagrams fixes all parameters of $\mathcal{G}^{(F)}$. The length l is thus the only unknown parameter in the Landau-Ginzburg functional (4.9). For practical purposes we now express all length in units of l.

In order to find the equilibrium composition profiles, one needs to perform a functional minimization of $\mathcal{F}$ resulting in the associated Euler-Lagrange differential equations:

$$\begin{aligned} \frac{\partial\mathcal{G}^{(F)}}{\partial\phi_1} &= \frac{\mathrm{d}^2\phi_1}{\mathrm{d}z^2} \\ \frac{\partial\mathcal{G}^{(F)}}{\partial\phi_2} &= \frac{\mathrm{d}^2\phi_2}{\mathrm{d}z^2} \end{aligned} \tag{4.10}$$

with

$$\begin{aligned} \frac{\partial\mathcal{G}^{(F)}}{\partial\phi_1} &= -h_1(T) + \ln(\phi_1) - \ln(\phi_C) + \ln(1 - \delta\phi_C) - \ln(\phi_1 + \phi_2) \\ &\quad +\chi\,(1 - 2\phi_1 - \phi_2) - \xi\,(1 - 2\phi_1 - 2\phi_2) - \mu_{\phi_{1b}} \\ \frac{\partial\mathcal{G}^{(F)}}{\partial\phi_2} &= -h_2(T) + \ln(\phi_2) - \ln(\phi_C) + \ln(1 - \delta\phi_C) - \ln(\phi_1 + \phi_2) \\ &\quad +\chi\,\phi_1 - \xi\,(1 - 2\phi_1 - 2\phi_2) - \mu_{\phi_{2b}} \end{aligned} \tag{4.11}$$

We solve numerically the system of differential equations (4.10) by a relaxation method [94] given the boundaries conditions $\phi_1(-\infty) = \phi_{1A}$, $\phi_2(-\infty) = \phi_{2A}$, $\phi_1(+\infty) =$

ϕ_{1B}, $\phi_2(+\infty) = \phi_{2B}$, $d\phi_1/dz|_{-\infty} = d\phi_2/dz|_{-\infty} = d\phi_1/dz|_{+\infty} = d\phi_2/dz|_{+\infty} = 0$ with (ϕ_{1A}, ϕ_{2A}) and (ϕ_{1B}, ϕ_{2B}) the composition of the two coexisting phases A and B - see figure (4.4).

Figure (4.5) shows a contour line representation for the grand potential $\mathcal{G}^{(F)}$. One can draw a mechanical analogy to the minimization of the functional $\mathcal{F}$ and thus to the solution of equations 4.10. In the mechanical analog a particle of coordinates ϕ_1 and ϕ_2 mooves in the potential $-\mathcal{G}^{(F)}$ as a function of the time z. The two equilibrium points A and B which represent the coexisting minima of same height in the grand potential $\mathcal{G}^{(F)}$ correspond to two hill tops in the mechanical potential $-\mathcal{G}^{(F)}$. Finding the profiles $\phi_1(z)$ and $\phi_2(z)$, is thus equivalent to determining the trajectory of a particle that leaves the hill top A with zero velocity and reaches with zero velocity also the hill top B after an infinite time.

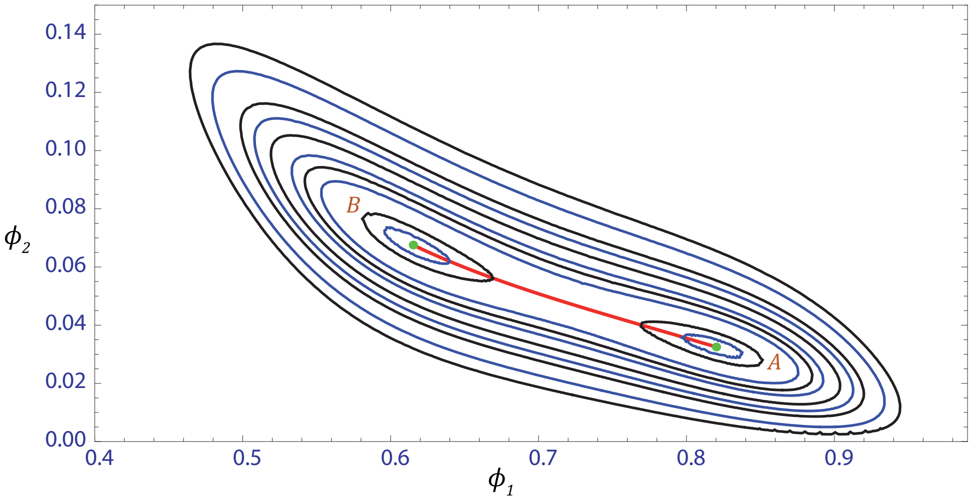

Figure 4.5 – *Contour line representation of* $\mathcal{G}^{(F)}$

In figure (4.6) we display results for the two couples of coexisting points, (A,B) and (C,D) displayed in figure (4.4) with compositions ($\phi_{1A} = 0.792$, $\phi_{2A} = 0.0225$), and ($\phi_{1B} = 0.687$, $\phi_{2B} = 0.0341$) near the critical point and ($\phi_{1C} = 0.820$, $\phi_{2C} = 0.0325$), and ($\phi_{1D} = 0.615$, $\phi_{2D} = 0.0675$) far from the critical point located at ($\phi_{1cr} = 0.769$, $\phi_{2cr} = 0.0083$). The equivalent trajectory representation is shown in figure (4.5) by an continuous line connecting points A and B.

As the figures clearly shows, the width ξ of the interface is similar for profiles ϕ_1 and ϕ_2 and depends on the distance to the critical point. For the composition far from the critical point the interface width is of order the molecular length l and becomes much larger as l as one approaches the critical point. We now investigate how ξ depends on the distance to the critical point.

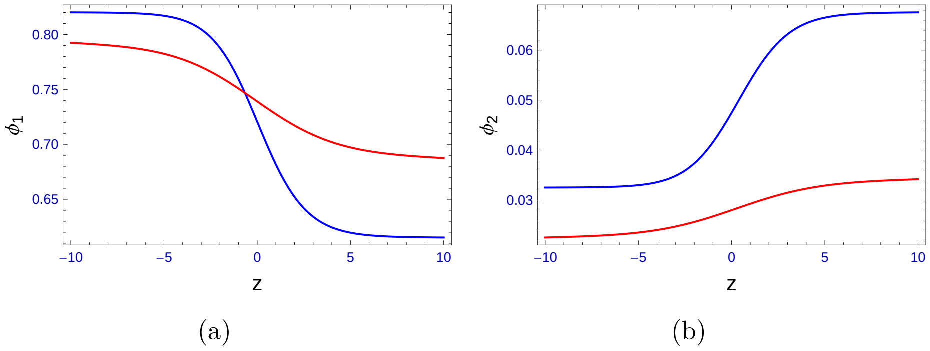

Figure 4.6 — ***(a)*** *Profiles of ϕ_1 near the critical point in red and far from the critical point in blue.* ***(b)*** *Profiles of ϕ_2 near the critical point in red and far from the critical point in blue.*

4.1.4 Interfacial thickness near the critical point

We calculated the composition profiles for conjugated points located on the liquid disordered - liquid ordered bulge. We computed the interfacial thickness from $\xi = \Delta/(2 * \phi'(0))$ where Δ is the length of the tie-line connecting the two coexisting points. Figure (4.7) shows a log-log plot of ξ as a function of Δ revealing the expected scalling behavior $\xi \approx 1/\Delta$ as one approaches the critical point $\Delta \to 0$. The blue line in the Gibbs diagram (4.4) is the locus of the middle points of the tie-lines. If one measures the distance to criticality by the length δ from the tie-lines to the critical point one has $\delta \approx \Delta^2$ and $\xi \approx 1/\delta^{1/2}$.

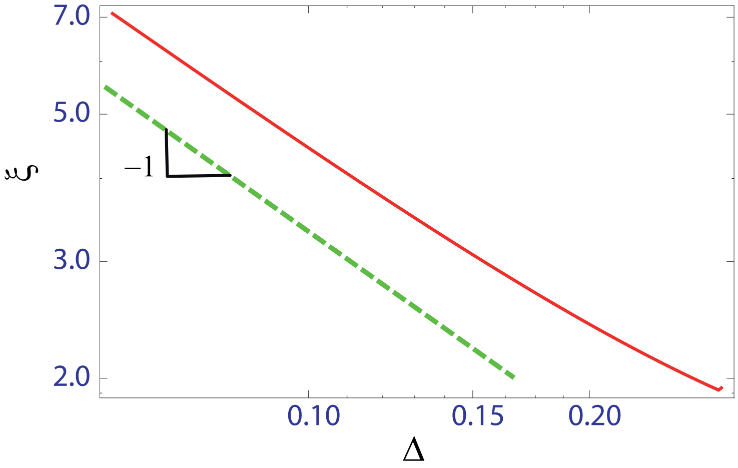

Figure 4.7 — *Log-log representation of ξ as a function of Δ in red. The green line represents a scaling law $\xi \approx \Delta^{-1}$.*

4.1.5 Line tension near the critical point

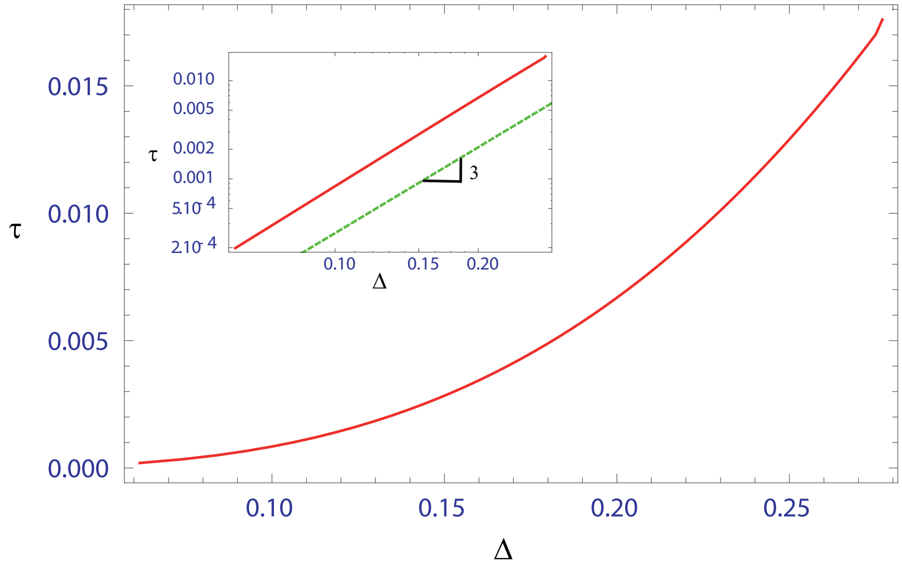

Figure 4.8 – *Line tension as a function of* Δ *in red. The log-log inset shows also the scaling law* $\tau \approx \Delta^3$ *in green.*

We compute the line tension between the liquid ordered and the liquid disordered domains by numerically integrating $\mathcal{F}$ (4.9) with the equilibrium profiles determined above. Figure (4.8) shows the value of τ in units of $k_B T l/S$ as a function of the tie-line length Δ. As the figure and its inset show the line tension obeys the expected scaling behavior $\tau \approx \Delta^3$. Quantitatively one finds $\tau = 0.825\Delta^3$ to better than 1% over the range of Δ values explored here.

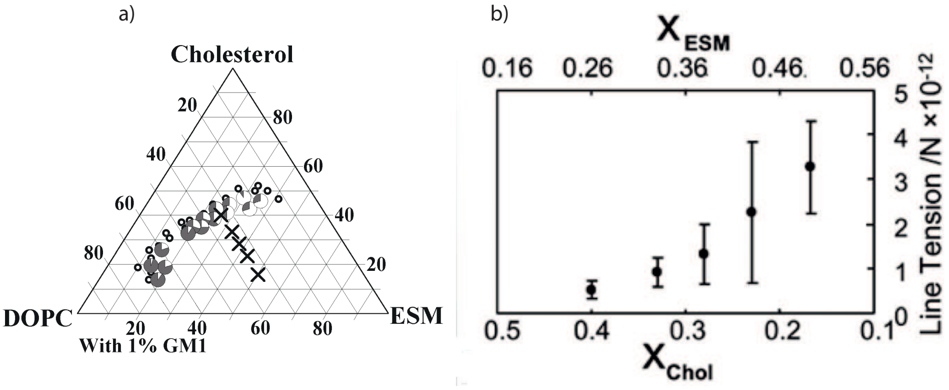

Figure 4.9 – *Measurement of the line tension in the ternary mixture DOPC/ESM/Chol. [91] a) The crosses show the composition for which the line tension was measured at different distances from the critical point. b) Line tension values as a function of the cholesterol and ESM contents.*

Several authors have reported in the litterature line tension values for phase coexisting domains [75, 91, 93]. The most extensive study is reported in [91] for the ternary system DOPC/egg-Sphingomyelin/Cholesterol. The authors study the line tension along a composition line that approaches the critical point by roughly following the midpoint of the tie-lines in figure (4.9 a). They show that the line tension vanishes at the critical point as shown in figure (4.9 b). We now attempt a comparison between our theoretical prediction and these experimental results. Let's first notice that our ternary phase diagram shown in figure 4.4 was computed for the ternary lipid system DOPC/DPPC/Cholesterol. However, the two ternary systems DOPC/egg-Sphingomyelin/Cholesterol and DOPC/DPPC/Cholesterol display similar experimental diagrams [68, 87] both with respect to coexistence domain shapes and sizes, and to the position of the critical point. Because the experimental data in [91] does not provide from an easy determination of the tie-lines length, we measure the distance to the critical point by δ the length on the Gibbs diagram between the sample composition and the composition of the critical point.

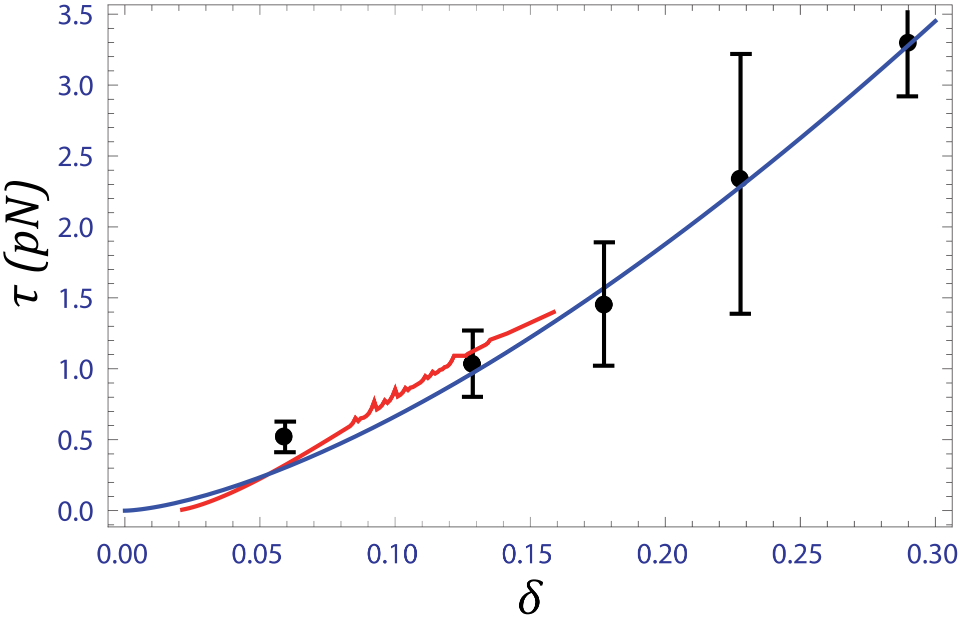

Figure 4.10 — *Comparison between theory and experiments for the line tension. δ is the distance between the critical point and the tie-line. Experimental points from [91]. The red line represents predictions from our theoretical model with $S = 0.6$ nm^2 and $l = 5$ nm. The blue line is the power law $\tau = 21 \cdot \delta^{3/2}$ pN.*

Experimental points from [91] as a function of δ are displayed in figure (4.10) that shows also theoretical predictions from our model as a red line. The theoretical values were rescaled by assuming $S = 0.6$ nm^2 and choosing the square gradient prefactor $l = 5$ nm. The mean field prediction for the line tension as a function of δ is also plotted in the figure 4.10, with the best fit value $\tau = 21 \cdot \delta^{3/2}$ pN. Our theoretical results are thus in very good aggreement with experiments. The law describing how the line tension vanishes as it approaches the critical point follows the mean field prediction in the composition range covered by experiments. Remarkably, all experimental points can be understood by the single parameter l, the macroscopic length associated with the square gradient term. The value of l that better fits the experiment is of order of the bilayer thickness. The linear interface separating two lipid domains has thus a thickness of the order of a few lipid diameters.

4.2 Effect of inclusions on local composition

4.2.1 Introduction

In bilayers of biological relevance proteins play a crucial role for controlling membrane function. Within the context of lipid phase separation it has been suggested that proteins [95, 96] actively change the membrane local composition by recruiting lipids to the protein vicinity. Such phenomena, akin to wetting, can be theoretically studied within the Landau-Ginzburg formalism introduced in the previous section. In the following we investigate the lipid recruitment efficiency of proteins as a function of protein size by mimicking the protein as solid membrane inclusions. The inclusions are inserted in the homogeneous liquid disordered phase in the vicinity of the boundary of the coexistence domain as shown in figure (4.11). The inclusion exhibits a repulsion for unsaturated lipids and an attraction for the saturated ones, a typical behaviour for proteins that are expected, in biological membranes, to play a role in raft formation. In the first paragraph we consider large enough inclusions, such that the inclusion lipid interface can be considered as flat for all practical purposes. This will allow us to setup the proper theoretical environment for studying wetting in systems described with two order parameters. In the second paragraph we consider circular inclusions of finite radii [97, 98] and study wetting as a function of inclusion size.

4.2.2 Wetting of a large inclusion by a liquid ordered phase

In this paragraph we extend the Landau-Ginzburg formalism introduced above to account for interactions between the lipid phases and the inclusion and write:

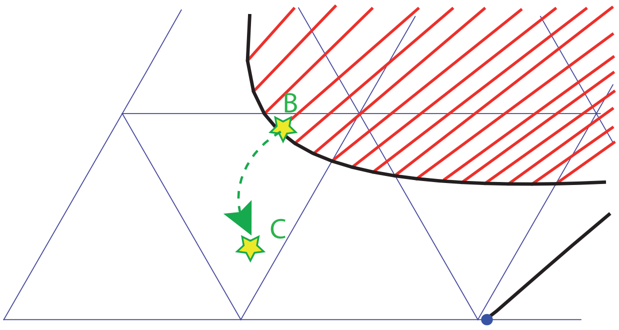

Figure 4.11 – *C is a point in the homogeneous phase in the vicinity of B the initially coexistence point.*

$$\mathcal{F}_W = E_S(\phi_{1_S},\phi_{2_S}) + \int_0^\infty \left[\frac{l^2}{2}\left(\frac{\mathrm{d}\phi_1}{\mathrm{d}z}\right)^2 + \frac{l^2}{2}\left(\frac{\mathrm{d}\phi_2}{\mathrm{d}z}\right)^2 + \mathcal{G}^{(F)}(\phi_1,\phi_2)\right]\mathrm{d}z \tag{4.12}$$

with

$$\begin{aligned} E_S(\phi_{1_S},\phi_{2_S}) = &\left[h_{\phi_1}\phi_{1_S}^2 - \gamma_{\phi_1}.\phi_{1_S} + h_{\phi_2}\phi_{2_S}^2 - \gamma_{\phi_2}.\phi_{2_S}\right] \\ &-\left[h_{\phi_1}\phi_{1_\infty}^2 - \gamma_{\phi_1}.\phi_{1_\infty} + h_{\phi_2}\phi_{2_\infty}^2 - \gamma_{\phi_2}.\phi_{2_\infty}\right] \end{aligned} \tag{4.13}$$

a line energy contribution accounting for interactions between the unsaturated lipids ϕ_1 and the saturated lipids ϕ_2 with the inclusion. Line energies γ_{ϕ_1}, and γ_{ϕ_2} represent the energy gain ($\gamma_{\phi_1},\gamma_{\phi_2} > 0$) or loss ($\gamma_{\phi_1},\gamma_{\phi_2} < 0$) of moving lipids from the bulk phase to the inclusion interface. Fields associated with the quadratic terms h_{ϕ_1} and h_{ϕ_2} represent the changes of lipid-lipid interactions at the interface. The role of these fields has been extensively studied in the context of the wetting theory for systems described with one order parameter as briefly reviewed in chapter(1),section (1.6). Subtraction of the second term of the right hand side of equation 4.13 allows $\mathcal{F}_W$ to measure only the energy cost of distorsion of the composition profiles.

Equilibrium profiles are obtained by minimization of the functional density $\mathcal{F}_W$ with respect to $\phi_1, \phi_2, \phi_{1_S}, \phi_{2_S}$ resulting in the Euler-Lagrange system of equations (4.10) with the associated boundary conditions.

$$\begin{aligned} \frac{\mathrm{d}\phi_{1_S}}{\mathrm{d}z} &= 2h_{\phi_1}\phi_{1_S} - \gamma_{\phi_1} \\ \frac{\mathrm{d}\phi_{2_S}}{\mathrm{d}z} &= 2h_{\phi_2}\phi_{2_S} - \gamma_{\phi_2} \end{aligned} \tag{4.14}$$

Notice that boundary conditions 4.14 provide two equations for determining the values of the profiles and of their gradients at the interface. They are therefore an infinity of surface fields that induces the same composition profile. As in the previous section we solve the system of differential equations (4.10) with boundary conditions 4.14 by numerical relaxation methods [94]. Figure (4.12) shows the contour line representation of the energy landscape of the energy $\mathcal{G}^{(F)}$. Contrary to the case of phase coexistence the two minima of the energy are not here at the same heigth as further represented in the 3D plot of figure (4.13). A mechanical analogy can still be drawn. One needs to find the trajectory of a particle in a two dimensionnal system of coordinates ϕ_1 and ϕ_2 as a function of time z. The particle leaves from a level below the hill top heigth C with finite velocity components $d\phi_1/dz|_{z=0}$ and $d\phi_2/dz|_{z=0}$ finishing its course at point C with vanishing velocity after an infinite time. When the particle trajectory passes trough the meta-stable minimum of the free energy, it slows down leading to profiles of liquid ordered enrichment close to the interface.

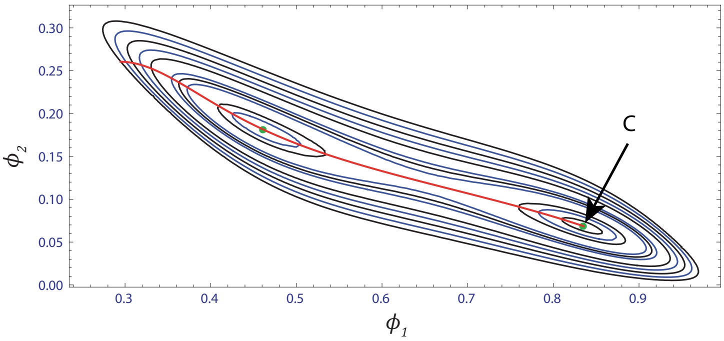

Figure 4.12 – *Contour line of the energy landscape* $\mathcal{G}^{(F)}$.

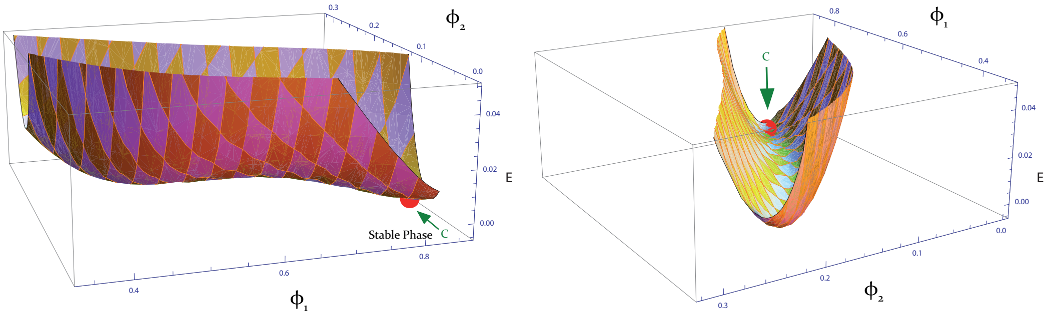

(a) (b)

Figure 4.13 – *(a) Landscape of energy seen in profile view along the* ϕ_1 *axis with the stable phase at the right(red point). (b) Landscape of energy seen in front view.*

When the particle trajectory does not explore the meta-stable minimum, one gets much less enrichment of the interface by the liquid ordered phase.

We computed profiles for the homogeneous liquid disordered phase C of composition ${\phi_1}_C$=0.835, ${\phi_2}_C$=0.0685 and surface field values γ_{ϕ_1}=0.3, h_{ϕ_1}= 0.0025, γ_{ϕ_2}= -0.001, h_{ϕ_2} = 0.5.10^{-5}. Notice that the interface strongly repels the unsaturated lipids and slightly attracts the saturated one. Results are plotted in figure (4.14). The figure displays two equally valid solutions of the differential equations with corresponding boundaries conditions. As expected the profiles of the unsaturated lipids display low values at the interface while those of the saturated lipids present higher values. However unsaturated lipid decrease is larger than saturated lipid increase which implies the enrichment of the inclusion interface by cholesterol ($\phi_{ch} = 1 - \phi_1 - \phi_2$). Note the choice of γ_{ϕ_1}, h_{ϕ_1}, γ_{ϕ_2}, h_{ϕ_2} is not unique. There is an infinity of pairs (h, γ) associated with a given value of the surface fields, ${\phi_1}_S$ and ${\phi_2}_S$.

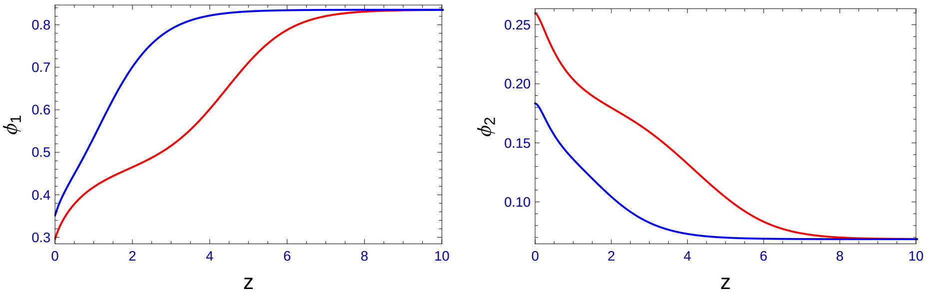

(a) ϕ_1 profile.

(b) ϕ_2 profile.

Figure 4.14 – *Equilibrium profiles for the interfacial behaviour of a liquid disordered phase of composition* ${\phi_1}_C$*=0.835,* ${\phi_2}_C$*=0.0685 that interacts with an inclusion interface with surface fields* γ_{ϕ_1}*=0.3,* h_{ϕ_1}*= 0.0025,* γ_{ϕ_2}*= -0.001,* h_{ϕ_2} = 0.5.10^{-5}*. This corresponds to an inteface that stronger repels the unsaturated lipids* ϕ_1 *and attracts the saturated lipid* ϕ_2*. Red and blue profiles correspond respectively to pre-wetting and partial wetting solutions-see text for a full discussion.*

The solutions in blue decay exponentially fast to the bulk value, they correspond to a local enrichment with a limited extent. The red solutions display instead thicker profiles that reveal pre-wetting behaviour of the inclusion by the liquid ordered phase. For systems with one order parameter only, the existence of a first integral of the movement in the analog mechanical problem allows for the so-called Cahn construction, a graphical representation that allows to distinguish the absolute stability of the different solutions. For systems with two order parameters such as ours there exists no Cahn construction and the stability analysis needs to be performed by the numerical evaluation of the energy $\mathcal{F}_W$. We will perform such analysis in the next section and show that for the surface field values of figure 4.14

the red solution is the stable one.

4.2.3 Effect of inclusion size on the wetting properties

In the previous section we have shown that exposure of the inclusion interface to an homogeneous phase of the ternary lipid membrane results in a build up of an interfacial inhomogeneous profile that extends over a lenght ξ. For relevant inclusion of a finite size that we model by circular interfaces of radius R we expect significant effects when R becomes similar or equal to ξ. The composition profile can be computed by minimization of functional density:

$$\mathcal{F}_W = E_S(\phi_{1_S}, \phi_{2_S}) + \int_R^\infty \left[\frac{l^2}{2} \left(\frac{\mathrm{d}\phi_1}{\mathrm{d}z} \right)^2 + \frac{l^2}{2} \left(\frac{\mathrm{d}\phi_2}{\mathrm{d}z} \right)^2 + \mathcal{G}^{(F)}(\phi_1, \phi_2) \right] 2\pi r dr \quad (4.15)$$

with:

$$\begin{aligned} E_S(\phi_{1_S}, \phi_{2_S}) = {} & 2\pi r \left[h_{\phi_1} \phi_{1_S}^2 - \gamma_{\phi_1} . \phi_{1_S} + h_{\phi_2} \phi_{2_S}^2 - \gamma_{\phi_2} . \phi_{2_S} \right] \\ & - 2\pi r \left[h_{\phi_1} \phi_{1_\infty}^2 - \gamma_{\phi_1} . \phi_{1_\infty} + h_{\phi_2} \phi_{2_\infty}^2 - \gamma_{\phi_2} . \phi_{2_\infty} \right] \end{aligned} \quad (4.16)$$

The energy functional $\mathcal{F}_W$ and its surface field components E_S have the same structure as those of the flat interface 4.10 but have been adapted to the cylindrical coordinates system. Minimization with respect to $\phi_1, \phi_2, \phi_{1_S}, \phi_{2_S}$ – see Appendix C – results in the Euler-Lagrange system of equations (4.17) with the associated boundary conditions that can be written as in equation (4.14).

$$\begin{aligned} \frac{\partial \mathcal{G}^{(F)}}{\partial \phi_1} &= \frac{\mathrm{d}^2 \phi_1}{\mathrm{d}r^2} + \frac{1}{r} \frac{\mathrm{d}\phi_1}{\mathrm{d}r} \\ \frac{\partial \mathcal{G}^{(F)}}{\partial \phi_2} &= \frac{\mathrm{d}^2 \phi_2}{\mathrm{d}r^2} + \frac{1}{r} \frac{\mathrm{d}\phi_2}{\mathrm{d}r} \end{aligned} \quad (4.17)$$

We plotted equilibrium profiles for two values of the radius of the inclusion in figures (4.15, 4.16) for field values γ_{ϕ_1}=0.3, h_{ϕ_1}= 0.0025, γ_{ϕ_2}= -0.001, h_{ϕ_2} = $0.5.10^{-5}$. As the figures show, for the same values of the surface fields, one obtains different composition profiles for different values of the inclusion radius. The thickness of the interfacial profile decreases as the radius is reduced. The pre-wetting line is therefore a function of particle radius. In practice, this implies that no significant recruitment of lipids can occur close to a protein with radius much smaller that the typical thickness of the wetting layer. This is quantitatively shown in figure (4.17)

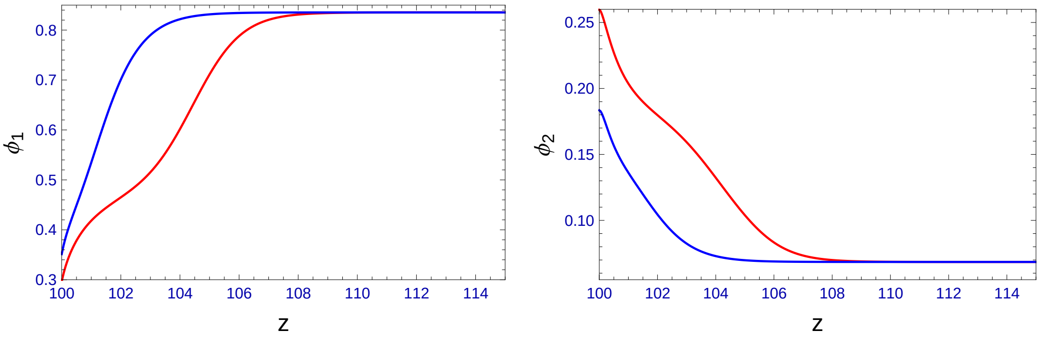

(a) ϕ_1 profile. (b) ϕ_2 profile.

Figure 4.15 – *Circular inclusion profiles with* $\boldsymbol{R}$*=100.*

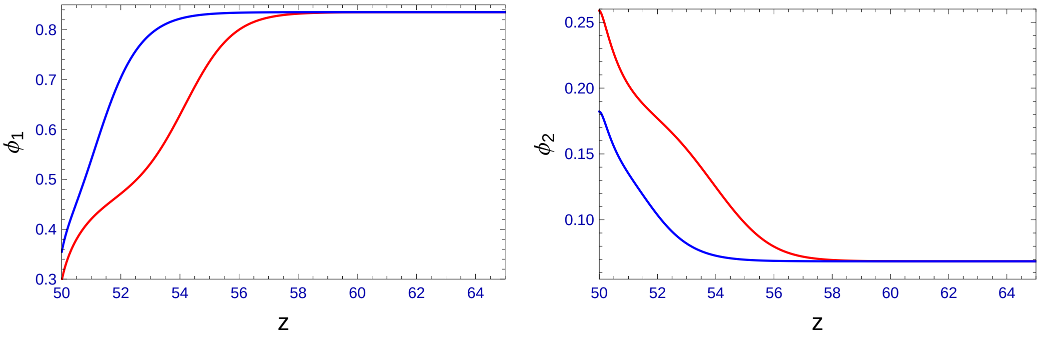

(a) ϕ_1 profile. (b) ϕ_2 profile.

Figure 4.16 – *Circular inclusion profiles with* $\boldsymbol{R}$*=50.*

where we plot the value of the interfacial thickness ξ as a function of radius. ξ is defined here for the wetting layer as the distance between the wall and the inflexion point of the composition profile. As the figure shows, the inflexion point vanishes for $R < 1.8$. This can be qualitatively understood by the balance between energy gain by contact with the interface and the penalty for distortion of the profiles in the wetting layer. As the radius is reduced, the gain of interfacial energy decreases also, eventually being too small to compensate for profile distortion.

As explained above, two solution families obey the Euler-Lagrange equations. They correspond to a partial wetting profile, characterized by an exponential relaxation decay and to a complete wetting profile. The relative stability of the two solutions can be determined by numerically integrating the total energy $\mathcal{F}_W$. We can observe on figure (4.18) the energy values for the two solutions as a function of inclusion radius. As the figure shows, for these values of surface fields that correspond to those of figures (4.15, 4.16) the wetting profile has always the lower energy,

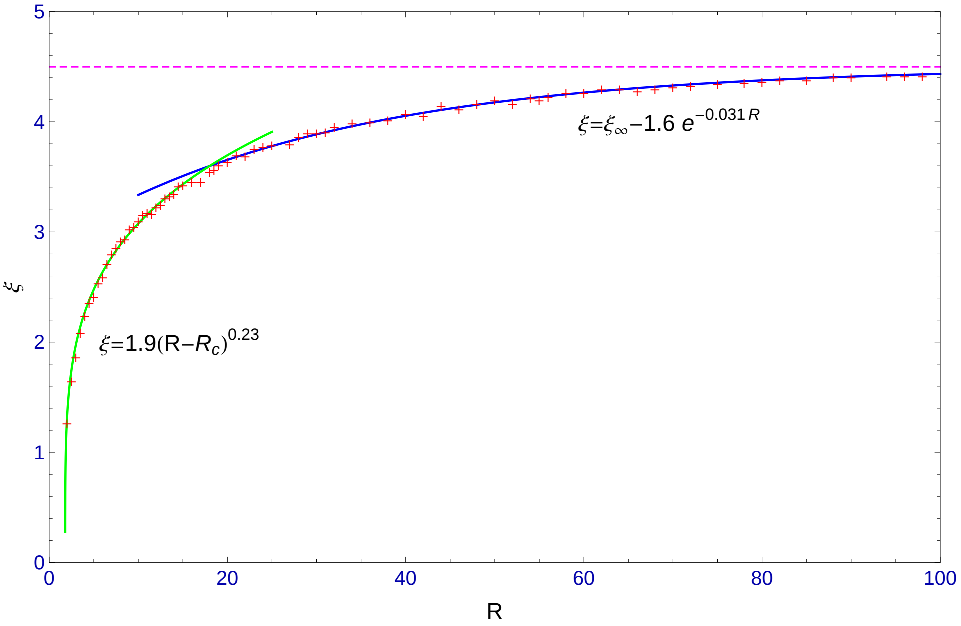

Figure 4.17 – *Width ξ of the pre-wetting with respect to the inclusion radius R. The dashed magenta line represents ξ_∞ the value of ξ for the large inclusion.*

even though it becomes coincident with the second solution for radii smaller than $R = 16$.

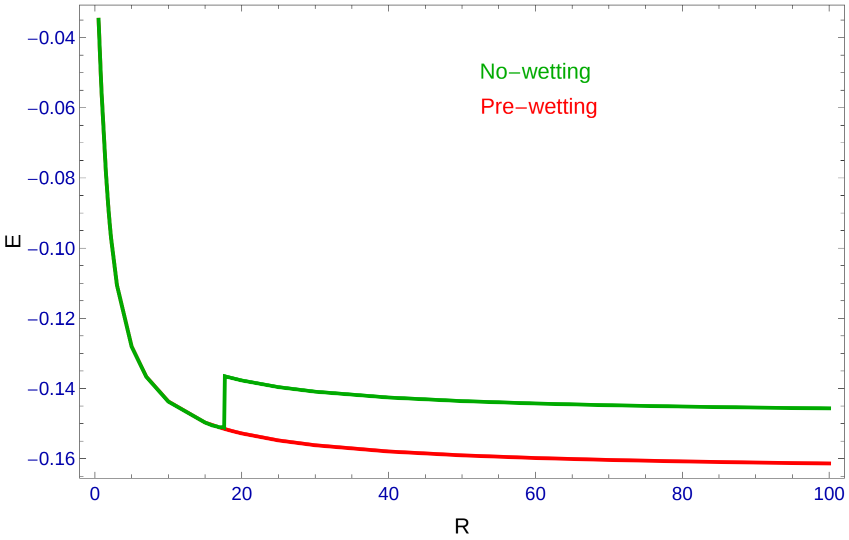

Figure 4.18 – *Total energy for each solutions with respect to the radius.*

Our results are summarised in the Gibbs diagram (4.19) where we represent the pre-wetting horn for R=25, other lines could be drawn for different values of the radius. This line separates the stable phase in two regions. All points which are localized between the horn and the coexistence line give a pre-wetting solution, while points localised further away do not display pre-wetting.

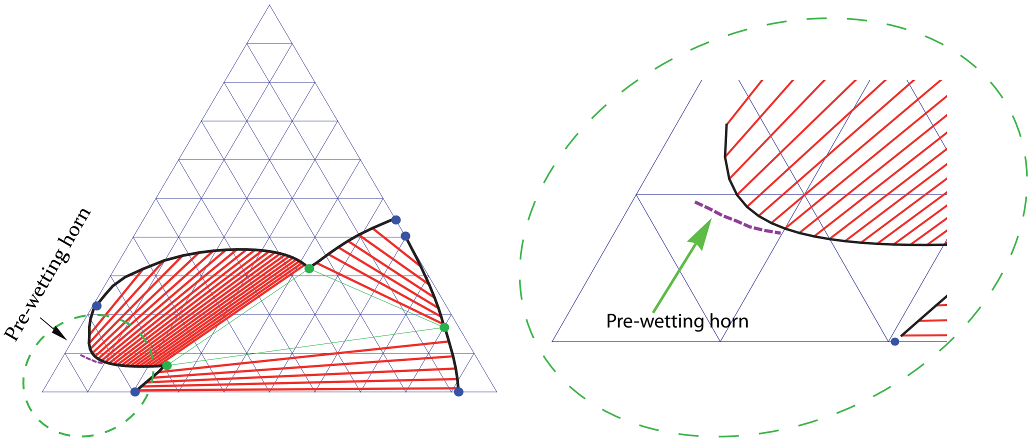

(a) Pre-wetting horn in the Gibbs triangle. (b) Zoomed zone from the left triangle.

Figure 4.19 – *Pre-wetting horn for R=25.*

Conclusion

In this work we presented a simple and predictive model for the thermodynamics of binary and ternary lipid mixtures containing cholesterol. This model makes an intensive use of an internal order parameter discriminating between thegel and the fluid phases. I ended up with a model with essentially a single free parameter χ, the other parameters being strongly constrained by the known thermodynamic properties of the system.

The determination of the ternary phase coexistence regions required a special numerical approach, which turned out to be efficient, accurate and applicable to a wide class of thermodynamic approaches with order parameter. We compared our calorimetry with DSC experiments, with good qualitative agreement. We investigated a number of other ternary lipid mixtures, which could all be reproduced. We made a first step towards including the effect of a change in the lipid specific areas, by extending to binary lipid mixtures the Flory-Huggins approach. This improved the agreement with experimental results.

I extended the model to describe inhomogeneous phase profiles by introducing a Landau-Ginzburg functional. I derived the concentration profile across a liquid ordered-liquid disordered boundary within the framework of this model, and obtained a value for the associated line tension. I then investigated various wetting profiles around circular inclusions, and showed the possibility of having a swollen liquid ordered domain around the inclusions even though the liquid disordered phase remains thermodynamically favorable. These calculations are relevant for the scenario consisting in creating rafts by a local nucleation of the liquid ordered phase around the participating proteins.

List of Figures

List of Tables

Appendix

Appendix A

Spinodal calculation

The spinodal line corresponds to a singular Hessian matrix.

$$\det(\mathcal{H}_{\mathcal{G}}) = 0. \tag{A.1}$$

with:

$$\mathcal{H}_{\mathcal{G}} = \begin{pmatrix} \dfrac{\partial^2 \mathcal{G}}{\partial \phi^2} & \dfrac{\partial^2 \mathcal{G}}{\partial \phi \partial m} \\ \dfrac{\partial^2 \mathcal{G}}{\partial \phi \partial m} & \dfrac{\partial^2 \mathcal{G}}{\partial m^2} \end{pmatrix} \tag{A.2}$$

We start from the derivatives of the free energy:

$$\begin{aligned} \frac{\partial \mathcal{G}}{\partial \phi} &= -h^{(1)} m + h^{(2)} m + \ln(\phi) - \ln(1-\phi) \\ \frac{\partial^2 \mathcal{G}}{\partial \phi^2} &= \frac{1}{\phi} + \frac{1}{1-\phi} \end{aligned} \tag{A.3}$$

$$\frac{\partial \mathcal{G}}{\partial m} = -h^{(1)}\phi - h^{(2)}(1-\phi) - 4Jm + \frac{1}{2}\ln\left(\frac{1+m}{2}\right) - \frac{1}{2}\ln\left(\frac{1-m}{2}\right)$$

$$\frac{\partial^2 \mathcal{G}}{\partial m^2} = -4J + \frac{1}{2(1+m)} + \frac{1}{2(1-m)}$$

$$\frac{\partial^2 \mathcal{G}}{\partial m \partial \phi} = -h^{(1)} + h^{(2)} \tag{A.4}$$

We obtain:

$$\left[\frac{1}{\phi} + \frac{1}{1-\phi}\right]\left[-4J + \frac{1}{2(1+m)} + \frac{1}{2(1-m)}\right] - \alpha^2 = 0 \tag{A.5}$$

with $\alpha = h^{(1)} - h^{(2)}$, and finally find the spinodal equation:

$$\phi(1-\phi) = \frac{1-4J(1-m^2)}{\alpha^2(1-m^2)} \tag{A.6}$$

Appendix B

Functional minimization

We perform the variation of the energy functional with respect to ϕ (with $\alpha = 1$):

$$I(\phi(z)) = E_S(\phi_S) + \int_0^\infty \left[V(\phi) + \frac{\alpha}{2}\left(\frac{\mathrm{d}\phi(z)}{\mathrm{d}z}\right)^2 \right] \mathrm{d}z \tag{B.1}$$

with: $E_S(\phi_S) = 1/2h\phi_S^2 - \gamma\phi_S$.

It gives:

$$\delta I(\phi(z)) = \delta\phi_S \frac{\mathrm{d}E_S(\phi_S)}{\mathrm{d}\phi_S} + \delta\phi \int_0^\infty \left[\frac{\mathrm{d}V}{\mathrm{d}\phi} - \frac{\mathrm{d}^2\phi(z)}{\mathrm{d}z^2} \right] \mathrm{d}z + \left[\frac{\mathrm{d}\phi}{\mathrm{d}z}\delta\phi \right]_0^\infty \tag{B.2}$$

The integral term gives the equation for the bulk,

$$\frac{\mathrm{d}V}{\mathrm{d}\phi} = \alpha \frac{\mathrm{d}^2\phi}{\mathrm{d}z^2}, \tag{B.3}$$

while the boundary contribution corresponds to a surface field equation (with $\delta\phi(\infty) = 0$):

$$2h\phi - \gamma = \frac{\mathrm{d}\phi}{\mathrm{d}z} \tag{B.4}$$

Appendix C

Functional minimization in polar coordinates

We perform the variation of the energy functional in the case of a circular inclusion for a binary system parameterized with polar coordinates.

$$I(\phi(r)) = E_S(\phi_S) + \int_R^\infty \left[\mathcal{G}^{(F)}(\phi) + \frac{1}{2}\left(\frac{\mathrm{d}\phi(r)}{\mathrm{d}r}\right)^2\right] 2\pi r \mathrm{d}r \tag{C.1}$$

We first obtain:

$$\delta I(\phi(r)) = \delta\phi_S \frac{\mathrm{d}E_S(\phi_S)}{\mathrm{d}\phi_S} + \int_R^\infty \left[\frac{\delta\mathcal{G}^{(F)}(\phi)}{\delta\phi}\delta\phi + \left[\frac{\mathrm{d}\phi(r)}{\mathrm{d}r}\frac{\mathrm{d}\delta\phi(r)}{\mathrm{d}r}\right]\right] 2\pi r \mathrm{d}r \tag{C.2}$$

After developing:

$$\delta I(\phi(r)) = \delta\phi_S \frac{\mathrm{d}E_S(\phi_S)}{\mathrm{d}\phi_S} + \left[r\frac{\mathrm{d}\phi}{\mathrm{d}r}\delta\phi\right]_R^\infty 2\pi + \int_R^\infty \left[\frac{\mathrm{d}\mathcal{G}^{(F)}(\phi)}{\mathrm{d}\phi}r - \left[\frac{\mathrm{d}\phi(r)}{\mathrm{d}r} + r\frac{\mathrm{d}^2\phi}{\mathrm{d}r^2}\right]\right]\delta\phi(r) 2\pi \mathrm{d}r \tag{C.3}$$

The equation for the bulk component reads:

$$\frac{\mathrm{d}\mathcal{G}^{(F)}(\phi)}{\mathrm{d}\phi} = \frac{1}{r}\frac{\mathrm{d}\phi(r)}{\mathrm{d}r} + \frac{\mathrm{d}^2\phi}{\mathrm{d}r^2}, \tag{C.4}$$

and the surface field condition, with $\delta\phi(\infty) = 0$ and $\delta\phi_S = \delta\phi(R)$ becomes:

$$\frac{\mathrm{d}E_S(\phi_S)}{\mathrm{d}\phi_S} - \frac{\mathrm{d}\phi(R)}{\mathrm{d}r} 2\pi R = 0, \tag{C.5}$$

which reduces to:

$$\frac{\mathrm{d}\phi(R)}{\mathrm{d}r} = 2h\phi - \gamma, \tag{C.6}$$

if one takes $E_S(\phi_S) = (h\phi^2 - \gamma\phi)2\pi R$

Appendix D

Heat capacity relations

The total enthalpy of a biphasic mixture for a specific ϕ_0 is given by:

$$H(T,\phi_0) = \eta \cdot H(T,\phi_1,m) + (1-\eta) \cdot H(T,\phi_2,m') \tag{D.1}$$

The heat capacity is defined as the constant pressure derivative of the enthalpy with respect to temperature:

$$C_P = \frac{\mathrm{d}\eta}{\mathrm{d}T} \cdot [H(T,\phi_1,m) - H(T,\phi_2,m')] + \eta \cdot \frac{\mathrm{d}H(T,\phi_1,m)}{\mathrm{d}T} + (1-\eta) \cdot \frac{\mathrm{d}H(T,\phi_2,m')}{\mathrm{d}T} \tag{D.2}$$

It is essential to note that ϕ_1, ϕ_2 and m depend on temperature along the two lines of coexistence, and this leads to:

$$\frac{\mathrm{d}H(T,\phi_i(T),m(T))}{\mathrm{d}T} = \frac{\partial H}{\partial T} + \frac{\partial H}{\partial \phi_i} \cdot \frac{\partial \phi_i}{\partial T} + \frac{\partial H}{\partial m} \cdot \frac{\partial m}{\partial T} \tag{D.3}$$

The m derivative do not contribute because of the minimization condition which defines m^*:

$$\frac{\partial H}{\partial m} = \frac{\partial}{\partial m} \cdot \frac{\partial \beta \mathcal{G}}{\partial \beta} = \frac{\partial}{\partial \beta} \cdot \frac{\partial \beta \mathcal{G}}{\partial m} = 0 \tag{D.4}$$

Thus,

$$C_p = \frac{\mathrm{d}\eta}{\mathrm{d}T} [H(T,\phi_1,m) - H(T,\phi_2,m')] + \eta \left[\frac{\partial H(T,\phi_1,m)}{\partial T} + \frac{\partial H(T,\phi_1,m)}{\partial \phi_1} \cdot \frac{\partial \phi_1}{\partial T} \right]$$
$$+(1-\eta) \left[\frac{\partial H(T,\phi_2,m')}{\partial T} + \frac{\partial H(T,\phi_2,m')}{\partial \phi_2} \cdot \frac{\partial \phi_2}{\partial T} \right] \tag{D.5}$$

We set N_t, the Avogadro number and obtain the enthalpy of the homogeneous phase:

$$H(T,\phi_i,m) = \frac{d(\beta G(\phi_i))}{d\beta} = N_t \cdot T^2 \cdot m(\phi_i) \cdot \left[\phi_i \frac{(\Delta S)_1}{2T_{M_1}} + (1-\phi_i)\frac{(\Delta S)_2}{2T_{M_2}}\right]. \tag{D.6}$$

The variation of the fraction η is obtained by differentiating the lever rule

$$\eta(T) = \frac{\phi_0 - \phi_2(T)}{\phi_1(T) - \phi_2(T)} \tag{D.7}$$

giving:

$$\frac{d\eta}{dT} = \frac{\frac{d\phi_1}{dT}(\phi_2 - \phi_0) + \frac{d\phi_2}{dT}(\phi_0 - \phi_1)}{(\phi_2 - \phi_1)^2} \tag{D.8}$$

The derivatives of the enthalpy in the homogeneous bulk phase are :

$$\frac{\partial H}{\partial \phi_i} = N_t \cdot T^2 \cdot m(\phi_i) \cdot \left[\frac{(\Delta S)_1}{2T_{M_1}} - \frac{(\Delta S)_2}{2T_{M_2}}\right] \tag{D.9}$$

Altogether:

$$\begin{aligned}\frac{\partial H}{\partial T} &= \frac{-1}{kT^2}\frac{d^2(\beta G(\phi_i))}{d\beta^2} \\ &= N_t \cdot \left[\frac{dm}{dT}(\phi_i) \cdot T^2 \left(\phi_i \frac{(\Delta S)_1}{2T_{M_1}} + (1-\phi_i)\frac{(\Delta S)_2}{2T_{M_2}}\right) + 2m(\phi_i) \cdot T \left(\phi_i \frac{(\Delta S)_1}{2T_{M_1}} + (1-\phi_i)\frac{(\Delta S)_2}{2T_{M_2}}\right)\right]\end{aligned} \tag{D.10}$$

where the slope dm/dT comes from the differentiation of equation (2.12):

$$\frac{dm}{dT}(\phi_i) = \frac{\phi_i \frac{dh^{(1)}}{dT} + (1-\phi_i)\frac{dh^{(2)}}{dT}}{\frac{1}{1-m(\phi_i)^2} - 4J} \tag{D.11}$$

Appendix E

Derivatives of $\mathcal{G}$

E.1 Generalized derivatives of $\mathcal{G}$

We list below the generalized derivatives in term of the partial derivatives of $\mathcal{G}(\phi_1, \phi_2, m)$.

$$\begin{aligned}
D_{\phi_1}\mathcal{G} &= \partial_{\phi_1}\mathcal{G} \\
D_{\phi_2}\mathcal{G} &= \partial_{\phi_2}\mathcal{G} \\
D^2_{\phi_1\phi_1}\mathcal{G} &= \partial^2_{\phi_1\phi_1}\mathcal{G} - \frac{(\partial^2_{m\phi_1}\mathcal{G})^2}{\partial^2_{mm}\mathcal{G}} \\
D^2_{\phi_2\phi_2}\mathcal{G} &= \partial^2_{\phi_2\phi_2}\mathcal{G} - \frac{(\partial^2_{m\phi_2}\mathcal{G})^2}{\partial^2_{mm}\mathcal{G}} \\
D^2_{\phi_1\phi_2}\mathcal{G} &= \partial^2_{\phi_1\phi_2}\mathcal{G} - \frac{\partial^2_{m\phi_1}\mathcal{G} \times \partial^2_{m\phi_2}\mathcal{G}}{\partial^2_{mm}\mathcal{G}} \\
D^3_{\phi_1\phi_1\phi_1}\mathcal{G} &= -3\frac{\partial^3_{\phi_1\phi_1 m}\mathcal{G} \times \partial^2_{\phi_1 m}\mathcal{G}}{\partial^2_{mm}\mathcal{G}} - \partial^3_{mmm}\mathcal{G} \times \frac{(\partial^2_{\phi_1 m} g)^3}{(\partial^2_{mm}\mathcal{G})^3} + \partial^3_{\phi_1\phi_1\phi_1}\mathcal{G} \\
&\quad +3\,\partial^3_{\phi_1 mm}\mathcal{G} \times \left(\frac{\partial^2_{\phi_1 m}\mathcal{G}}{\partial^2_{mm}\mathcal{G}}\right)^2 \\
D^3_{\phi_2\phi_2\phi_2}\mathcal{G} &= -3\frac{\partial^3_{\phi_2\phi_2 m}\mathcal{G} \times \partial^2_{\phi_2 m}\mathcal{G}}{\partial^2_{mm}\mathcal{G}} - \partial^3_{mmm}\mathcal{G} \times \frac{(\partial^2_{\phi_2 m}\mathcal{G})^3}{(\partial^2_{mm}\mathcal{G})^3} + \partial^3_{\phi_2\phi_2\phi_2}\mathcal{G} \\
&\quad +3\,\partial^3_{\phi_2 mm}\mathcal{G} \times \left(\frac{\partial^2_{\phi_2 m}\mathcal{G}}{\partial^2_{mm}\mathcal{G}}\right)^2
\end{aligned}$$

$$\begin{aligned}
D^3_{\phi_1\phi_1\phi_2}\mathcal{G} &= -2\frac{\partial^3_{\phi_1\phi_2 m}\mathcal{G}\times\partial^2_{\phi_1 m}\mathcal{G}}{\partial^2_{mm}\mathcal{G}} + \partial^3_{\phi_1\phi_2\phi_2}\mathcal{G} - \frac{\partial^2_{m\phi_2}\mathcal{G}}{\partial^2_{mm}\mathcal{G}}(\partial^3_{\phi_1\phi_1 m}\mathcal{G} + \frac{(\partial_{\phi_1 m}\mathcal{G})^2\times\partial^3_{mmm}\mathcal{G}}{(\partial^2_{mm}\mathcal{G})^2}) \\
&+2\frac{\partial^3_{\phi_1 mm}\mathcal{G}\times\partial^2_{\phi_1 m}\mathcal{G}\times\partial^2_{\phi_2 m}\mathcal{G}}{(\partial^2_{mm}\mathcal{G})^2} + \frac{\partial^3_{\phi_2 mm}\mathcal{G}\times(\partial^2_{\phi_1 m}\mathcal{G})^2}{(\partial^2_{mm}\mathcal{G})^2} \\
D^3_{\phi_1\phi_2\phi_2}\mathcal{G} &= -2\frac{\partial^3_{\phi_1\phi_2 m}\mathcal{G}\times\partial^2_{\phi_2 m}\mathcal{G}}{\partial^2_{mm}\mathcal{G}} + \partial^3_{\phi_1\phi_2\phi_2}\mathcal{G} - \frac{\partial^2_{m\phi_1}\mathcal{G}}{\partial^2_{mm}\mathcal{G}}(\partial^3_{\phi_2\phi_2 m}\mathcal{G} + \frac{(\partial^2_{\phi_2 m}\mathcal{G})^2\times\partial^3_{mmm}\mathcal{G}}{(\partial^2_{mm}\mathcal{G})^2}) \\
&+2\frac{\partial^3_{\phi_1 mm}\mathcal{G}\times\partial^2_{\phi_1 m}\mathcal{G}\times\partial^2_{\phi_2 m}\mathcal{G}}{(\partial^2_{mm}\mathcal{G})^2} + \frac{\partial^3_{\phi_1 mm}\mathcal{G}\times(\partial^2_{\phi_2 m}\mathcal{G})^2}{(\partial^2_{mm}\mathcal{G})^2}
\end{aligned} \tag{E.1}$$

E.2 Partial derivatives of our model

We now give the the partial derivatives for our specific expression of $\mathcal{G}$ which is introduced in our work, *i.e.* eq. (2.33).

$$\begin{aligned}
\partial_{\phi_1}\mathcal{G}(\phi_1,\phi_2,m) &= -h_1(T)m + \ln(\phi_1) - \ln(1-\phi_1-\phi_2) + \ln(1-\delta(1-\phi_1-\phi_2)) \\
&- \ln(\phi_1+\phi_2) - \xi(m-1)[1-2\phi_1-2\phi_2] \\
&+\chi[1-2\phi_1-\phi_2] - \xi[1-2\phi_1-2\phi_2] \\
\partial_{\phi_2}\mathcal{G}(\phi_1,\phi_2,m) &= -h_2(T)m + \ln(\phi_2) - \ln(1-\phi_1-\phi_2) + \ln(1-\delta(1-\phi_1-\phi_2)) \\
&- \ln(\phi_1+\phi_2) - \xi(m-1)[1-2\phi_1-2\phi_2] \\
&-\chi\phi_1 - \xi[1-2\phi_1-2\phi_2] \\
\partial_m\mathcal{G}(\phi_1,\phi_2,m) &= -h_1(T)\phi_1 - h_2(T)\phi_2 - 4\tilde{J}m + \frac{1}{2}\ln(\frac{1+m}{1-m}) - \xi(1-\phi_1-\phi_2)(\phi_1+\phi_2) \\
\partial_{m,\phi_1}g(\phi_1,\phi_2,m) &= -h_1(T) + \xi(2\phi_1+2\phi_2-1) \\
\partial_{m,\phi_2}g(\phi_1,\phi_2,m) &= -h_2(T) + \xi(2\phi_1+2\phi_2-1) \\
\partial^2_{mm}\mathcal{G}(\phi_1,\phi_2,m) &= -4\tilde{J} + \frac{1}{1-m^2} \\
\partial^2_{\phi_1\phi_1}\mathcal{G}(\phi_1,\phi_2,m) &= \frac{1}{1-\phi_1-\phi_2} + \frac{\delta}{1-\delta(1-\phi_1-\phi_2)} + \frac{1}{\phi_1} - \frac{1}{\phi_1+\phi_2} + 2\xi(m-1) - 2(\chi-\xi) \\
\partial^2_{\phi_2\phi_2}\mathcal{G}(\phi_1,\phi_2,m) &= \frac{1}{1-\phi_1-\phi_2} + \frac{\delta}{1-\delta(1-\phi_1-\phi_2)} + \frac{1}{\phi_2} - \frac{1}{\phi_1+\phi_2} + 2\xi(m-1) + 2\xi \\
\partial^2_{\phi_1\phi_2}\mathcal{G}(\phi_1,\phi_2,m) &= \frac{1}{1-\phi_1-\phi_2} + \frac{\delta}{1-\delta(1-\phi_1-\phi_2)} - \frac{1}{\phi_1+\phi_2} + 2\xi(m-1) + 2\xi - \chi
\end{aligned}$$

$$\begin{aligned}
\partial^3_{\phi_1\phi_1\phi_1}\mathcal{G}(\phi_1,\phi_2,m) &= \frac{1}{(1-\phi_1-\phi_2)^2}+\frac{1}{(\phi_1+\phi_2)^2}-\frac{1}{\phi_1^2}-\frac{\delta^2}{[1-\delta(1-\phi_1-\phi_2)]^2}\\
\partial^3_{\phi_2\phi_2\phi_2}\mathcal{G}(\phi_1,\phi_2,m) &= \frac{1}{(1-\phi_1-\phi_2)^2}+\frac{1}{(\phi_1+\phi_2)^2}-\frac{1}{\phi_2^2}-\frac{\delta^2}{[1-\delta(1-\phi_1-\phi_2)]^2}\\
\partial^3_{\phi_1\phi_1\phi_2}\mathcal{G}(\phi_1,\phi_2,m) &= \frac{1}{(1-\phi_1-\phi_2)^2}+\frac{1}{(\phi_1+\phi_2)^2}-\frac{\delta^2}{[1-\delta(1-\phi_1-\phi_2)]^2}\\
\partial^3_{\phi_1\phi_2\phi_2}\mathcal{G}(\phi_1,\phi_2,m) &= \frac{1}{(1-\phi_1-\phi_2)^2}+\frac{1}{(\phi_1+\phi_2)^2}-\frac{\delta^2}{[1-\delta(1-\phi_1-\phi_2)]^2}\\
\partial^3_{\phi_1\phi_1 m}\mathcal{G}(\phi_1,\phi_2 m) &= 2\xi\\
\partial^3_{\phi_2\phi_2 m}\mathcal{G}(\phi_1,\phi_2,m) &= 2\xi\\
\partial^3_{\phi_1\phi_2 m}\mathcal{G}(\phi_1,\phi_2,m) &= 2\xi\\
\partial^3_{\phi_1 mm}\mathcal{G}(\phi_1,\phi_2,m) &= 0\\
\partial^3_{\phi_2 mm}\mathcal{G}(\phi_1,\phi_2,m) &= 0\\
\partial^3_{mmm}\mathcal{G}(\phi_1,\phi_2,m) &= \frac{2m}{(1-m^2)^2} \qquad \text{(E.2)}
\end{aligned}$$

The above expressions were checked with the help of Mathematica software, which was also used for solving numerically the non linear equations. The derivatives $\partial^3_{\phi_i mm}\mathcal{G}$ vanishes, which simplify a bit the expressions obtained for the third order derivatives $D^3\mathcal{G}$.

Finally, let us mention a relation between the determinant of the Hessian matrix and the original Hessian matrix:

$$\begin{vmatrix} \partial^2_{\phi_1\phi_1}\mathcal{G} & \partial^2_{\phi_1\phi_2}\mathcal{G} & \partial^2_{\phi_1 m}\mathcal{G}\\ \partial^2_{\phi_2\phi_1}\mathcal{G} & \partial^2_{\phi_2\phi_2}\mathcal{G} & \partial^2_{\phi_2 m}\mathcal{G}\\ \partial^2_{m\phi_1}\mathcal{G} & \partial^2_{m\phi_2}\mathcal{G} & \partial^2_{mm}\mathcal{G} \end{vmatrix} = \partial^2_{mm}\mathcal{G}\times\begin{vmatrix} D^2_{\phi_1\phi_1}\mathcal{G} & D^2_{\phi_1\phi_2}\mathcal{G}\\ D^2_{\phi_2\phi_1}\mathcal{G} & D^2_{\phi_2\phi_2}\mathcal{G}\end{vmatrix} \qquad \text{(E.3)}$$

The spinodal line can be found by setting any of the two above determinants to zero. However, it did not seem to us that the use of the 3 × 3 matrix would lead to simpler treatment than the 2 × 2 matrix that we considered in our approach.

Thermodynamic Approach to Phase Coexistence in Ternary Phospholipid-Cholesterol Mixtures

J. Wolff, C. M. Marques, and F. Thalmann*

Institut Charles Sadron, Université de Strasbourg, CNRS UPR 22, 23 rue du Loess, Strasbourg Cedex, F-67037, France

(Received 16 September 2010; published 23 March 2011)

We introduce a simple and predictive model for determining the phase stability of ternary phospholipid-cholesterol mixtures. Assuming that competition between the liquid and gel order of the phospholipids is the main driving force behind lipid segregation, we derive a Gibbs free energy of mixing, based on the thermodynamic properties of the lipids main transition. A numerical approach was devised that enables the fast and efficient determination of the ternary diagrams associated with our Gibbs free energy. The computed phase coexistence diagram of DOPC/DPPC/cholesterol reproduces well-known features for this system at 10 °C, as well as its evolution with temperature.

DOI: 10.1103/PhysRevLett.106.128104 PACS numbers: 87.16.dt, 64.75.−g, 87.14.Cc

Lipid membranes have captured the attention of physicists, chemists, and biologists alike owing to their prominent structural and functional roles in living cells, and to the pervading use of lipid based products in the pharmaceutical, food, and cosmetic industries [1,2]. In recent years, ternary lipid systems comprising phospholipids and cholesterol were established as important model systems in relation with lateral lipid segregation phenomena in membranes. At the root of this rich phenomenology lies a complex phase behavior of certain lipid mixtures, in which cholesterol molecules play a unique role. Ternary systems comprising a phospholipid in the liquid state, a second phospholipid in the gel state and cholesterol display several unique characteristics, the two most important of them being arguably a wide binary coexistence gap between the so-called liquid disordered (L_d) and liquid ordered (L_o) phases, and a region of triple coexistence [3–5].

A prominent feature of phospholipid membranes is their main thermodynamic transition, from a low temperature gel or rippled gel phase (usually termed L_β, P_β), to a high temperature liquid phase (L_α) [2]. A sharp change in the statistical conformations of the hydrophobic chains occurs at the transition, associated with membrane thinning and an increase of the area per phospholipid. The transition takes place at a melting temperature T_m whose precise value depends on the chemical structure of the chains. It is a weakly first order transition for a membrane of pure composition. The thermotropic behavior of phospholipid binary mixtures has been studied since the seminal work of Mabrey and Sturtevant [6] and supports the view that liquid-prone and gel-prone lipids tend to phase separate. This suggests that mixtures composed of phospholipids with the same head group have their miscibility behavior governed by the competition between their liquid and gel conformations. Hence, a description of ternary lipid systems must necessarily, and to some extent, account for the internal state of the phospholipids.

We introduce in this Letter a simple, robust, and predictive model of a phospholipid-cholesterol mixture's phase coexistence. Our model aims at predicting the miscibility behavior of phospholipids, based upon the thermodynamic properties of their main transition [7–10]. The thermotropic behavior of the phospholipid tails is modeled with an internal order parameter, in a way that schematically reproduces the thermodynamic features of the liquid-gel transition. The peculiar features of cholesterol-phospholipid interactions [11,12] are accounted for by means of a nonideal mixing entropy, generalizing the one proposed by Komura *et al.* [13]. In addition, we outline an original numerical procedure for the derivation of ternary phase diagrams.

The stability of a mixture is governed by its Gibbs free energy of mixing G_{mix}. This thermodynamic function expresses the free-energy difference between the homogeneous mixed state and the system comprising the separated pure components with the same global composition. Ternary mixtures in membranes are therefore described by $G_{\mathrm{mix}}(T, n_1, n_2, n_3)$, where the n_i are the molar contents of each lipid, and T the temperature. We assume that the hydrostatic pressure remains constant, close to the standard value, and that lipid membranes have no tension, so that these two intensive parameters are absent from G_{mix}. Membranes are assumed to be well hydrated with a large excess of water, and free from any other external fields [14].

The simplest realization of our model, described in this Letter, assumes that the areas per lipid a_i do not change with temperature. This allows us to express G_{mix} in terms of the surface fractions ϕ_1, ϕ_2, and ϕ_C of each lipid component, ϕ_C standing for the cholesterol. We claim that it is acceptable to neglect all changes in the area per lipid at $T = T_m$, in a first approximation to the description of the mixture phase coexistence, especially in the absence of membrane tension. This restriction is not a fundamental one, and versions of our model accounting for membrane expansion at the transition will be presented elsewhere [15].

A frequent approximation to nonideal solutions is obtained by combining an ideal mixing entropy with a quadratic enthalpic term. For a membrane of area $\mathcal{A}$, the free energy of mixing per unit of area, $g_{\text{mix}} = \beta G_{\text{mix}}/\mathcal{A}$, reads:

$$g_{\text{mix}} = \frac{\phi_1}{a_1}\ln(\phi_1) + \frac{\phi_2}{a_2}\ln(\phi_2) + \frac{\phi_C}{a_C}\ln(\phi_C) + \chi_{12}\phi_1\phi_2 + \chi_{1C}\phi_1\phi_C + \chi_{2C}\phi_2\phi_C, \quad (1)$$

with $\phi_1 + \phi_2 + \phi_C = 1$ and β the Boltzmann factor $1/k_BT$, and a_1, a_2, and a_C are the areas of the three different lipid species. One observes that expression (1) alone does not account for the main transition, and that the effective interaction parameters χ_{ij} are expected to display a nontrivial and unknown temperature dependence. We could not obtain, based on (1), any diagram comparable with the experimental ones. Moreover, our attempts to do so lead to unexpectedly large values of a_C, conflicting with the view that cholesterol molecules are smaller than phospholipids.

Both experiments and simulations suggest that cholesterol may form transient bound complexes with phospholipid moieties surrounding them [11,12]. The presence of such complexes prevents cholesterol molecules from occupying too many neighboring positions, thus giving the semblance of a large excluded volume. To account for the statistical behavior of cholesterol molecules, we derived the following entropic contribution, where all lipid areas have been set to unit:

$$\mathcal{G}^{(E)}(\phi_1, \phi_2) = \phi_1\ln(\phi_1) + \phi_2\ln(\phi_2) + \phi_C\ln(\phi_C) - (\phi_1 + \phi_2)\log(\phi_1 + \phi_2) + (\delta^{-1} - \phi_C)\log(1 - \delta\phi_C). \quad (2)$$

This expression originates from a lattice enumeration of configurations, following Flory, where each cholesterol molecule deprives an average number δ of neighboring sites from the possibility of being occupied by another cholesterol molecule. Expression (2) reduces to ideal mixing when $\delta \to 1$, and is similar to the entropy of Komura *et al.* for binary systems and $\delta = 2$ [13]. It accounts for both the mixing term and the excluded volume between cholesterol molecules, consistent with the presence of cholesterol complexes. It finally sets a maximal value $\phi_C \leq 1/\delta$ to the mixture content in cholesterol.

Several Landau order parameters have been proposed for describing the liquid-gel chain melting [7,8,10,13,16]. Theories based on a single scalar order parameter can pretend to capture only rough features of the main transition. This is why, for simplicity and generality, we restrict ourselves to a schematic approach, a two-state model based on a scalar order parameter m restricted to the interval $[-1, 1]$. The mean-field Ising model under finite external field serves as a guide [17].

$$\mathcal{G}^{(I)}(T, \phi_1, \phi_2, m) = -m\{h_1(T)\phi_1 + h_2(T)\phi_2\} - 2\tilde{J}m^2 + \left(\frac{1+m}{2}\right)\ln\left(\frac{1+m}{2}\right) + \left(\frac{1-m}{2}\right)\ln\left(\frac{1-m}{2}\right), \quad (3)$$

with

$$h_1(T) = \frac{\Delta H_1}{2RT_1^2}(T - T_1); \qquad h_2(T) = \frac{\Delta H_2}{2RT_2^2}(T - T_2), \quad (4)$$

and R is the gas constant. Equation (3) represents a mean-field Ising model in the presence of an effective external field $h_{\text{eff}} = h_1\phi_1 + h_2\phi_2$. For $\tilde{J} \geq \tilde{J}_c = 1/4$, the m dependence of $\mathcal{G}^{(I)}$ is shaped as a double well potential, with a linear bias induced by h_{eff}. The order parameter m fluctuates freely around an optimal value $m^\star$ located at the global minimum of $\mathcal{G}^{(I)}$, with (T, ϕ_1, ϕ_2) constant. In practice, as soon as $\tilde{J}$ is larger than 0.3, the two local minima are close to ± 1. We conventionally ascribe $m_g \simeq -1$ to represent the L_β gel phase, while $m_l \simeq 1$ is set to represent the L_α liquid phase. The coupling $\tilde{J}$ expresses that neighboring lipid tails tend to be in the same state, irrespective of the chemical species to which they belong. This is the main cooperative effect that induces the liquid-gel separation.

The term h_{eff} acts as a switch that drives the order parameter from its $m^\star = m_g$ gel state to its $m^\star = m_l$ liquid state, upon changing its sign from negative to positive. One sees from (4) that if lipid 1 is pure, $h_1(T)$ changes its sign at $T = T_1$ while $m^\star(T)$ suddenly jumps from m_g to m_l, with an amplitude $\Delta m^\star \simeq 2$. The enthalpic change is close to ΔH_1, so that ΔH_1 can be identified with the molar latent heat at the main transition. The difference in Gibbs free energy between the liquid and gel phases at $T \neq T_1$ is then extrapolated linearly with T at the vicinity of the transition. The contribution $\mathcal{G}^{(I)}$ is thus entirely specified by the temperature and the enthalpy difference at the transition of the lipid species composing the mixture. This term induces a liquid-gel separation in the whole temperature range $[T_1, T_2]$.

Cholesterol-phospholipid interactions are further accounted for with a specific interaction term

$$\mathcal{G}^{(C)}(\phi_1, \phi_2, m) = \chi\phi_1\phi_C - \xi m(\phi_1 + \phi_2)\phi_C. \quad (5)$$

Equation (5) comprises a m-dependent contribution, proportional to ξ, which marks the preference of cholesterol for either the $m = 1$ liquid order, or the $m = -1$ gel order, according to the sign of ξ. This interaction does not discriminate between saturated and unsaturated lipids, since it describes a coupling to the chain order. Other cholesterol-phospholipid interactions are accounted for by a m-independent contribution in χ. This order-insensitive interaction introduces a coupling between cholesterol and the unsaturated component. We found that interactions between cholesterol and the saturated component are not required to describe the experimental phase diagrams.

The sum $\mathcal{G}(T, \phi_1, \phi_2, m) = \mathcal{G}^{(E)} + \mathcal{G}^{(I)} + \mathcal{G}^{(C)}$ is our main thermodynamic potential. In the absence of surface tension, and assuming that changes in the internal state occur at constant volume, m fluctuates around its optimal value $m^\star$, with $m = m^\star$ in the thermodynamic limit. Therefore, the free energy of mixing $g_{\mathrm{mix}}(T, \phi_1, \phi_2)$ is obtained by minimizing $\mathcal{G}(T, \phi_1, \phi_2, m)$ with respect to m at fixed temperature and surface fractions [10].

$$\begin{aligned} g_{\mathrm{mix}}(T, \phi_1, \phi_2) &= \min_m[\mathcal{G}(T, \phi_1, \phi_2, m)]|_{T,\phi_1,\phi_2} \\ &= \mathcal{G}(T, \phi_1, \phi_2, m^\star(T, \phi_1, \phi_2)). \qquad (6) \end{aligned}$$

The Gibbs free-energy surface g_{mix} arises from projecting out m from the four-dimensional potential $\mathcal{G}$. Equivalently, g_{mix} can be viewed as the restriction of $\mathcal{G}$ to the submanifold $\partial_m \mathcal{G} = 0$. For $\tilde{J} > \tilde{J}_c$, the constraint $\partial_m \mathcal{G} = 0$ defines two stable submanifolds, a negative $m_g(T, \phi_1, \phi_2)$ and a positive $m_l(T, \phi_1, \phi_2)$ branch, linked, respectively, with the gel and liquid phases. At fixed (T, ϕ_1, ϕ_2) only one of the two branches is the stable one, while the other branch remains metastable.

In ternary mixtures it is known that phase coexistence is dictated by the convexity properties of $g_{\mathrm{mix}}(T, \phi_1, \phi_2)$ relative to ϕ_1, ϕ_2. Minimization of g_{mix} is equivalent to finding $\tilde{g}_{\mathrm{mix}}$, the lower convex hull of g_{mix}, that displays regions of three kinds. Points of the convex hull in contact with the original surface are stable monophasic regions. Regions lying above triple tangent planes correspond to triple coexistence. The remaining part of the convex hull corresponds to developable patches of surface, wrapped around double tangent lines that connect pairs of points with distinct composition (tie-lines) [18]. In practice, we used a public domain routine, *qhull*, to compute a discrete approximation of $\tilde{g}_{\mathrm{mix}}$ [19]. The starting point is a fine mesh discretization of g_{mix} over the relevant domain of composition $\{\phi_1, \phi_2 \geq 0, \phi_1 + \phi_2 \leq 1 - 1/\delta\}$. Then *qhull* computes a triangulated surface approaching $\tilde{g}_{\mathrm{mix}}$. Triple coexistence corresponds to facets with all sides much larger than the initial mesh size. Double coexistence is associated with elongated triangles, with a shortest side much smaller than the two longer sides, the latter being oriented parallel with the tie lines. Finally, small facets of the convex minimization are linked with stable monophasic regions. The projection of the triangulated $\tilde{g}_{\mathrm{mix}}$ surface onto the composition plane provides directly a fast and accurate approximation of the Gibbs phase diagram shown in Fig. 1(a). This discrete solution can then be refined according to the usual rules for the determination of ternary phase diagrams. Details of these calculations will be given in a forthcoming publication [15].

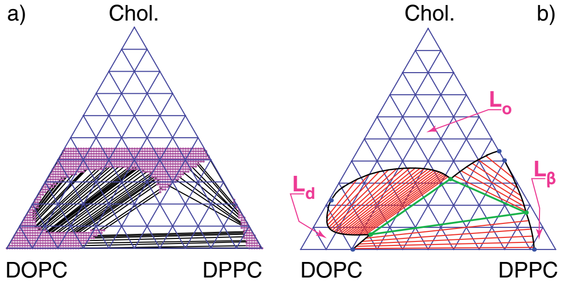

FIG. 1 (color online). (a) Discrete approximation to the ternary phase diagram obtained from the lower convex hull method explained in the text. (b) Final phase diagram determined from the analytical refinement of the discrete approximation.

Arguably, the most widely studied ternary lipid phase diagram for membranes containing cholesterol is the ternary mixture DOPC/DPPC/Chol. DOPC is a double tail molecule with 18 carbons per tail and a *cis*-unsaturated bond on the ninth carbon. It has a low main transition temperature T_1 at $-21\,^\circ\mathrm{C}$ and an associated enthalpy change ΔH_1 evaluated at 7.7 kcal/mol [20]. DPPC also has a phosphatidylcholine head but here the two 16-carbon tails have no unsaturated bonds, leading to a higher transition temperature T_2 at $42\,^\circ\mathrm{C}$, and associated enthalpy change $\Delta H_2 = 8.7$ kcal/mol [20]. Within our approach, the above temperature and enthalpy values and a single coupling parameter $\tilde{J} = 0.35$—see Eq. (3)—describe well published data [21] for the experimental binary DOPC/DPPC mixing behavior. For a complete description of the ternary phase diagram our model further requires three parameters: δ, ξ, and χ. The value of δ is bound by the maximum amount of cholesterol that a membrane can hold, estimated here at $\phi_C \simeq 0.45$ or equivalently $\delta = 1/\phi_C = 2.2$ [3]. The parameter ξ, as defined in Eq. (5), quantifies the preference of cholesterol for the liquid disordered phase with respect to the gel phase [1,22]. Binary diagrams of DPPC/Chol computed with $\xi = 1.8$ reproduce well the temperature behavior of the miscibility gaps occurring between the L_β-gel phase and the L_o liquid ordered phase as determined from giant unilamellar vesicles in [23] and from NMR [24]—see Fig. 2. Equation (5) also includes a repulsive m-independent interaction between cholesterol and the unsaturated component, given by χ. At $10\,^\circ\mathrm{C}$ a value of $\chi = 6.0$ promotes both a triple coexistence region and a large biphasic domain, with oblique L_o/L_d tie lines of positive slope and a plait point on the left side of the Gibbs triangle, in agreement with experimental findings [5]. A larger value of χ there would open a miscibility gap, unseen for DOPC/Chol, while a smaller value would drastically reduce the biphasic L_o/L_d domain. In our model a continuous path connects the L_o and L_d regions around the critical point, where the order parameter m remains positive. The L_β phase on the lower right corner of the phase diagram is associated with a negative m value

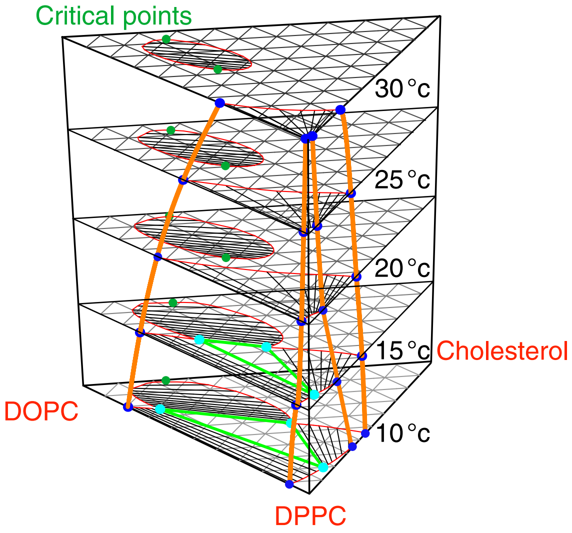

FIG. 2 (color online). Computed evolution of the DPPC/DOPC/Chol triangular diagram with temperature. The computed diagrams display the main expected features for this lipid mixture.

and separated from the rest of the diagram by a discontinuity in m across the coexistence gap.

The evolution of the Gibbs diagram with respect to temperature is displayed in Fig. 2. The diagram was drawn here under the assumption of a constant ξ parameter, and a constant value of the coupling contribution $k_B T \chi$ denoting its pure enthalpic nature. Our diagram at the lower temperature in Fig. 2, displays the main expected features for a DOPC/DPPC/Chol mixture. As the temperature increases, the triple coexistence triangle shrinks and vanishes between 15 °C and 20 °C. Also, the L_o/L_d biphasic region, resting initially on the left side of the triangle, detaches and assumes a closed shape of decreasing surface. A first critical point, on the left side of the Gibbs diagram, evolves slowly away from the edge [4]. A second critical point, initially hidden by the triple coexistence region, is predicted to emerge at the binary detachment temperature. Note also that within our approach the extension of the L_β domain, on the right bottom part of the diagram, gradually decreases up to T_2.

As a summary we presented a model for phase coexistence in ternary phospholipid-cholesterol mixtures. Our approach is based on a mean-field two-state description of the phospholipids and a nonideal mixing entropy for cholesterol. All parameters but one in our system are bound by known thermodynamic or physical properties. We combined analytical theory and numerical convex minimization to show the predictive power of our model for the ternary mixture DOPC/DPPC/Chol. Resulting phase coexistence diagrams reproduce well known features for this system at 10 °C as well as the temperature variation of the diagram. We are also encouraged by preliminary results from related ternary systems that further indicate that our model successfully describes a large variety of lipid/lipid/cholesterol mixtures.

*fabrice.thalmann@ics-cnrs.unistra.fr

[1] O. Mouritsen, *Life-as a Matter of Fat: The Emerging Science of Lipidomics* (Springer, New York, 2005).
[2] T. Heimburg, *Thermal Biophysics of Membranes* (Wiley-VCH, Weinheim, NY, 2007).
[3] J. Zhao, J. Wu, F. Heberle, T. Mills, P. Klawitter, G. Huang, G. Costanza, and G. Feigenson, Biochim. Biophys. Acta **1768**, 2764 (2007).
[4] S. Veatch, O. Soubias, S. Keller, and K. Gawrisch, Proc. Natl. Acad. Sci. U.S.A. **104**, 17 650 (2007).
[5] F. Goñi, A. Alonso, L. Bagatolli, R. Brown, D. Marsh, M. Prieto, and J. Thewalt, Biochim. Biophys. Acta **1781**, 665 (2008).
[6] S. Mabrey and J. Sturtevant, Proc. Natl. Acad. Sci. U.S.A. **73**, 3862 (1976).
[7] R. Priest, Mol. Cryst. Liq. Cryst. **60**, 167 (1980).
[8] I. Sugar and G. Monticelli, Biophys. Chem. **18**, 281 (1983).
[9] S. Komura, H. Shirotori, and P. Olmsted, J. Phys. Condens. Matter **17**, S2951 (2005).
[10] G. Putzel and M. Schick, Biophys. J. **95**, 4756 (2008).
[11] A. Radhakrishnan and H. McConnell, Biophys. J. **77**, 1507 (1999).
[12] A. Radhakrishnan and H. McConnell, Proc. Natl. Acad. Sci. U.S.A. **102**, 12 662 (2005).
[13] S. Komura, H. Shirotori, P. Olmsted, and D. Andelman, Europhys. Lett. **67**, 321 (2004).
[14] B. Różycki, T. R. Weikl, and R. Lipowsky, Phys. Rev. Lett. **100**, 098103 (2008).
[15] J. Wolff, C. Marques, and F. Thalmann (to be published).
[16] R. Goldstein and S. Leibler, Phys. Rev. A **40**, 1025 (1989).
[17] P. Chaikin and T. Lubensky, *Principle of Condensed Matter Physics* (Cambridge University Press, Cambridge, England, 1995).
[18] J. Gibbs, *The Scientific Papers of J. Willard Gibbs, Volume 1, Thermodynamics* (Ox Bow Press, Woodbridge, CT, 1993).
[19] C. Barber, D. Dobkin, and H. Huhdanpaa, ACM Trans. Math. Softw. **22**, 469 (1996); http://www.qhull.org.
[20] G. Cevc, *Phospholipids Handbook* (CRC Press, New York, NY, 1993).
[21] M. Schmidt, L. Ziani, M. Boudreau, and J. Davis, J. Chem. Phys. **131**, 175103 (2009).
[22] H. Ipsen, G. Karlström, O. Mouritsen, H. Wennerström, and M. Zuckermann, Biochim. Biophys. Acta **905**, 162 (1987).
[23] S. Veatch and S. Keller, Biophys. J. **85**, 3074 (2003).
[24] M. R. Vist and J. H. Davis, Biochemistry **29**, 451 (1990).

Bibliography

[1] https://campusvirtuel.smbh.univ-paris13.fr.

[2] E. Gorter and F. Grendel. On bimolecular layers of lipoids on the chromocytes of the blood. *The Journal of Experimental Medicine*, 41(4):439–443, 1925.

[3] S. J. Singer and G.L. Nicolson. The fluid mosaic model of the structure of cell membranes. *Science*, 175(4023):720–731, 1972.

[4] H.I. Petrache, S.W. Dodd, and Brown M.F. Area per lipid and acyl length distributions in fluid phosphatidylcholines determined by 2h nmr spectroscopy. *Biophysical journal*, 79:31723192, 2000.

[5] G. Cevc. *Phospholipids Handbook*. CRC Press, 1993.

[6] O.G Mouritsen. *Life-As A Matter of Fat*. Springer, 2005.

[7] J.N.Israelachvili. *Intermolecular Surface Forces*. Academic Press INC., 1985.

[8] C. Loudet, A. Diller, A. Grelard, R. Oda, and E.J. Dufourc. Biphenyl phosphatidylcholine: A promoter of liposome deformation and bicelle collective orientation by magnetic fields. *Progress in Lipid Research*, 49:289 – 297, 2010.

[9] J.M Seddon and R.H Templer. *Polymorphism of Lipid-Water Systems*. Elsevier Science B.V., 1995.

[10] R. Dimova, S. Aranda, N. Bezlyepkina, V. Nikolov, K.A. Riske, and R. Lipowsky. A practical guide to giant vesicles. probing the membrane nanoregime via optical microscopy. *Journal of Physics: Condensed Matter*, 18(28):S1151, 2006.

[11] J.J. Myher, A. Kuksis, and S. Pind. Molecular species of glycerophospholipids and sphingomyelins of human erythrocytes: Improved method of analysis. *Lipids*, 24:396–407, 1989.

[12] G.Cevc and D.Marsh. *Phospholipid bilayers.* A Wiley-Interscience Publication, 1987.

[13] H. Heller, M. Schaefer, and K. Schulten. Molecular dynamics simulation of a bilayer of 200 lipids in the gel and in the liquid crystal phase. *The Journal of Physical Chemistry*, 97(31):8343–8360, 1993.

[14] M. Mihailescu, R.G. Vaswani, E. Jardon-Valadez, F. Castro-Roman, J.A. Freites, D.L. Worcester, A.R. Chamberlin, D.J. Tobias, and S.H. White. Acyl-chain methyl distributions of liquid-ordered and -disordered membranes. *Biophysical J*, 100:1455–1462, 2011.

[15] R.S. Gracia, N. Bezlyepkina, R.L. Knorr, R. Lipowsky, and R. Dimova. Effect of cholesterol on the rigidity of saturated and unsaturated membranes: fluctuation and electrodeformation analysis of giant vesicles. *Soft Matter*, 6:1472–1482, 2010.

[16] E. Van den Brink-van der Laan, J.A. Killian, and B. de Kruijff. Nonbilayer lipids affect peripheral and integral membrane proteins via changes in the lateral pressure profile. *Biochimica et Biophysica Acta (BBA) - Biomembranes*, 1666:275 – 288, 2004.

[17] K. Youngchan, K. Kyoohyun, and Y. Park. *Measurement Techniques for Red Blood Cell Deformability: Recent Advances (chapter 10).* InTech, 2012.

[18] S. Leibler and D. Andelman. Ordered and curved meso-structures in membranes and amphiphilic films. *Journal de physique*, 48:2013–2018, 1987.

[19] T. Heimburg. *Thermal Biophysics of Membranes.* Wiley-VCH, 2007.

[20] J.H. Ipsen and O.G. Mouritsen. Modelling the phase equilibria in two-component membranes of phospholipids with different acyl-chain lengths. *Biochimica et Biophysica Acta (BBA) - Biomembranes*, 944(2):121 – 134, 1988.

[21] M.O. Jensen and O.G. Mouritsen. Lipids do influence protein function—the hydrophobic matching hypothesis revisited. *Biochimica et Biophysica Acta (BBA) - Biomembranes*, 1666:205 – 226, 2004.

[22] K. Simons and E. Ikonen. Functional rafts in cell membranes. *Nature*, 387:569, 1997.

[23] F.M. Goñi, A. Alonso, L.A. Bagatolli, R. E. Brown, D. Marsh, M. Prieto, and J.L. Thewalt. Phase diagrams of lipid mixtures relevant to the study of membrane rafts. *Biochim. Biophys. Acta*, 1781:665–684, 2008.

[24] M.L. Schmidt, L. Ziani, M. Boudreau, and J.H. Davis. Phase equilibria in dopc/dppc: Conversion from gel to subgel in two component mixtures. *J.Chem.Phys.*, 131(17):175103, 2009.

[25] A. Radhakrishnan and H. McConnell. Condensed complexes of cholesterol and phospholipids. *Biophysical Journal*, 77:1507–1517, 1999.

[26] A. Radhakrishnan and H. McConnell. Condensed complexes in vesicles containing cholesterol and phospholipids. *PNAS*, 102(36):12662–12666, 2005.

[27] D. Marsh. Liquid-ordered phases induced by cholesterol: A compendium of binary phase diagrams. *Biochimica et Biophysica Acta (BBA) - Biomembranes*, 1798(3):688 – 699, 2010.

[28] J. Zhao, J. Wu, F.A. Heberle, T.T. Mills, P. Klawitter, G. Huang, G. Costanza, and G.W. Feigenson. Phase studies of model biomembranes: Complex behavior of dspc/dopc/cholesterol. *B.B.A.*, 1768:2764, 2007.

[29] M. Venturoli, M.M. Sperotto, M. Kranenburg, and B. Smit. Mesoscopic models of biological membranes. *Physics Reports*, 437(1–2):1 – 54, 2006.

[30] T. Heimburg. A model for the lipid pretransition: Coupling of ripple formation with the chain-melting transition. *Biophysical Journal*, 78(3):1154 – 1165, 2000.

[31] H.J. Risselada and S.J. Marrink. The molecular face of lipid rafts in model membranes. *Proceedings of the National Academy of Sciences*, 105(45):17367–17372, 2008.

[32] J.F. Nagle and S. Tristram-Nagle. Structure of lipid bilayers. *Biochimica et Biophysica Acta (BBA) - Reviews on Biomembranes*, 1469(3):159 – 195, 2000.

[33] W.C. Hung, F.Y. Chen, and Huey W. Huang. Order-disorder transition in bilayers of diphytanoyl phosphatidylcholine. *Biochimica et Biophysica Acta (BBA) - Biomembranes*, 1467(1):198 – 206, 2000.

[34] J. Daillant, E. Bellet-Amalric, A. Braslau, T. Charitat, G. Fragneto, F. Graner, S. Mora, F. Rieutord, and B. Stidder. Structure and fluctuations of a single floating lipid bilayer. *Proceedings of the National Academy of Sciences of the United States of America*, 102(33):11639–11644, 2005.

[35] A. Hemmerle, L. Malaquin, T. Charitat, S. Lecuyer, G. Fragneto, and J. Daillant. Controlling interactions in supported bilayers from weak electrostatic repulsion to high osmotic pressure. *Proceedings of the National Academy of Sciences*, 109(49):19938–19942, 2012.

[36] L.S. Vermeer, B. Groot, V. Reat, A. Milon, and J. Czaplicki. Acyl chain order parameter profiles in phospholipid bilayers: computation from molecular dynamics simulations and comparison with 2h nmr experiments. *European Biophysics Journal*, 36:919–931, 2007.

[37] S.L. Veatch, I.V. Polozov, K. Gawrisch, and S.L. Keller. Liquid domains in vesicles investigated by nmr and fluorescence microscopy. *Biophysical journal*, 86:2910–2922, 2004.

[38] Y. Yu and S. Granick. Pearling of lipid vesicles induced by nanoparticles. *Journal of the American Chemical Society*, 131(40):14158–14159, 2009.

[39] J. R. Silvius. Fluorescence energy transfer reveals microdomain formation at physiological temperatures in lipid mixtures modeling the outer leaflet of the plasma membrane. *Biophysical journal*, 85:10341045, 2003.

[40] L. A. Bagatolli and E. Gratton. Two-photon fluorescence microscopy observation of shape changes at the phase transition in phospholipid giant unilamellar vesicles. *Biophysical Journal*, 77:20902101, 1999.

[41] C.K. Haluska, A.P. Schroeder, P. Didier, D. Heissler, G. Duportail, Y. Mely, and C.M. Marques. Combining fluorescence lifetime and polarization microscopy to discriminate phase separated domains in giant unilamellar vesicles. *Biophysical Journal*, 95:5737–5747, 2008.

[42] H.G Wolfgang, B. Bechinger, and T. Lele. Chapter eight cytoskeletal proteins at the lipid membrane. volume 6 of *Advances in Planar Lipid Bilayers and Liposomes*, pages 227 – 264. Academic Press, 2008.

[43] S. G. Whittington and D. Chapman. Effect of density on configurational properties of long-chain molecules using a monte carlo method. *Trans. Faraday Soc.*, 62:3319–3324, 1966.

[44] D. Chapman, R.M. Williams, and B.D. Ladbrooke. Physical studies of phospholipids. vi. thermotropic and lyotropic mesomorphism of some 1,2-diacyl-phosphatidylcholines (lecithins). *Chemistry and Physics of Lipids*, 1(5):445 – 475, 1967.

[45] J. F. Nagle. Theory of biomembrane phase transitions. *The Journal of Chemical Physics*, 58(1):252–264, 1973.

[46] S. Marcelja. Chain ordering in liquid crystals: Ii. structure of bilayer membranes. *Biochimica et Biophysica Acta (BBA) - Biomembranes*, 367(2):165 – 176, 1974.

[47] D. Marsh. Statistical mechanics of the fluidity of phospholipid bilayers and membranes. *The Journal of Membrane Biology*, 18:145–162, 1974.

[48] Jr. H. L. Scott. Some models for lipid bilayer and biomembrane phase transitions. *The Journal of Chemical Physics*, 62(4):1347–1353, 1975.

[49] R.E. Jacobs, B. Hudson, and H.C. Andersen. A theory of the chain melting phase transition of aqueous phospholipid dispersions. *Proceedings of the National Academy of Sciences*, 72(10):3993–3997, 1975.

[50] S. Doniach. Thermodynamic fluctuations in phospholipid bilayers. *The Journal of Chemical Physics*, 68(11):4912–4916, 1978.

[51] A. Caille, A. Rapini, M. J. Zuckermann, A. Cros, and S. Doniach. A simple model for phase transitions in monolayers and bilayers of lipid molecules. *Canadian Journal of Physics*, 56(3):348–357, 1978.

[52] R.E. Goldstein and S. Leibler. Structural phase transitions of interacting membranes. *Phys. Rev. A*, 40(2):1025–1035, Jul 1989.

[53] A.G. Lee. Lipid phase transitions and phase diagrams ii. mixtures involving lipids. *Biochimica et Biophysica Acta (BBA) - Reviews on Biomembranes*, 472(34):285 – 344, 1977.

[54] A.G. Lee. Calculation of phase diagrams for non-ideal mixtures of lipids, and a possible non-random distribution of lipids in lipid mixtures in the liquid crystalline phase. *Biochimica et Biophysica Acta (BBA) - Biomembranes*, 507(3):433 – 444, 1978.

[55] S.A. Simon, W.L. Stone, and P.B. Benett. Can regular solution trheory be applied to lipid bilayer menbranes? *BBA-biomembranes*, 550:38–47, 1979.

[56] R.G. Priest. Landau phenomenological theory of one and two component phospholipid bilayers. *Molecular Crystals and Liquid Crystals*, 60:167–180, 1980.

[57] L.D. Landau and E.M.Lifshitz. *Statistical physics.* 1969.

[58] I.P. Sugar and G. Monticelli. Landau theory of two-component phospholipid bilayers: I. phosphatidylcholine/phosphatidylethanolamine mixtures. *Biophysical Chemistry*, 18(4):281– – 289, 1983.

[59] M.R. Vist. *Partial Phase Behaviour of Perpeuterated Dipalmitoyl Phosphatidylcholine-cholesterol Model Membranes.* PhD thesis, University of Guelph, Ontario, Canada, 1984.

[60] M.R. Vist and J.H. Davis. Phase equilibria of cholesterol/dipalmitoylphosphatidylcholine mixtures: deuterium nuclear magnetic resonance and differential scanning calorimetry. *Biochemistry*, 29(2):451–464, 1990.

[61] J.H Ipsen, G. Karlström, O.G. Mouritsen, H. Wennerström, and M.J. Zuckermann. Phase equilibria in phosphatidylcholine-cholesterol system. *Biochim. Biophys. Acta*, 905:162–172, 1987.

[62] T.P.W. McMullen and R.N. McElhaney. New aspects of the interaction of cholesterol with dipalmitoylphosphatidylcholine bilayers as revealed by high-sensitivity differential scanning calorimetry. *Biochimica et Biophysica Acta (BBA) - Biomembranes*, 1234(1):90 – 98, 1995.

[63] M. Nielsen, L. Miao, J.H. Ipsen, M.J. Zuckermann, and O.G. Mouritsen. Off-lattice model for the phase behavior of lipid-cholesterol bilayers. *Phys. Rev. E*, 59:5790–5803, May 1999.

[64] I.P. Sugar, T.E. Thompson, and R.L. Biltonen. Monte carlo simulation of two-component bilayers: Dmpc/dspc mixtures. *Biophysical journal*, 76:2099, 1999.

[65] M.B. Sankaram and T.E. Thompson. Cholesterol-induced fluid-phase immiscibility in membranes. *Proceedings of the National Academy of Sciences*, 88(19):8686–8690, 1991.

[66] S. Komura, H. Shirotori, P. D. Olmsted, and D. Andelman. Lateral phase separation in mixtures of lipids and cholesterol. *EPL (Europhysics Letters)*, 67(2):321, 2004.

[67] J. Huang. Exploration of molecular interactions in cholesterol superlattices: Effect of multibody interactions. *Biophysical j*, 83:1014–1025, 2002.

[68] S.L. Veatch, O. Soubias, S.L. Keller, and K. Gawrisch. critical fluctuations in domain-forming lipid mixtures. *PNAS*, 104:17650–17655, 2007.

[69] R.F.M. de Almeida, A. Fedorov, and M. Prieto. Sphingomyelin/phosphatidylcholine/cholesterol phase diagram: Boundaries and composition of lipid rafts. *Biophysical jou*, 85:2406–2416, 2003.

[70] S. Komura, H. Shirotori, and P. D. Olmsted. Phase behaviour of three-component lipid mixtures. *Journal of Physics: Condensed Matter*, 17(31):S2951, 2005.

[71] G.G. Putzel and M. Schick. Phenomenological model and phase behavior of saturated and unsaturated lipids and cholesterol. *Biophysical Journal*, 95(10):4756 – 4762, 2008.

[72] J. de Joannis, P.S. Coppock, F. Yin, M. Mori, A. Zamorano, and J.T. Kindt. Atomistic simulation of cholesterol effects on miscibility of saturated and unsaturated phospholipids: Implications for liquid-ordered/liquid-disordered phase coexistence. *Journal of the American Chemical Society*, 133(10):3625–3634, 2011.

[73] T. Gil, M.C. Sabra, J.H. Ipsen, and O.G. Mouritsen. Wetting and capillary condensation as means of protein organization in membranes. *Biophysical Journal*, 73:1728 – 1741, 1997.

[74] T. Gil, J.H Ipsen, O.G. Mouritsen, C.S. Mads, M.M. Sperotto, and M.J. Zuckermann. Theoretical analysis of protein organization in lipid membranes. *Biochimica et Biophysica Acta (BBA) - Reviews on Biomembranes*, 1376(3):245 – 266, 1998.

[75] T.Baumgart, S.T.Hess, and W.W.Webb. Imaging coexisting fluid domains in biomembrane models coupling curvature and line tension. *Nature*, 425:821–824, 2003.

[76] J.W Cahn. Critical point wetting. *journal of chemical physics*, 66:3667, 1977.

[77] D. Bonn and D. Ross. Wetting transitions. *Reports on Progress in Physics*, 64(9):1085, 2001.

[78] P. J. Flory. *Statistical Mechanics of Chain Molecules.* 1969.

[79] J. Lajzerowicz and J. Sivardiere. Spin-1 lattice-gas model. i. condensation and solidification of a simple fluid. *Phys. Rev. A*, 11:2079–2089, Jun 1975.

[80] M.R. Morrow and J.H. Davis. Differential scanning calorimetry and deuterium nmr studies of the phase behavior of gramicidin-phosphatidylcholine mixtures. *Biochemistry*, 27(6):2024–2032, 1988.

[81] W. Schrader, H. Ebel, P. Grabitz, E. Hanke, T. Heimburg, M. Hoeckel, M. Kahle, F. Wente, and U. Kaatze. Compressibility of lipid mixtures studied by calorimetry and ultrasonic velocity measurements. *The Journal of Physical Chemistry B*, 106(25):6581–6586, 2002.

[82] V.P. Ivanova and T. Heimburg. Histogram method to obtain heat capacities in lipid monolayers, curved bilayers, and membranes containing peptides. *Phys. Rev. E*, 63:041914, Mar 2001.

[83] S.L.Veatch and S.L.Keller. Separation of liquid phases in giant vesicles of ternary mixtures of phospholipids and cholesterol. *Biophysical Journal*, 85:3074–3083, 2003.

[84] J.W.Gibbs. *The Scientific Papers of J. Willard Gibbs, volume 1, Thermodynamics.* Oxbow Press, 1993.

[85] C.B.Barber, D.P.Dobkin, and H.Huhdanpaa. Acm trans on mathematical software, http://www.qhull.org. 1996.

[86] S.L. Veatch and S.L. Keller. Miscibility phase diagrams of giant vesicles containing sphingomyelin. *Phys. Rev. Lett.*, 94:148101, Apr 2005.

[87] N. Bezlyepkina, R.S. Gracia, P. Shchelokovskyy, R. Lipowsky, and R. Dimova. Phase diagram and tie-line determination for the ternary mixture dopc/esm/cholesterol. *Biophysical Journal*, 104:14561464, 2013.

[88] R. Brewster and S.A. Safran. Line active hybrid lipids determine domain size in phase separation of saturated and unsaturated lipids. *Biophysical Journal*, 98:L21L23, 2010.

[89] H. Lindsey, N.O. Petersen, and S.I. Chan. Physicochemical characterization of 1,2-diphytanoyl-sn-glycero-3-phosphocholine in model membrane systems. *Biochimica et Biophysica Acta (BBA) - Biomembranes*, 555(1):147 – 167, 1979.

[90] S.L. Veatch, K. Gawrisch, and S.L. Keller. Closed-loop miscibility gap and quantitative tie-lines in ternary membranes containing diphytanoyl pc. *Biophysical journal*, 80:4428–4436, 2006.

[91] A. Tian, C. Johnson, W. Wang, and T. Baumgart. Line tension at fluid membrane domain boundaries measured by micropipette aspiration. *Phys. Rev. Lett.*, 98:208102, May 2007.

[92] T. Baumgart, S.T. Hess, and W.W. Webb. Imaging coexisting fluid domains in biomembrane models coupling curvature and line tension. *Nature*, 425(6960):821–824, October 2003.

[93] T. Baumgart, S. Das, W.W. Webb, and J.T. Jenkins. Membrane elasticity in giant vesicles with fluid phase coexistence. *Biophysical Journal*, 89:1067–1080, 2005.

[94] W.H Press. *Numerical recipes in C.* Cambridge University Press, 1992.

[95] S.A. Akimov, V.A.J. Frolov, P.I. Kuzmin, J. Zimmerberg, Y.A. Chizmadzhev, and F.S. Cohen. Domain formation in membranes caused by lipid wetting of protein. *Phys. Rev. E*, 77:051901, May 2008.

[96] R. Phillips, T. Ursell, P. Wiggins, and P. Sens. Emerging roles for lipids in shaping membrane-protein function. *Nature*, 459(7245):379–385, May 2009.

[97] T. Gil and L.V. Mikheev. Curvature controlled wetting in two dimensions. *Phys. Rev. E*, 52:772–780, Jul 1995.

[98] G. Tamir and J.H. Ipsen. Capillary condensation between disks in two dimensions. *Phys. Rev. E*, 55:1713–1721, Feb 1997.

Abstract We propose a new theoretical model for describing the formation and the phase coexistence in ternary mixtures of phospholipids and cholesterol. This model combines the properties of the liquid-gel phase transition, described with an internal order parameter, with some non ideal mixing behavior accounting for the influence of cholesterol, and inspired by Flory's description of polymer melts. Our thermodynamical approach successfully accounts for the coexistence of binary phospholipid mixtures such as DOPC-DPPC. The order parameter, originally introduced by Doniach, describes in a simplified manner the thermodynamics of the alkyl chains in a lipid bilayer, by analogy with the Ising model under magnetic field. We not only obtain ternary diagrams resembling to experimental diagrams, but also discuss the evolution of these phase equilibria with temperature. This approach is then generalized to other lipid components, namely PSM, POPC and DiphytanoylPC. Our approach, made of a combination of discrete geometry calculations and numerical resolutions of the analytical equations for determining the properties of the Gibbs diagram is novel, and applies to a wide class of thermodynamic models with order parameters. A Landau-Ginzburg extension of the above model allows us to study inhomogeneous systems. A first important application consists in determining the line tension τ and the profile of an interface separating macrodomains of ordered and disordered liquid phase. We extend Cahn's wetting theory to the case of a circular inclusion of finite radius R in a "lipid sea", at coexistence and off-coexistence. We finally discuss the effects of the proximity of a critical point, and the consequences relative to mutual interactions between impurities induced by the wetting process.

Resume Nous proposons un modèle théorique original pour décrire le processus de formation et la coexistence de phase dans les mélanges ternaires de phospholipides et de cholestérol. Ce modèle combine les effets de transitions de phase liquide-gel, décrits à l'aide d'un paramètre d'ordre interne, et les effets de mélange non-idéaux inspirés des modèles de Flory pour décrire l'influence du cholestérol. Notre approche thermodynamique décrit avec un réel succès la coexistence de mélanges phospholipide binaires, tel que DOPC-DPPC. Le paramètre d'ordre inspiré de l'approche de Doniach et de l'analogie avec le modèle d'Ising sous champ magnétique modélise de façon simplifiée la thermodynamique des chaînes alkyles dans la bicouche lipidique. Nous obtenons d'une part des diagrammes ternaires ressemblant aux diagrammes expérimentaux mais aussi la dépendance en température des équilibres de phases. Nous décrivons également des diagrammes pour d'autres espèces, telles que PSM, POPC ou DiphytanoylPC. Notre approche, combinant géométrie discrète et résolution des équations analytiques pour la détermination des caractéristiques des diagrammes de Gibbs est novatrice, et s'applique à une classe étendue de modèles thermodynamiques avec paramètre d'ordre. Nous cherchons ensuite à décrire des systèmes inhomogènes à l'aide d'une généralisation de Ginzburg-Landau du modèle précédent. Une application importante consiste à déterminer la tension de ligne τ et le profil d'une interface entre macrodomaines de phase liquide ordonné et désordonné. Enfin, nous étendons la théorie du mouillage de Cahn à la description de l'environnement d'une inclusion circulaire de rayon fini R dans un "océan lipidique", à coexistence et hors coexistence. Nous discutons pour finir les effets de la proximité du point critique et ses conséquences quant aux interactions entre impuretés induites par les effets de mouillage.